PL-TR-93-2072

MODELING REGIONAL SEISMIC WAVES

Donald V. Helmberger
David G. Harkrider

California Institute of Technology
Seismological Laboratory
Division of Geological and Planetary Sciences
Pasadena, CA 91125

24 March 1993

Final Report
26 September 1991- 25 September 1992

APPROVED FOR PUBLIC RELEASE; DISTRIBUTION UNLIMITED

PHILLIPS LABORATORY
Directorate of Geophysics
AIR FORCE MATERIEL COMMAND
HANSCOM AIR FORCE BASE, MA 01731-3010

The views and conclusions contained in this document are those of the authors and should not be interpreted as representing the official policies, either expressed or implied, of the Air Force or the U.S. Government.

This technical report has been reviewed and is approved for publication.

JAMES F. LEWKOWICZ
Contract Manager
Solid Earth Geophysics Branch
Earth Sciences Division

JAMES F. LEWKOWICZ
Branch Chief
Solid Earth Geophysics Branch
Earth Sciences Division

DONALD H. ECKHARDT, Director
Earth Sciences Division

This document has been reviewed by the ESD Public Affairs Office (PA) and is releasable to the National Technical Information Service (NTIS).

Qualified requestors may obtain additional copies from the Defense Technical Information Center. All others should apply to the National Technical Information Service.

If your address has changed, or if you wish to be removed from the mailing list, or if the addressee is no longer employed by your organization, please notify PL/TSI, Hanscom AFB MA 01731-3010. This will assist us in maintaining a current mailing list.

Do not return copies of this report unless contractual obligations or notices on a specific document requires that it be returned.

REPORT DOCUMENTATION PAGE

Form Approved
OMB No. 0704-0188

1. AGENCY USE ONLY (Leave blank)	2. REPORT DATE	3. REPORT TYPE AND DATES COVERED
	24 March 1993	Final Report (9/26/91 - 9/25/92)

4. TITLE AND SUBTITLE

Modeling Regional Seismic Waves

5. FUNDING NUMBERS

PE 62101F
PR 7600 TA 09 WU BA
Contract F19628-90-K-0049

6. AUTHOR(S)

Donald V. Helmberger
David G. Harkrider

7. PERFORMING ORGANIZATION NAME(S) AND ADDRESS(ES)

California Institute of Technology
Seismological Laboratory
Division of Geological and Planetary Sciences
Pasadena, CA 91125

8. PERFORMING ORGANIZATION REPORT NUMBER

9. SPONSORING/MONITORING AGENCY NAME(S) AND ADDRESS(ES)

Phillips Laboratory
29 Randolph Road
Hanscom AFB, MA 01731-3010

Contract Manager: James Lewkowicz/GPEH

10. SPONSORING/MONITORING AGENCY REPORT NUMBER

PL-TR-93-2072

11. SUPPLEMENTARY NOTES

12a. DISTRIBUTION/AVAILABILITY STATEMENT

Approval for public release: distribution unlimited

12b. DISTRIBUTION CODE

13. ABSTRACT (Maximum 200 words)

The research performed under the contract, during the period 26 September 1991 through 25 September 1992, can be divided into two main topics; using the moment of regional Rayleigh waves and a regional magnitude based on the maximum amplitude of the shear wave train as a seismic discriminant and source retrieval from broadband regional seismograms.

In section 1, we propose using the ratio of M_L (local magnitude) to M_0 (scalar seismic moment) as a regional discriminant analagous to the teleseismic discriminant using the m_b;M_s ratio. We applied this criterion to a data set of 299 earthquakes and 178 explosions and found that this ratio appears to be diagnostic of source type. This method does require the determination of regional crustal models and path calibrations from master events or by other means.

In section 2, we develop and test a method of relocation and source characterization of small earthquakes using one modern regional station. First, we model teleseismic body-waves of two events, which are used as masters. Short period depth phases, pP and sP, are used to establish the epicentral depth, and the events are relocated using calibrated stations and a mantle model derived for this region, TIP. The events moved upward by 12 and 31 kms, respectively. Secondly, these events can be used as "masters" in the calibration of other systems, case-based event characterizations, etc.

14. SUBJECT TERMS

M_L:M_0 Broadband regional seismograms
Seismic discriminants Regional moments
Seismic source retrieval Hindu Kush region

15. NUMBER OF PAGES

94

16. PRICE CODE

17. SECURITY CLASSIFICATION OF REPORT	18. SECURITY CLASSIFICATION OF THIS PAGE	19. SECURITY CLASSIFICATION OF ABSTRACT	20. LIMITATION OF ABSTRACT
Unclassified	Unclassified	Unclassified	SAR

FINAL TECHNICAL REPORT
26 September 1991 - 25 September 1992

ARPA Order No:	5307
Name of Contractor:	California Institute of Technology
Effective Date of Contract:	26 September 1991
Contract Expiration Date:	25 September 1992
Contract Number	F19628-90-K-0049
Principal Investigators:	Donald V. Helmberger (818) 356-6998
	David G. Harkrider (818) 356-6910
Program Manager:	James F. Lewkowicz (617) 377-3222
Short Title of Work	Modeling Regional Seismic Waves

Sponsored by
Defense Advanced Research Projects Agency (DoD)
Nuclear Monitoring Research Office
ARPA Order No. 5307
Issued by the Air Force Geophysics Laboratory under
Contract #F19628-90-K-0049

Seismological Laboratory
Division of Geological and Planetary Sciences
California Institute of Technology
Pasadena, California 91125

Table of Contents

Summary

The research performed under the contract, during the period 26 September 1991 through 25 September 1992, can be divided into two main topics; using the moment of regional Rayleigh waves and a regional magnitude based on the maximum amplitude of the shear wave train as a seismic discriminant and source retrieval from broadband regional seismograms.

In section 1, we propose using the ratio of M_L (local magnitude) to M_0 (scalar seismic moment) as a regional discriminant analagous to the teleseismic discriminant using the m_b;M_s ratio. We applied this criterion to a data set of 299 earthquakes and 178 explosions and found that this ratio appears to be diagnostic of source type. For a given M_0, the M_L of an explosion is more than 0.5 magnitude units larger than that of an earthquake. This separation of populations with respect to source type can be attributed to the fact that M_L is a short-period (1 Hz) energy measurement, whereas seismic moment is determined from long-period body wave phases (period > 4 seconds) and surface waves (10 to 40 seconds). Using regional stations with sources 200 to 600 km away, the effective threshold for magnitude measurements for this discriminant is found to be M_L = 3.1 for earthquakes and M_L 3.6 for explosions. This method does require the determination of regional crustal models and path calibrations from master events or by other means.

In section 2, we develop and test a method of relocation and source characterization of small earthquakes using one modern regional station. First, we model teleseismic body-waves of two events, which are used as masters. Short period depth phases, pP and sP, are used to establish the epicentral depth, and the events are relocated using calibrated stations and a mantle model derived for this region, TIP. The events moved upward by 12 and 31 kms, respectively. The regional waveforms recorded at the IRIS station GAR from the best determined source are forward modeled to establish a local crustal model. A four-layered model with a thickness of 65 km proves effective. Synthetics from this crustal model can then be compared to the data from other events where the depths are poorly known, i.e., PDE depths of 33 km. Forward modeling of the short period phases allows better estimates of depth and makes relocation possible. Next, we perform a long period inversion of whole and partial waveform data to obtain source mechanism and moment, and repeat the procedure if necessary. This technique is applied to events in the tectonically active Pamir-Hindu Kush region to test its usefulness. Five crustal events sampling various azimuths are presented as examples of relocation and determination of source mechanisms from small events. The smallest event has a moment of 5.1 x 10^{22} dyne-cm. For the seven events we studied the average depth correction to PDE is 19 km, and the location correction is 11 km on average. The method can be used to identify earthquakes and thus it lowers the threshold below present m_b:M_S discrimination, since these events are too small to be seen teleseismically. Secondly, these events can be used as "masters" in the calibration of other systems, case-based event characterizations, etc.

SECTION 1

M_L:M_0 as a Regional Seismic Discriminant

M_L:M_0 as a Regional Seismic Discriminant

BRADLEY B. WOODS, SHARON KEDAR AND DONALD V. HELMBERGER

Seismological Laboratory 252-21,

California Institute of Technology

The m_b:M_S ratio determined by teleseismic observations has proven to be an effective discriminant, for explosive sources tend to be significantly richer in short-period energy than earthquakes. Unfortunately, this method is limited by the detection threshold of teleseismic surface waves. However, recent advances in instrumentation allowing low amplitude surface wave measurements coupled with new analytical techniques make it feasible to use regional waveform data to determine the long-period source excitation level of low magnitude events. We propose using the ratio of M_L (local magnitude) to M_0 (scalar seismic moment) as an analogous regional discriminant. We applied this criterion to a data set of 299 earthquakes and 178 explosions and found that this ratio appears to be diagnostic of source type. For a given M_0, the M_L of an explosion is more than 0.5 magnitude units larger than that of an earthquake. This separation of populations with respect to source type can be attributed to the fact that M_L is a short-period (1 Hz) energy measurement, whereas seismic moment is determined from long-period body wave phases (period > 4 seconds) and surface waves (10 to 40 seconds). Using regional stations with sources 200 to 600 km away, the effective threshold for magnitude measurements for this discriminant is found to be M_L = 3.1 for earthquakes and M_L = 3.6 for explosions. This method does require the determination of regional crustal models and path calibrations from master events or by other means.

INTRODUCTION

In this era of increased concern regarding the proliferation of nuclear weapons, the need for effective seismic discrimination techniques is as important as ever. As more countries attain or near the technology threshold needed to develop nuclear weapons, more regions of the world need to be monitored for verification purposes. Effective discrimination methods which can make use of historical seismic data and don't require elaborate, costly large-scale arrays, are of considerable interest.

One of the most successful seismic discriminants proven so far is the classical comparison of body wave magnitude (m_b) to surface wave magnitude (M_S) (Basham, 1969; Lieberman and Pomeroy, 1969; and Marshall, 1971; Stevens and Day, 1985), which exploits the observation that for a given m_b, explosions have a significantly smaller M_S than do earthquakes. This observation implies that explosive sources are richer in high frequency energy than are earthquakes for a given long-period energy level and is attributed, in part, to the differences in characteristic temporal and spatial source dimensions between the two source types. Savino *et al* (1971), Aki *et al* (1974) and Müller (1973) find that explosions exhibit characteristics of an impulsive source. Empirical explosion source models developed by Haskell (1967), and Müller and Murphy (1971) yield source time functions with rise times which are only fractions of second in length. Aki (1967), Brune (1970) and Marshall (1970) find that earthquake source functions, on the other hand, are best-modeled as ramps or step functions with combined duration and rise times greater than one second. Dreger and Helmberger (1991a) found that even moderate-sized earthquakes ($M_L \sim 5.2$) have source durations greater than a second. Stevens and Day (1985) conclude from numerical modeling experiments that the difference between earthquake and explosion source spectra is only partially responsible for

explaining m_b:M_S observations. They also cite focal mechanism, near-source elastic properties and pP interference effects as contributing factors to the separation of populations with this type of discriminant.

The drawback to the m_b:M_S method is the threshold at which teleseismic surface wave magnitudes can be determined and the apparent convergence of populations at small magnitudes. Lieberman and Pomeroy (1969) found the surface wave detection level for earthquakes to be m_b >4.3 and for explosions to be m_b > 4.8, but found that the populations converged below m_b = 5.0 for discrimination purposes. Evernden *et al* (1971) suggest that with high-dynamic-range digital instruments, surface waves from earthquakes with m_b >4.0 (which corresponds roughly to a m_b =5.0 explosion) can be measured out to 6000 km to 7000 km - distances at which well-dispersed 20 sec. surface waves can be measured. Broadband, high-dynamic-range seismic stations, such as those in the IRIS network achieve this observational capability.

Below these threshold levels the surface wave signals are within the noise level and analogous discriminants using regional phases must be employed. Evernden *et al* (1971), Lambert and Alexander (1971), and Peppin and McEvilly (1974) found that they could distinguish between source types on the basis of regional P_n amplitude (or $m_{b(Pn)}$) to regional Airy phase Rayleigh wave amplitude (or magnitude) comparisons for events down to $m_{b(Pn)}$ = 3.6 to 4.0 - the detection threshold for explosion generated surface waves.

Two significant advances in observational seismology occurred since these studies: one is the large-scale upgrade and augmentation of seismic networks with broadband, high dynamic range instruments; the other is the increased sophistication in source parameterization of earthquakes and explosions in terms of the excitation of Green's functions and the seismic

moment tensor solutions(Dziewonski *et al.* 1981), which more precisely quantify seismic sources. With several three component, broadband stations it is feasible to invert for the source function using regional body waves (Dreger and Helmberger, 1990 & 1992), surface waves (Kanamori and Given, 1981; Thio and Kanamori, 1992; Patton, 1988) or a combination of the two wave types (Zhao and Helmberger, 1993). M_0 should better reflect the long-period source characteristics of a source than does M_S, so that its use should improve discriminants which make use of long-period seismic phases.

We re-examine the utility of short-period vs. long-period energy measures in the context of regional seismic records. Figure 1 displays the study area, which includes central and southern California, western Nevada and northern Baja, Mexico. Waveform data is presented in this paper for the events shown in the figure (stars). This region is unique in that there is a large amount of natural seismicity, as well as that of Nevada Test Site (NTS) explosions and their aftershocks. The large number of seismic networks monitoring this regions has created a wealth of data useful for discrimination studies.

With M_0 serving as a long-period energy measure, we employ the classical local magnitude, M_L, (Richter, 1935 & 1958) as a measure of short-period energy. M_L is computed from the peak horizontal displacements on a Wood-Anderson torsion instrument, which is a high pass filter peaked around 1.0 second. Teleseismic P-wave phases measured to determine body-wave magnitudes are typically of the same period, so M_L, too, can be considered a fair measure of the short-period source spectrum. There are several advantages of using M_L. One is that it is a simple measurement to make and is easy to obtain to very small magnitudes. Secondly, it is a routine source quantification used by many seismic networks. We will make use of M_L magnitudes from several network catalogs. One drawback to measuring M_L is that

it is not determined from a particular seismic phase. Normally it is a measure of shear-wave amplitude, but depending on distance and source spectrum for extreme circumstances, a P-wave or surface wave may be the largest amplitude phase on a short-period record.

From visual inspection of broadband recordings of regional earthquakes and explosions it is apparent that these two source types show distinctly different spectral content. Figure 2a compares records of the explosion Kearsarge (the 150 kt, m_b = 5.5, Joint Verification Event detonated at Pahute Mesa) to two earthquakes: Lee Vining (10/24/90, m_b = 5.0) and Little Skull Mountain (6/29/92, m_b = 5.7). The three events, all recorded digitally at Pasadena, California (PAS), have roughly the same epicentral distance (see Figure 1). For each event the broadband displacement records are displayed (middle trace), as well as the displacements convolved with a Press-Ewing 30-90 (PE) long-period instrument (top trace) and with a Wood-Anderson short-period (WA) instrument (bottom trace). Peak amplitudes are to the right of each trace. For Kearsarge, the ratio of peak short-period (WA trace) to long-period (PE trace) amplitude is 0.325, 0.265 and 0.625 for the vertical, radial and tangential component, respectively. On the long-period tangential component, no fundamental Love wave is apparent; only later arriving, higher frequency, higher mode waves (L_g and possibly multi-pathing crustal waveguide surface waves) are evident. The absence of a Love wave is also evidence of an isotropic source, since explosions, in the absence of tectonic strain release do not generate long-period SH waves. For Lee Vining the ratio of peak short-period to long-period amplitude is 0.152, 0.223 and 0.210 for the vertical, radial and tangential components. The tangential component also has a large fundamental mode Love wave. For Little Skull Mountain the ratio of peak short-period to long-period amplitude is 0.0451, 0.0433 and 0.0872 for the vertical, radial and tangential components. Again a large

Love wave is observed. Of these three events, the explosion has the largest short-period to long-period amplitude ratio for each component.

Figure 2b shows an analogous plot of seismograms recorded at the digital station Goldstone, California (GSC), for the explosion Bexar (m_b =5.6 and detonated within a kilometer of the Kearsarge shot point) and the two earthquakes of Figure 2. As with Kearsarge, little or no long period Love wave is evident on the tangential component; only shorter period crustal waveguide surface waves are visible. The ratio of peak short-period to long-period amplitude for Bexar is 0.379, 0.794 and 0.794 for vertical, radial and tangential component, respectively. For Lee Vining the ratio of peak short-period to long-period amplitude is 0.221, 0.189 and 0.0694 for the vertical, radial and tangential components. For Little Skull Mountain the respective ratios are 0.0989, 0.394 and 0.455. Again, the explosion has the largest short-period to long-period amplitude ratio for each component.

Another comparative difference between the explosions and earthquakes in these figures is the spectral content of the Rayleigh waves. The explosion Rayleigh waves exhibit large, relatively short-period (3 to 8 sec.) "ringing" or coda waves after the Airy phase, whereas the earthquakes display primarily the dominant long-period Airy phase. This effect is believed to be a depth dependent phenomena. Kafka (1990) found, in a study of New England earthquakes and quarry blasts, that shallow events produce larger short-period (0.4 to 2.5 Hz) R_g waves than do deeper events. Such Rayleigh wave information is useful as a depth discriminant to help distinguish source types.

These sets of records corroborate the observation that explosions are richer in short-period energy relative to long-period energy as compared to earthquakes. Events recorded at both PAS and GSC have been plotted in order to illustrate that this observation is path inde-

pendent. Of the network shown in Figure 1, only PAS and GSC recorded the Lee Vining event. We shall show, using a large data set, that this spectral difference becomes even more evident after applying propagational corrections and can be used as an effective regional discriminant.

Data Analysis and Results

We compiled seismic moments (M_0) and local magnitudes (M_L) for NTS explosions and earthquakes throughout the western United States and northern Baja California, Mexico from many sources. M_L values were taken from the CIT and Berkeley catalogs, and from the Northwestern Mexico Seismic Network (Vidal and Munguia, 1991). For recent events (1988-1992) in Nevada and the California-Nevada Border region, M_L's were determined from the array of eight broadband stations shown in Figure 1. To calculate these M_L's, an attenuation curve developed by Kanamori *et al* (1992) was used. All the M_L's used were determined in essentially the same fashion.

The seismic moments collected for this study, however, were determined through a variety of means. Dreger and Helmberger (1990, 1991a, 1991b, & 1992), Ma and Kanamori (1991), and Zhao and Helmberger (1993) inverted local and regional broadband waveforms to obtain source parameters, including moment. Cohn *et al* (1982) forward modeled near-field broadband records to determine earthquake moments. Moments determined from combined regional phase (P_{nl}) and teleseismic body waves (P and SH) studies were also gathered. Bent and Helmberger (1991) used a combination of forward modeling comparative amplitude ratios to estimate moments for historical southern California We also included moments and local magnitudes compiled from various source studies for historical western United States earthquakes (Doser and Smith, 1989; Doser, 1990).

Moments from several short-period array source studies were incorporated into our data set. Mori and Frankel (1990) obtained moment estimates from deconvolved displacement pulses. Employing the method of Brune (1970), several studies calculated M_0 from the low frequency amplitude of shear wave spectra (Johnson and McEvilly, 1974; Fletcher *et al*, 1984; Frankel, 1984; Vidal and Munguia, 1991).

Surface wave moments were also obtained from a variety of sources. Thio and Kanamori (1992) obtained source parameters from broadband TERRAscope data for earthquakes throughout southern California for a wide range of magnitudes. Their inversion method uses both Rayleigh wave and Love wave spectra and employs the technique of Kanamori and Given (1981). Patton and Zandt (1991) determined moment tensor solutions for earthquakes throughout the western U. S. using a linear moment inversion scheme developed for Rayleigh wave spectra by Romanowicz (1982) and extended to Love wave spectra by Patton (1988). Wyss and Brune (1968) determined moments from Love wave spectra for central California events.

Table 1 is a list of the local magnitudes and log-moments for earthquakes for which source parameters were determined from broadband data. It includes all available data from the studies by Dreger and Helmberger (1990, 1991a, 1991b, 1992), Ma and Kanamori (1991), and Thio and Kanamori (1992).

Table 2 lists of the local magnitudes and log-moments for explosions cited in this study. Seven explosion moments were determined from near-field observations (Aki *et al*, 1974; Helmberger and Hadley, 1981; Stump and Johnson, 1984; and Johnson, 1988), although most were obtained from surface wave studies. Stevens (1986) calculated spectral moments from Rayleigh wave spectra for large NTS explosions. Given and Mellman (1986) performed

moment tensor inversions of large NTS blasts, too, using the path structures developed by Stevens (1986). They used Rayleigh wave and Love wave spectra to solve for the isotropic source as well as a double couple source associated with tectonic release. The data sets for these last two studies overlap substantially. The moment values were found to be similar, so that for events for which two moments were available, the Stevens' (1986) moment was used.

Time domain surface wave moments of explosions were also included in this study. Woods and Harkrider (1993) determined moments from the peak to peak amplitude (PPA) of the dominant Airy phase of the Rayleigh wave for NTS explosions. With their technique, moment is determined from the ratio of the observed PPA to that of a synthetic seismogram with a given input moment. Figure 3 plots comparisons of observed vs. modeled vertical Rayleigh waves for the 55 station network used in their study. Data from representative Pahute Mesa NTS explosions, with little or no tectonic release, are the upper, darker traces. The synthetics seismograms were generated with a step moment source buried at 0.6 km, a typical shot depth. Many of the path structures used were taken from the Stevens (1986) study. Other paths were determined by inverting Rayleigh wave dispersion data. It can be seen that the waveform fits are good, in that dispersion and amplitude are both well-modeled. The correlation between moments obtained by this time domain moment and a more standard spectral scheme performed on a 108 event subset of this study is very good (see Woods and Harkrider, 1993), implying that this time domain moment method yields accurate, robust moment measurements. Using this method we obtained moments for other small NTS events.

Figure 4a displays M_L vs. log Moment (N-m) plotted for 299 earthquakes and 178 explosions. Solid symbols represent earthquakes, while open symbols and crosses represent NTS

explosions. Moments determined from near-field body wave studies are plotted as circles. Earthquake moments determined from surface wave studies and body wave studies are represented by triangles and diamonds, respectively. Explosion moments determined from surface source studies are denoted by stars (Given and Mellman, 1986), squares (Stevens, 1986) and crosses (Woods and Harkrider, 1993). This figure shows how well this discriminant works. There is a significant separation of earthquakes and explosions, with no real overlap of the two populations. This discriminant also works at all scales, with explosions and earthquakes following their respective scaling laws over a wide range of magnitudes and moments; for earthquakes this is true over seven and a half orders of magnitude. It should be noted that the earthquakes with a $\log(M_0)$ below 13.0 were determined from local stations (D < 75 km) and would not be detectable at regional distances. They are included here only to show the continuity of the linear scaling relationship between M_L and $\log(M_0)$ for earthquakes.

Figure 4b is a blow-up of the portion of Figure 4a containing explosion data. It is important to note when examining these two plots that the data are taken from a number of sources. M_L's were determined from different networks and the moments were calculated in a variety of ways. Yet a distinct separation of the two populations is still obtained. There is one anomalous explosion, Buggy (M_L = 3.96, $\log(M_0)$=14.28), which lies very close to the earthquake population. This was a Plow Shares event in which four nuclear charges with an announced combined yield of 5.4 kt were detonated. We would expect that a multiple-source event like this one would display characteristics similar to a distributed earthquake source, *i.e.* it should be enriched in long-period energy relative to a point source explosion of the same yield.

Discussion and Conclusions

The M_L:M_0 criterion appears to be a robust method to discriminant regional seismic events. For a given moment, the M_L of an explosion is more than 0.5 units larger than that of an earthquake. This difference can be attributed to M_L being a short-period (1 Hz) energy measurement, whereas the moment is determined from long-period body wave phases (period > 4 seconds) and Rayleigh waves (10 to 40 seconds).

There are several explanations for the observed difference in short-period:long-period spectral character between earthquakes and explosions. Earthquakes tend to be asperity-driven distributed sources, as opposed to explosions which can more aptly be modeled as point-sources with impulsive time functions. Dreger and Helmberger (1991a) showed that broad-band seismograms from small local earthquakes ($4.0 < M_L < 5.0$) can be modeled as distributed finite sources rather than as point-sources. Such distributed slip time functions will generally result in reduced high-frequency spectra relative to a point-source step moment. It is possible that even very small earthquakes (M_L <4) behave similarly. Another possible reason that this discriminant works at low magnitudes is that for small events the quantities being measured are the P-wave low frequency spectrum (M_L) and the S-wave low frequency spectrum (M_0), in which case, for explosions, the S-wave energy is predominantly generated by secondary P to S converted phases. If this is so, the moment should not be determined solely from P-wave information.

Spall effects may also be a cause of observed high-frequency (0.15 Hz < f < 2.0 Hz) enrichment of explosion source spectra. Theoretical results (Day and McLaughlin, 1991) and various observational studies (Viecelli, 1973; Stump, 1985; Taylor and Randall, 1989; and Patton, 1990) conclude that spallation can be a significant contributor to short period

energy, while Patton (1988) and Day *et al* (1983) find no appreciable spall energy at periods greater than 8 seconds. Spall energy would tend to increase M_L measurements.

This discriminant is only limited by the detection threshold capability of long-period data, as the two populations do not converge at small magnitudes. This observation implies that the convergence in the M_S:m_b ratio for small magnitude events seen in some previous studies is due to approaching the effective signal to noise level for measuring surface amplitudes. Previous studies relied on data recorded on lower grade (usually analog) instruments that did not have the recording capabilities of modern, high dynamic range, digital seismometer systems. Modern data combined with digital processing techniques increases the resolution of long-period transient signals. Figure 5 shows the Yucca Flat blast Floydada recorded at four TERRAscope stations (epicentral distances being between 200 and 400 km), played-out with PE and WA instruments. The amplitudes indicate that these signals would not be discernible on the actual analog instruments. M_L for this event is 4.0 and its log moment is 14.20. Assuming it is a shallow explosion above the water table, the yield can be inferred to be less than 10 kt from the moment-yield scaling relationships determined for NTS by Woods and Harkrider (1993). Were it detonated in hard rock below the water table, it would correspond to a two kiloton explosion. We estimate that were this event 2.5 times lower in yield it would still be possible to obtain its moment, yielding a magnitude threshold of $M_L >$ 3.6 for explosions.

Low SNR seismograms also may be phase match filtered (Herrin and Goforth, 1977; and Stevens, 1986a) in order to retrieve the signal of very small events for spectral amplitude estimates. However, there is some debate on the accuracy of using this method, see Der (1986) and Stevens (1986b) for a discussion of this problem. Employing one or another

means of time domain measurements in order to obtain the seismic moment avoids such problems.

Simple time domain moment measurements included in this study are straightforward and can be directly applied to historical analog data sets in order to establish earthquake M_L:M_0 curves for other regions. Since only peak amplitude measurements are necessary for such methods, the required signal to noise ratio (SNR) effectively decreases, too. Time domain peak amplitude measurements are also less susceptible to noise contamination than are spectral amplitude measurements. The other parameter M_L is a simple time-domain measurement which can be made on the smallest detectable seismic sources. Modern source inversion techniques that make use of regional body wave phases (such as P_{nl} and S_{nl}) recorded at sparse regional networks also make for powerful moment determination tools as shown in studies using the TERRAscope broadband network (Dreger and Helmberger, 1992; and Zhao and Helmberger, 1993).

A disadvantage to determining moment tensor solutions is that many methods require Green's functions in order to obtain accurate moments. However, with modern broadband, high dynamic range instrumentation it is quite feasible to use moderate-sized to small events to determine regional path structures. Zhao and Helmberger (1991) detail the forward modeling of P_{nl}, S_{nl} and Rayleigh wave regional phases along a continental shield path. Dreger and Helmberger (1990) were able to forward model velocity structure using waveform data from small (m_b = 3.7 - 4.0) local events. Shallow crustal structure can also be inferred from the inversion of surface wave dispersion data generated by small, regional seismic sources (Saikia *et al.* 1990) as well as in conjunction with teleseismic surface waves (Thio and Kanamori, 1991). These path structures needn't be overly complicated or detailed. Dreger and Helm-

berger (1991b, 1992) found that they could model broadband regional body-wave phases from events located throughout Southern California and recorded at various TERRAscope stations with one relatively simple crustal model (with an underlying mantle half-space). Using their regional Green's functions in conjunction with a time-domain source inversion method yielded source parameter solutions consistent with other studies. Zhao and Helmberger (1993) extended this technique to include surface waves and found that this inversion scheme worked well with simple regional earth models as well.

An important point to address concerns the *a priori* source type assumptions made in determining the seismic moments. All earthquake moments were determined assuming either a double couple source (for moment tensor and Green's function inversion methods) or a circular fault model (for corner frequency moment estimates). Most of the the NTS explosion moments were determined by modeling the Rayleigh waves as being generated by a shallow, isotropic source excitation function in the absence of an azimuthally dependent radiation pattern. The Given and Mellman (1986) moments, however, were determined by inverting Rayleigh and Love wave spectra to obtain the isotropic and double couple components of the moment tensor solution. An obvious problem with classifying events with respect to their M_L:M_0 ratio is that for an unidentified seismic event one doesn't know which source model to assume in order to estimate the moment. This point leads to the question, how distinguishable would the two populations be, had they all been treated as double couple sources for moment estimation purposes? For a given seismic moment, the average radiation pattern amplitude (assuming absolute values) for Rayleigh waves generated by a predominantly strike-slip fault motion ($sin2\theta$ radiation pattern) is only slightly larger (by 10 percent) than that of an explosion. In this case one could still infer the source type

from the moment estimate. For such strike-slip earthquakes, observations from all azimuthal quadrants (the four lobes of the $sin2\theta$ radiation pattern) will result in better constrained moment determinations.

The difficulty occurs in modeling the Rayleigh waves assuming a shallow source with a dip-slip orientation for which there is a singularity in the Green's function solutions. In this special case we would obtain a larger moment and the event's M_L - M_0 ratio would decrease towards the earthquake population. However, one can generally model and invert for earthquake sources that occur deeper than 3 km. When an event does not fit our regional Green's functions to some specified degree, we would assume it is shallow and model it as a vertical strike-slip earthquake. Thus, explosions would still discriminate as displayed above and shallow strike-slip earthquakes would still lie within in the earthquake population. M_0 for a shallow dip-slip earthquake, however, may be underestimated and could potentially fall within the explosion population. In a monitoring environment we would have a problematic event, to which other discrimination criterion would need to be applied in order to identify it correctly.

Applying the M_L:M_0 ratio in conjunction with other discriminants would yield a more effective source identification scheme. Phase information (*i.e.* Rayleigh wave polarity) and Love wave data would be helpful in such cases, since reversed polarity Rayleigh waves and/or large Love wave amplitudes are diagnostic of a double couple source. A depth discriminant, based on the complexity and amplitude of the Rayleigh wave tail (coda) for example, would be useful for depth constraints to be placed on the moment tensor inversion of a source. In a related study Woods and Helmberger (1992) found that the ratio of short-period energy in the vertical component *Pnl* wave train to that in the long-period surface wave train

(summed over all three components) of regional seismograms also separates source populations, although it, too, suffers similar magnitude threshold limitations.

For very small events information from high-frequency (f > 1 Hz) phases may be needed to compliment the M_L:M_0 discriminant. Comparisons of L_g spectral amplitude levels for different bandwidths (in the 0.5 to 8 HZ range) have been shown to effectively discriminate events with magnitudes down to $m_{b(P_n)} = 3.3$ (Murphy and Bennett, 1982); Taylor *et al*, 1988). Although the M_L:M_0 discrimination threshold is slightly higher than this, the regional body wave phases and Rayleigh waves used in this method are not as susceptible to path "blockage" effects as is the L_g phase. Also, using relatively close-in stations for surface wave measurements, as it is possible to do with this method, path attenuation effects are minimized. The M_L:M_0 ratio discriminant would work well as a companion test, or check, for other, high-frequency, discrimination methods, particularly for events in the $3.5 < m_b < 4.5$ range for which teleseismic methods no longer work.

Because both source parameters used in this discrimination method can be obtained from a sparse broadband network, this discriminant can be applied throughout the world as more broadband stations similar to those of the IRIS network come on line. For an active tectonic region the threshold for this discriminant is $M_L = 3.1$ for earthquakes and $M_L = 3.6$ for explosions for epicentral distances up to 600 km.

Acknowledgments. We wish to thank Riley Geary for the use of explosion M_L's which he has compiled from the CIT catalog. This research was supported by the Defense Advanced Research Projects Agency (DOD), Nuclear Monitoring Research Office and was monitored by Air Force Geophysics Laboratory under Contract F29601-91-K-DB14 and also was supported by Phillips Laboratory of the Air Force Systems Command under Contract F19628-90-K-

0049. Contribution No. 5200, Division of Geological and Planetary Sciences, California Institute of Technology, Pasadena, California.

References

Aki K. (1967). Scaling Law of Seismic Spectrum, *J. Geophys. Res.*, **72**, 1217-1231.

Aki, K., M. Bouchon, and P. Reasenberg (1974). Seismic Source Function for an Underground Nuclear Explosion, *Bull. Seism. Soc. Am.*, **64**, 131-148.

Basham, P.W., (1969). Canadian Magnitudes of Earthquakes and Nuclear Explosions in Southwestern North America, *Geophys. J. R. astr. Soc.*, **17**, 1-13.

Bent, A. L. and D. V. Helmberger (1991). A Re-examination of Historic Earthquakes in the San Jacinto Fault Zone, California. *Bull. Seism. Soc. Am.*, **81**, 2289-2309.

Brune, J. N., 1970. Tectonic Stress and the Spectra of seismic Shear Waves from Earthquakes, *J. Geophys. Res., 75,* 4997-5009.

Cohn, S. N., T.-L. Hong, and D. V. Helmberger (1982). The Oroville Earthquakes: A Study of Source Characteristics and Site Effects, *J. Geophys. Res.*, **87**, 4585-4594.

Day S. M., and K. L. McLaughlin (1991). Seismic Source Representation for Spall, *Bull. Seism. Soc. Am.*, **81**, 191-201.

Day S. M., N. Rimer, and J. T. Cherry (1983). Surface Waves from Underground Explosions with Spall: Analysis of Elastic and Nonlinear Source Models, *Bull. Seism. Soc. Am.*, **73**, 247-264.

Der, Z. A. (1986). Comments on the Paper "Estimation of Scalar Moments from Explosion-Generated Surface Waves" by J. L. Stevens., *Bull. Seism. Soc. Am.*, **76**,

1822-1824.

Doser, D. I. and R. B. Smith (1989). An Assessment of Source Parameters of Earthquakes in the Cordillera of the Western United States, *Bull. Seism. Soc. Am.*, **79**, 1389-1409.

Doser, D. I. (1990). A Re-examination of the 1947 Manix, California, Earthquake Sequence and Comparison to Other Sequences of the Mojave Block, *Bull. Seism. Soc. Am.*, **80**, 267-277.

Dreger, D. S. and D. V. Helmberger (1990). Broadband Modeling of Local Earthquakes, *Bull. Seism. Soc. Am.*, **80**, 1162-1179.

Dreger, D. S. and D. V. Helmberger (1991a). Complex Faulting Deduced from Broadband Modeling of the February 28, 1990 Upland Earthquake (M_L =5.2), *Bull. Seism. Soc. Am.*, **81**, 1129-1144.

Dreger, D. S. and D. V. Helmberger (1991b). Source Parameters of the Sierra Madre Earthquake from Regional and Local Body Waves, *Geophys. Res. Lett.*, **18**, 2015-2018.

Dreger, D. S. and D. V. Helmberger (1992). Determination of Source Parameters at Regional Distances with Three-Component Sparse Network Data, *J. Geophys. Res.* (in press).

Dziewonksi, A. M., T.-A. Chouw and J. H. Woodhouse (1981). Determination of Earthquake Soure Parameters from Waveform Data for Studies of Global and Regional Seismicity, *J. Geophys. Res.*, **86**, 2825-2852.

Evernden, J. F., W. J. Best, P. W. Pomeroy, T. V. McEvilly, J. M. Savino and L. R. Sykes (1971). Discrimination between Small-Magnitude Earthquakes and Explosions, *J. Geophys. Res.*, **76**, 8042-8055.

Fletcher, J., J. Boatwright, L. Haar, T. Hanks and A. McGarr (1984). Source Parameters for Aftershocks of the Oroville, California, Earthquake, *Bull. Seism. Soc. Am.*, **74**, 1101-1123.

Frankel, A. (1984). Source Parameters of Two $M_L \sim 5$ Earthquakes Near Anza, California and a Comparison with an Imperial Valley Aftershock, *Bull. Seism. Soc. Am.*, **74**, 1509-1527.

Given, J.W. and G.R. Mellman (1986). Estimating Explosion and Tectonic Release Source Parameters of Underground Nuclear Explosions from Rayleigh and Love Wave Observations, *DARPA Report AFGL-TR-86-0171 ADB110040.*

Haskell, N. A. (1967). Analytic Approximation for the Elastic Radiation from a Contained Underground Explosion, *J. Geophys. Res.*, **72**, 2583-2586.

Helmberger, D. V. and D. M. Hadley (1981). Seismic Source Functions and Attenuation from Local and Teleseismic Observations of the NTS Events JORUM and HANDLEY, *Bull. Seism. Soc. Am.*, **71**, 51-67.

Herrin, E. and T. Goforth (1977). Phase Matched Filtering: Application to the Study of Rayleigh Waves, *Bull. Seism. Soc. Am.*, **76**, 1259-1275.

Johnson, L. R. and T. V. McEvilly (1974). Near-field Observations and Source Parameters of Central California Earthquakes, *Bull. Seism. Soc. Am.*, **64**, 1855-1886.

Johnson, L. R. (1988). Source Characteristics of Two Underground Nuclear Explosions. *Geophys. J. Int.*, **95**, 15-30.

Kafka, A. L. (1990). R_g as a Depth Discriminant for Earthquakes and Explosions: A Case Study in New England, *Bull. Seism. Soc. Am.*, **80**, 373-394.

Kanamori, H., J. Mori, E. Hauksson, T. H. Heaton, L. K. Hutton and L. M. Jones (1992). Determination of Earthquake Energy Release and M_L Using TERRAscope. submitted to ***Bull. Seism. Soc. Am.***.

Kanamori, H. and J. W. Given (1981). Source Parameters Determined from Long Period Surface Waves, *Phys. Earth Planet. Int.*, **11**, 312-332.

Lambert, D. G. and S. S. Alexander (1971). Relationship of Body and Surface Wave Magnitudes for Small Earthquakes and Explosions, *Final AFTAC Report VELA T/2706, Teledyne Geotech.*

Liebermann, C. R. and P. W. Pomeroy (1969). Relative Excitation of Surface Waves by Earthquakes and Underground Explosions, *J. Geophys. Res.*, **74**, 1575-1590.

Ma, K. F. and H. Kanamori (1991). Aftershock sequence of the 3 December 1988 Pasadena Earthquake, *Bull. Seism. Soc. Am.*, **81**, 2310-2319.

Marshall, P. D. (1970). Aspects of the Spectral Differences Between Earthquakes and Underground Explosions. *Geophys. J. R. astr. Soc.*, **20**, 397-416.

Mori J. and A. Frankel (1990). Source Parameters for Small Events Associated with the 1986 North Palm Springs, California, Earthquake Determined Using Empirical Green Functions, *Bull. Seism. Soc. Am.*, **80**, 278-295.

Müller, R. A. (1973). Seismic Moment and Long-period Radiation of Underground Nuclear Explosions, *Bull. Seism. Soc. Am.*, **63**, 847-857.

Müller, R. A. and J. R. Murphy (1971). Seismic Characteristics of Undergrond Nuclear Detonations: Part I. Seismic Spectrum Scaling, *Bull. Seism. Soc. Am.*, **61**, 1675-1692.

Murphy J. R. and T. J. Bennett (1982). A Discrimination Analysis of Short-Period Data Recorded at Tonto Forest Observatory, *Bull. Seism. Soc. Am.*, **72**, 1351-1366.

Patton, H. J. (1988). Source Models of the HARZER Explosion from Regional Observations of Fundamental-mode and higher Mode Surface Waves, *Bull. Seism. Soc. Am.*, **78**, 1133-1157.

Patton, H. J. and G. Zandt (1991). Seismic Moment Tensors of Western U. S. Earthquakes and Implications for tectonic Stress Field, *J. Geophys. Res.*, **96**, 18,245-18,259.

Peppin, W. A. and T. V. McEvilly (1974). Discrimination among Small Magnitude Events on Nevada Test Site, *Geophys. J. R. astr. Soc.*, **37**, 227-243.

Richter, C. F. (1935). An Instrumental Magnitude Scale, *Bull. Seism. Soc. Am.*, **25**, 1-32.

Richter, C. F. (1958). *Elementary Seismology*, W.H. Freeman, San Francisco.

Saikia, K. C., A. L. Kafka, S. C. Gnewuch and J. W. McTigue (1990). Shear Velocity and Intrinsic Q Structure of the Shallow Crust in Southeastern New England from R_g Wave Dispersion, *J. Geophys. Res.*, **95**, 8527-8541.

Savino, J. L., L. R. Sykes, R. C. Lieberman and P. Mollnar (1971). Excitation of Seismic Surface Waves with Periods of 15 to 70 seconds for Earthquakes and Underground Explosions, *J. Geophys. Res.*, **76**, 8003-8020.

Stevens, J. L and S. M. Day (1985). The Physical Basis of m_b:M_s and Variable Frequency Magnitude Methods for Earthquake/Explosion Discrimination, *J. Geophys. Res.*, **90**, 3009-3020.

Stevens, J. L. (1986a). Estimation of Scalar Moments from Explosion-Generated Surface Waves, *Bull. Seism. Soc. Am.*, **76**, 123-151.

Stevens, J. L. (1986b). Reply to Z. Der's "Comments on the Paper 'Estimation of Scalar Moments from Explosion-Generated Surface Waves'", *Bull. Seism. Soc. Am.*, **76**, 1825-1829.

Stump, B. W. and L. R. Johnson, (1984). Near-field Source Characteristics of Contained Nuclear Explosions in Tuff, *Bull. Seism. Soc. Am.*, **74**, 1-26.

Stump, B. W. (1985). Constraints on Explosive Sources with Spall from Near-source Waveforms, *Bull. Seism. Soc. Am.*, **75**, 1312-1325.

Taylor, S. R. and G. E. Randall, (1989). The Effects of Spall on Regional Seismograms, *Geophys. Res. Lett.*, **16**, 211-221.

Thio, H. K. and H. Kanamori (1991). A Surface Wave Study on the Structure of the Crust and Upper Mantle Under Southern California, *abstract, Eos Trans AGU*, **72**, no. 14, 321.

Thio, H. K. and H. Kanamori (1992). Moment Tensor Inversions in Southern California Using Surface Waves Recorded by TERRAscope, *abstract, Eos Trans AGU*, **73**, no. 43, 376.

Viecelli, J. A. (1973). Spallation and the Generation of Surface Waves by an Underground Nuclear Explosion, *J. Geophys. Res.*, **78**, 2475-2487.

Vidal, A. and L. Munguia (1991). Local Magnitude and Source Parameters for Earthquakes in the Peninsular Ranges of Baja California, Mexico, *Bull. Seism. Soc. Am.*, **81**, 2254-2267.

Woods, B. B., C. K. Saikia and D. V. Helmberger (1992). An Energy Discriminant for Regional Seismic Events, *Eos Trans AGU*, **73**, no. 43, 359.

Woods, B. B. and Harkrider, D. G. (1993). Determining Surface Wave Magnitudes from Regional NTS Data, submitted to *Geophys. J. Int.*.

Wyss, M. and J. N. Brune (1968). Seismic Moment, Stress, and Source Dimensions for Earthquakes in the California-Nevada Region, *J. Geophys. Res.*, **73**, 4681-4694.

Zhao, L. S. and D. V. Helmberger (1991). Broadband Modelling Along a Regional Shield Path, Harvard Recording of the Saguenay Earthquake, *Geophys. J. Int.*, **105**, 301-312.

Zhao, L. S. and D. V. Helmberger (1993). Source Estimation from Broadband Regional Seismograms, *Bull. Seism. Soc. Am.* (submitted).

Figure 1. Map showing the study area. Broadband stations used to determine M_0 and M_L for 1988+ events are shown with triangles. Events shown in this study are denoted by stars.

Figure 2. **(a)** Broadband displacement (middle trace) records of the JVE event Kearsarge and the Lee Vining and Skull Mountain earthquakes recorded at PAS and played out with long-period (top trace) and short-period (lower trace) instruments. **(b)** Analogous plot for the explosion Bexar and the Lee Vining and Skull Mountain earthquakes recorded at GSC.

Figure 3. Comparison of synthetic and observed fundamental Rayleigh waves for a regional network from which seismic moments were determined. The data are the upper, darker traces. The records chosen came from an ensemble of high-SNR Pahute Mesa events with little or no tectonic release. The synthetics were generated with a step moment isotropic source buried at 0.6 km.

Figure 4. **(a)** M_L vs. log M_0 for 299 earthquakes (solid symbols) and 178 explosions (open symbols and crosses). Circles are moments from near-field source studies. Triangles are surface wave moments and diamonds are body wave moments. Explosion moments determined from surface waves are shown as stars (Given and Mellman, 1985), squares (Stevens, 1986a) and crosses (Woods and Harkrider, 1992). **(b)** Blow-up of that part of the plot which contains explosions.

Figure 5. A small Yucca Flat explosion, Floydada (M_L=4.0), recorded at TERRA-scope stations and played out on Press-Ewing (long-period) and Wood-Anderson (short-period) instruments.

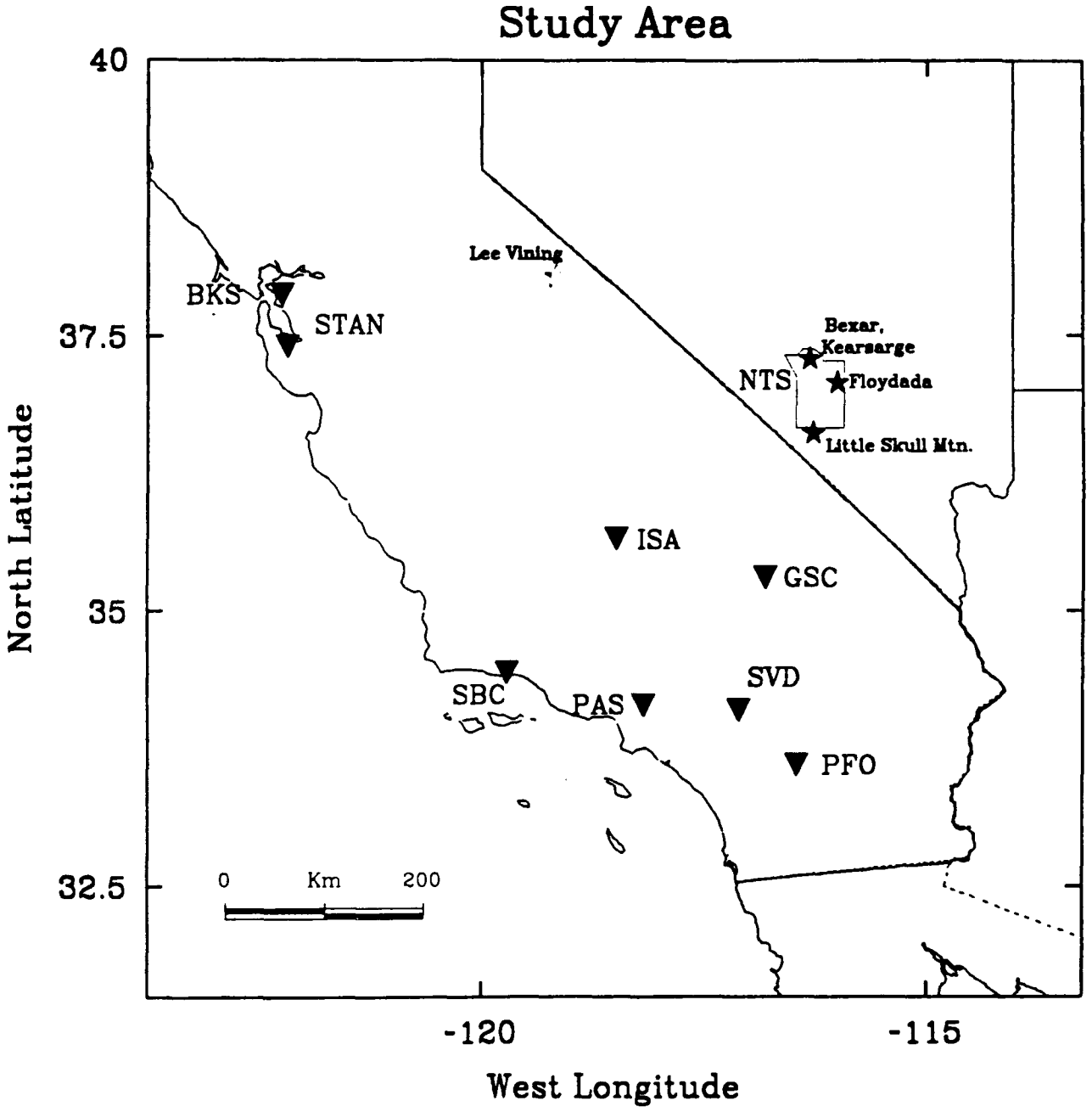
Study Area
40
37.5
35
32.5
North Latitude
-120
-115
West Longitude
BKS
STAN
Lee Vining
Bexar,
Kearsarge
NTS
Floydada
Little Skull Mtn.
ISA
GSC
SVD
SBC
PAS
PFO
0
Km
200

Figure 1

Kearsarge, Lee Vining and Little Skull Mtn at PAS

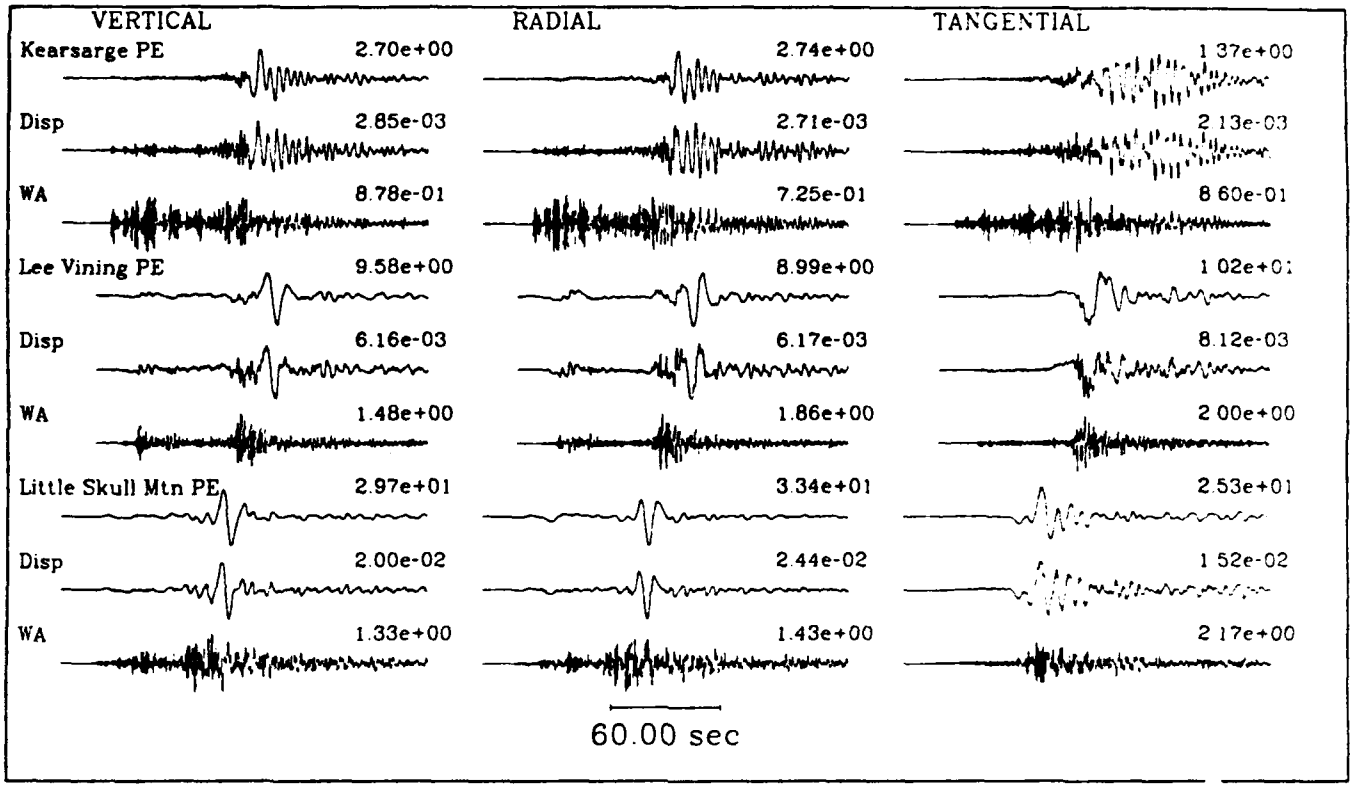

Figure 2a

Bexar, Lee Vining and Little Skull Mtn at GSC

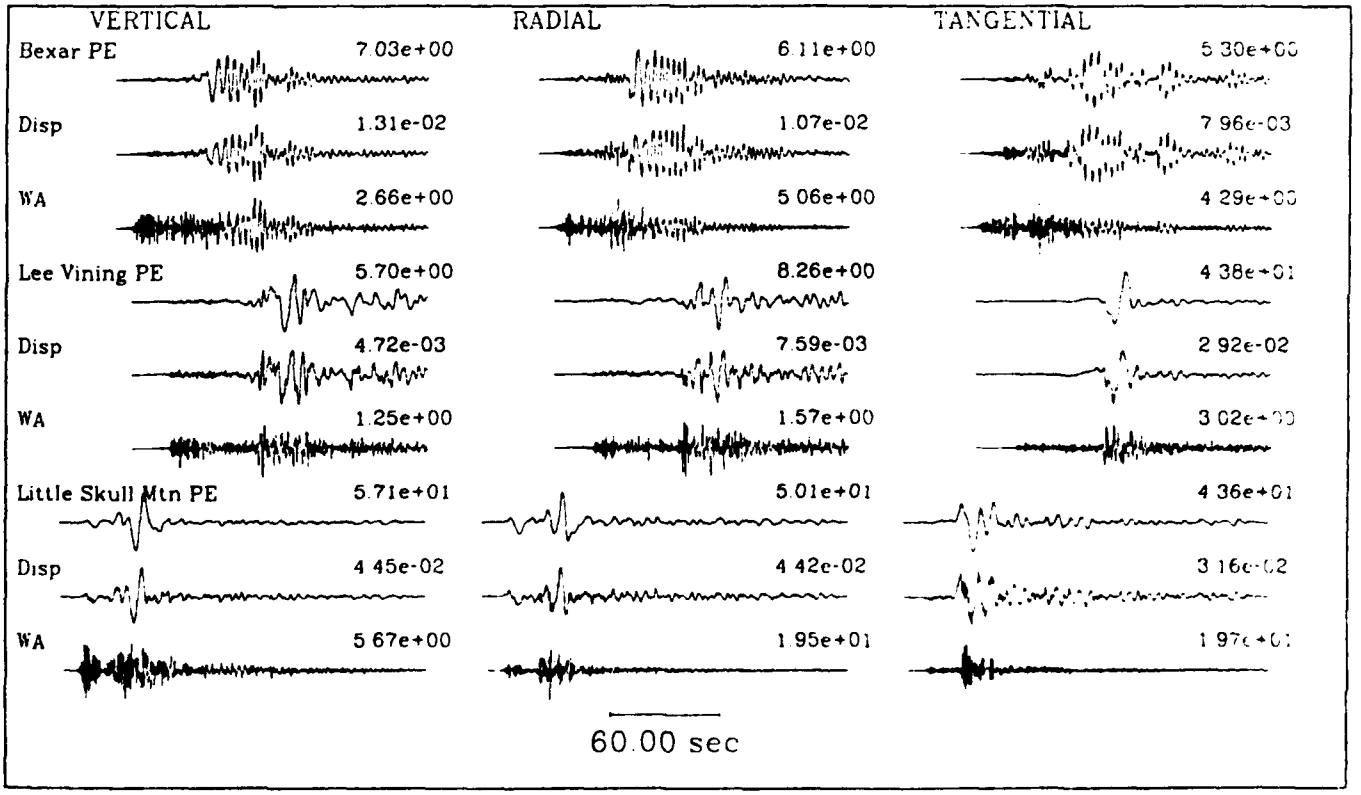

Figure 2b

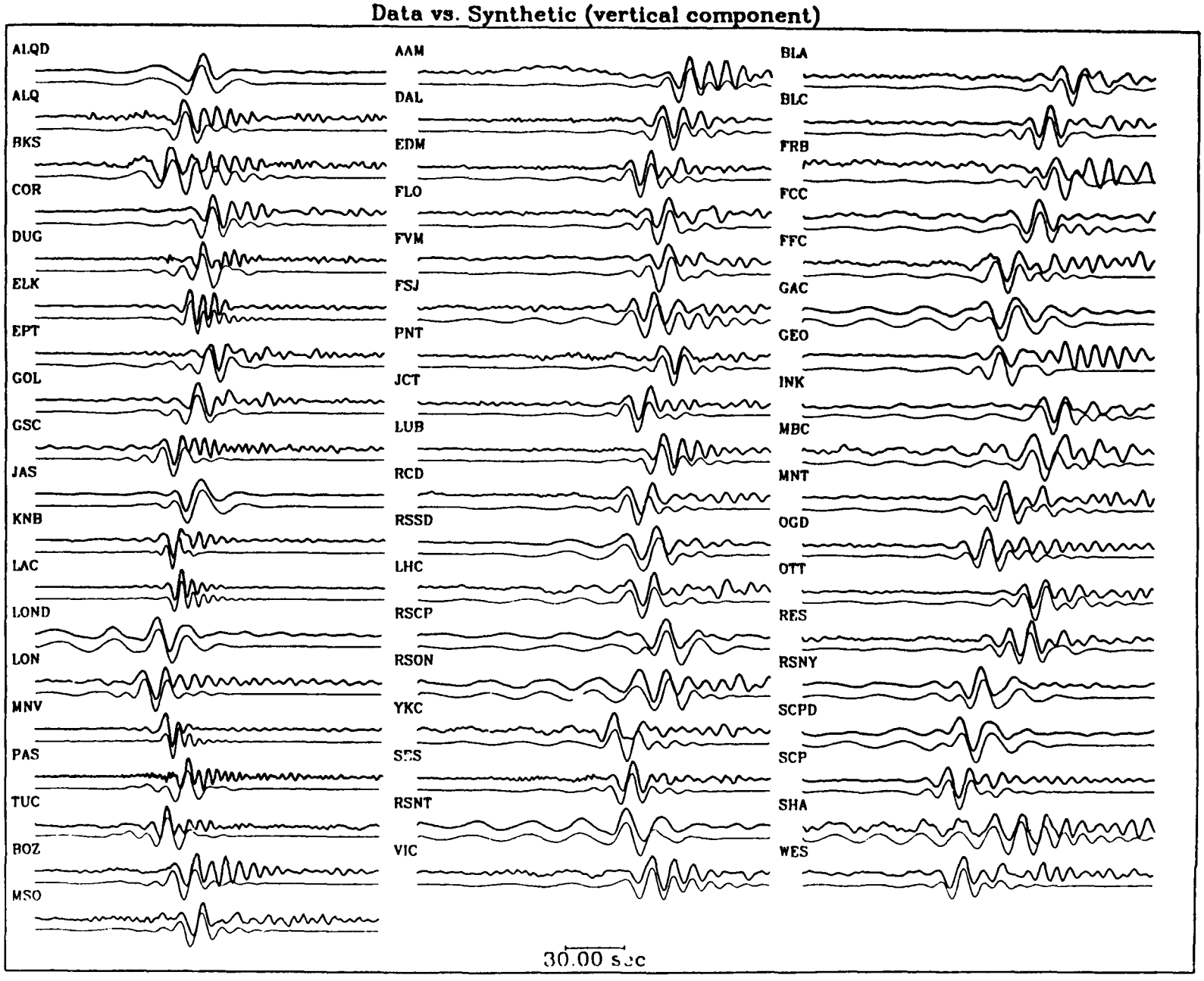
Data vs. Synthetic (vertical component)
ALQD
ALQ
BKS
COR
DUG
ELK
EPT
GOL
GSC
JAS
KNB
LAC
LOND
LON
MNV
PAS
TUC
BOZ
MSO
AAM
DAL
EDM
FLO
FVM
FSJ
PNT
JCT
LUB
RCD
RSSD
LHC
RSCP
RSON
YKC
SCS
RSNT
VIC
BLA
BLC
FRB
FCC
FFC
GAC
GEO
INK
MBC
MNT
OGD
OTT
RES
RSNY
SCPD
SCP
SHA
WES
30.00 sec

Figure 3

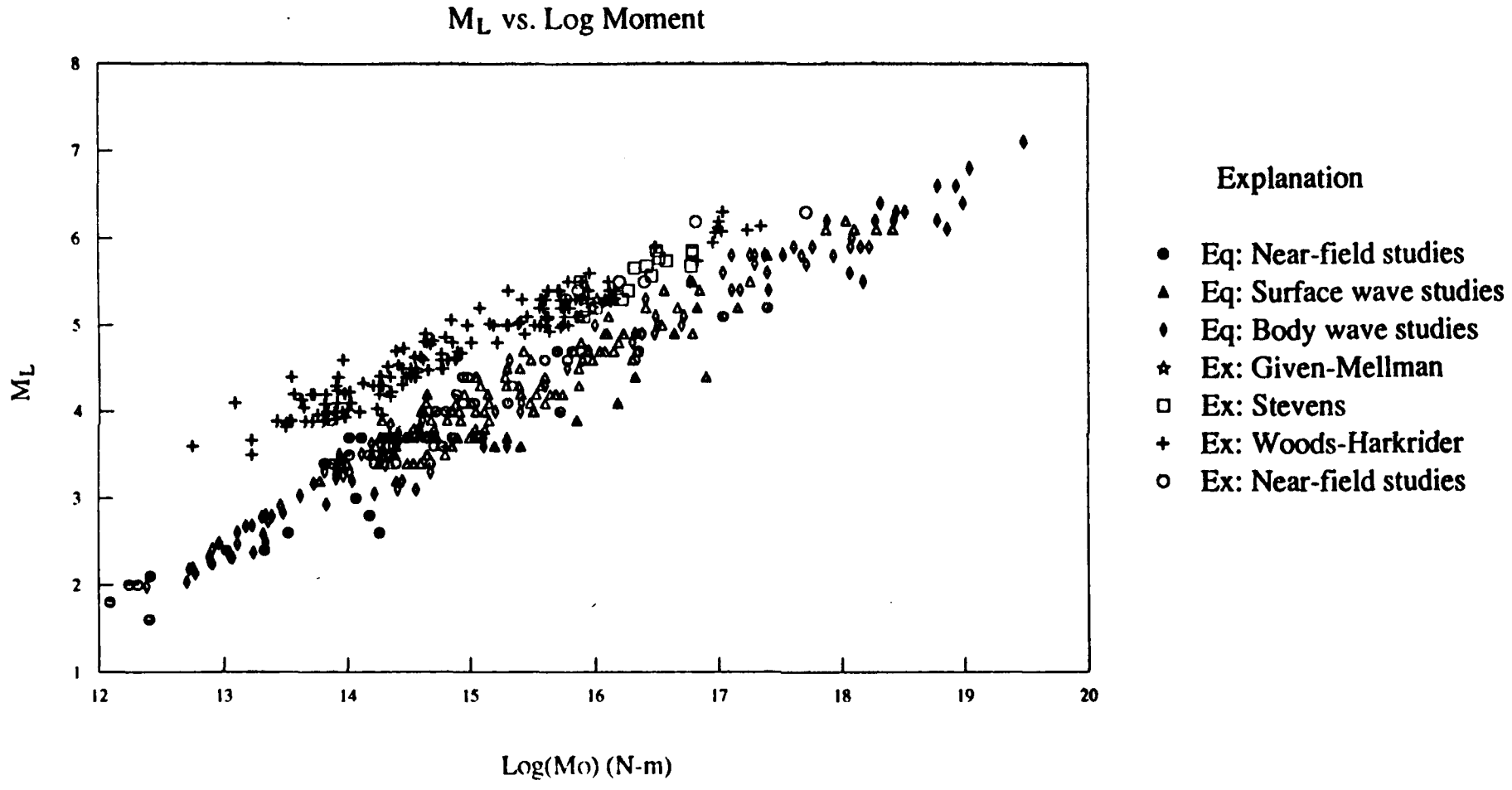
M_L vs. Log Moment
M_L
Log(Mo) (N-m)
8
7
6
5
4
3
2
1
12
13
14
15
16
17
18
19
20
Explanation
Eq: Near-field studies
Eq: Surface wave studies
Eq: Body wave studies
Ex: Given-Mellman
Ex: Stevens
Ex: Woods-Harkrider
Ex: Near-field studies

Figure 4a

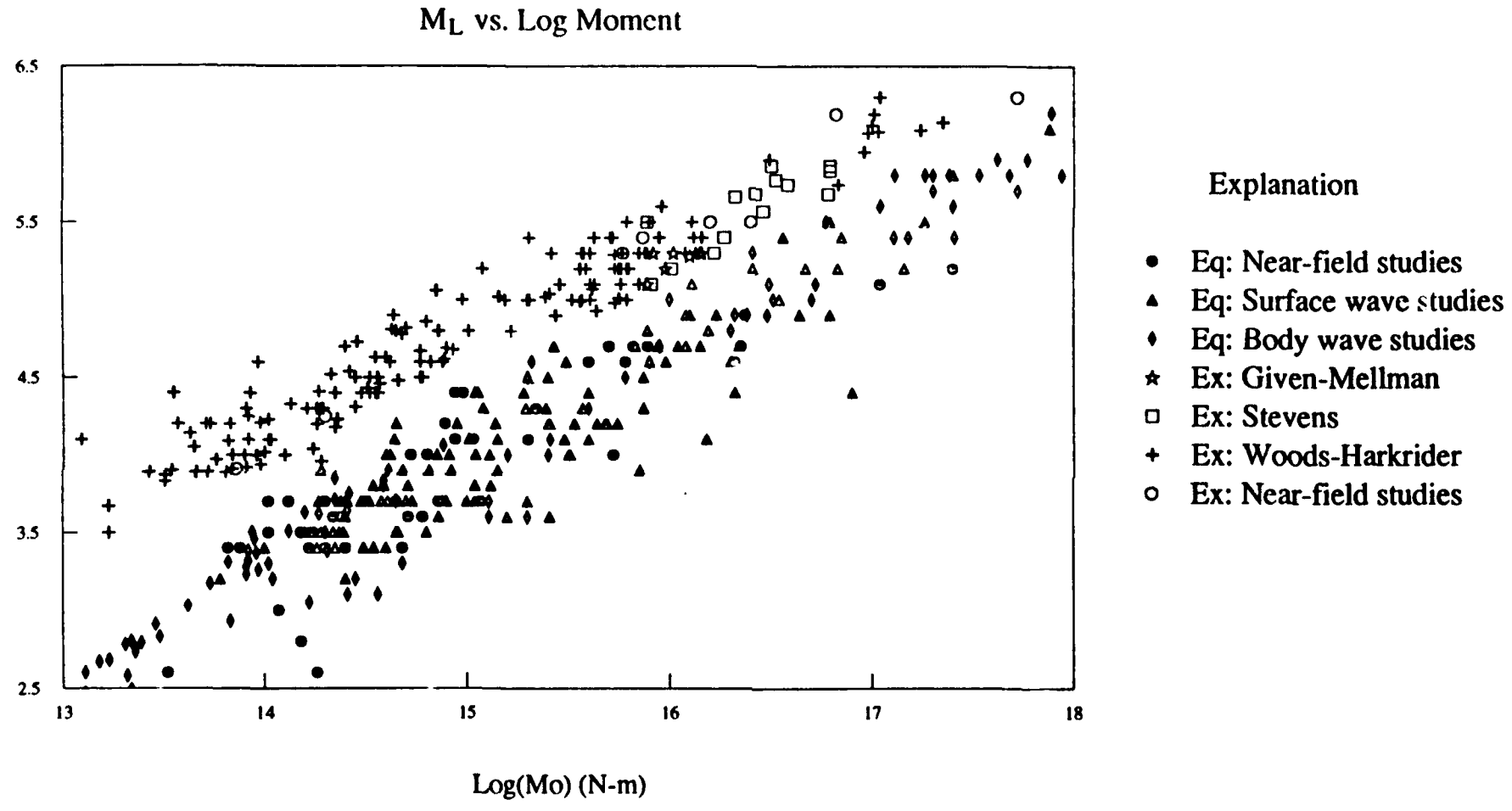
M_L vs. Log Moment
6.5
5.5
4.5
3.5
2.5
M_L
13
14
15
16
17
18
Log(Mo) (N-m)
Explanation
Eq: Near-field studies
Eq: Surface wave studies
Eq: Body wave studies
Ex: Given-Mellman
Ex: Stevens
Ex: Woods-Harkrider
Ex: Near-field studies

Figure 4b

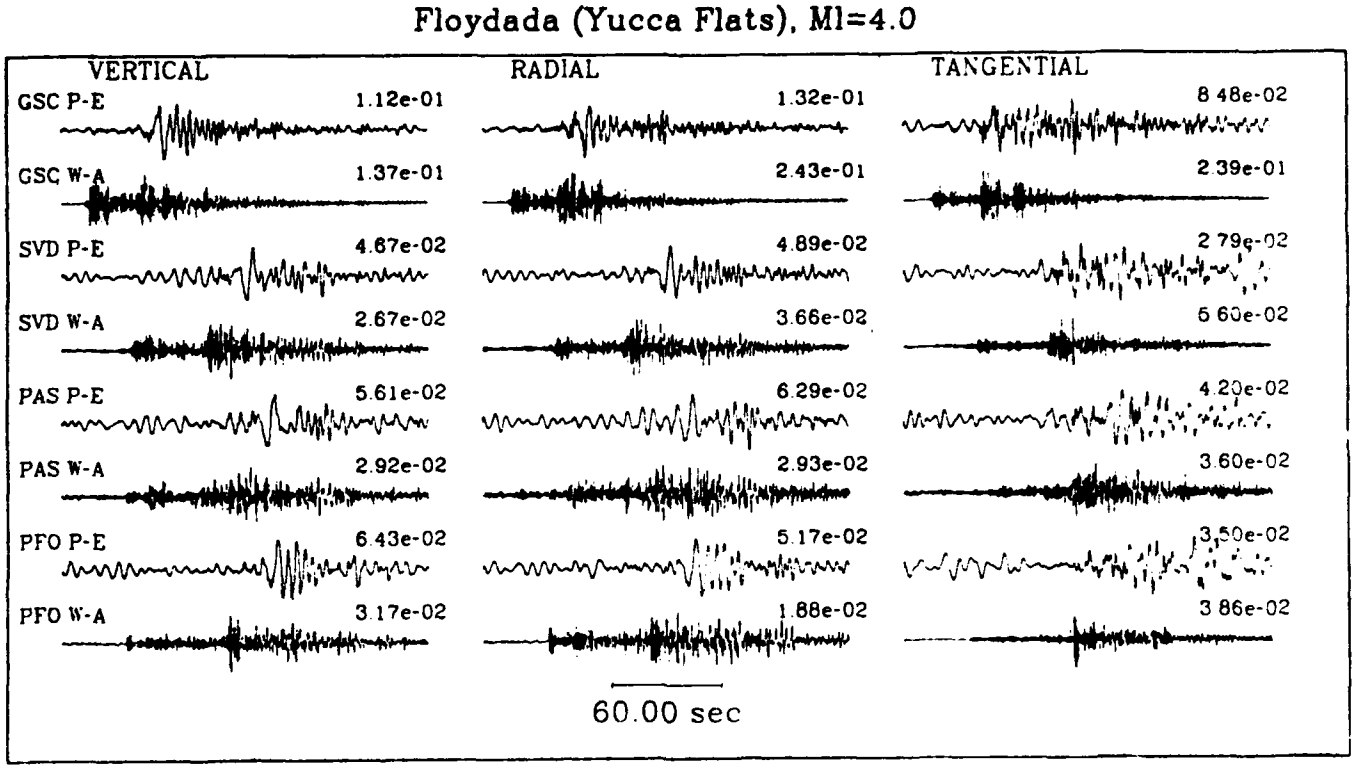
Floydada (Yucca Flats), Ml=4.0
VERTICAL
RADIAL
TANGENTIAL
GSC P-E
1.12e-01
1.32e-01
8.48e-02
GSC W-A
1.37e-01
2.43e-01
2.39e-01
SVD P-E
4.67e-02
4.89e-02
2.79e-02
SVD W-A
2.67e-02
3.66e-02
5.60e-02
PAS P-E
5.61e-02
6.29e-02
4.20e-02
PAS W-A
2.92e-02
2.93e-02
3.60e-02
PFO P-E
6.43e-02
5.17e-02
3.50e-02
PFO W-A
3.17e-02
1.88e-02
3.86e-02
60.00 sec

Figure 5

Table 1: Earthquakes with Moments Determined Using Broadband Data

Date	M_L	$\log(M_0)$	Event	Date	M_L	$\log(M_0)$	Event
88/06/10	5.4	17.11 [a]	Gorman	92/03/03	3.4	14.49 [a]	Walker Pass
88/06/26	4.6	15.78 [d]	Chino	92/03/04	4.2	15.14 [a]	San Clemente
88/06/27	5.5	16.77 [c]	San Juan Botista	92/03/05	3.8	14.59 [a]	Bakersfield
88/07/06	3.7	14.88 [d]	Chino A.S.	92/04/10	3.4	14.60 [a]	Borrego
88/12/03	4.9	16.38 [b]	Pasadena M.S.	92/04/15	3.4	14.00 [a]	Lytle Creek
11:49:	2.1	12.41 [b]	Pasadena A.S. 1	92/04/23	4.6	15.49 [a]	Joshua Tree F.S.
12:08:	2.0	13.02 [b]	Pasadena A.S. 3	92/04/23	6.1	18.29 [a]	Joshua Tree M.S.
12:13:	2.4	13.02 [b]	Pasadena A.S. 4	13:58:	4.1	15.01 [a]	" " A.S. 1
12:15:	1.6	12.40 [b]	Pasadena A.S. 5	22:55:	3.8	14.54 [a]	" " A.S. 2
13:36:	1.8	12.09 [b]	Pasadena A.S. 6	23:52:	3.8	14.54 [a]	" " A.S. 3
14:46:	1.9	11.88 [b]	Pasadena A.S. 7	92/04/24	3.5	14.37 [a]	" " A.S. 4
88/12/04	2.0	12.24 [b]	Pasadena A.S. 8	18:06:	3.7	14.52 [a]	" " A.S. 5
88/12/08	2.2	12.64 [b]	Pasadena A.S. 9	18:20:	3.7	14.61 [a]	" " A.S. 6
89/01/19	5.0	16.51 [a]	Malibu	92/04/25	3.7	14.73 [a]	" " A.S. 7
89/02/18	4.3	15.34 [e]	Upland	18:56:	4.4	15.05 [a]	" " A.S. 8
89/08/08	5.3	16.41 [c]	Los Gatos	92/04/26	3.7	14.27 [a]	" " A.S. 9
89/10/18	7.0	19.48 [c]	Loma Prieta	6:26:	4.2	15.69 [a]	" " A.S. 10
90/02/28	3.7	14.65 [e]	Upland F.S.	17:21:	4.3	15.39 [a]	" " A.S. 11
90/02/28	5.2	17.40 [e]	Upland M.S.	92/04/27	4.2	15.41 [a]	" " A.S. 12
90/03/01	4.7	15.70 [e]	Upland A.S.	92/04/28	3.7	14.90 [a]	" " A.S. 13
90/03/02	4.6	15.60 [e]	Upland A.S.	11:33:	3.8	15.12 [a]	" " A.S. 14
90/04/17	4.6	15.78 [e]	Upland A.S.	92/04/30	3.7	14.70 [a]	" " A.S. 15

Table 1 (cont.): Earthquakes with Moments Determined Using Broadband Data

Date	M_L	$\log(M_0)$	Event	Date	M_L	$\log(M_0)$	Event
90/10/24	5.0	16.70 [g]	Lee Vining	92/05/01	3.8	14.71 [a]	J. T. A.S. 16
90/12/17	3.7	14.38 [a]	Big Bear I	92/05/02	4.1	14.64 [a]	" " A.S. 17
90/12/18	3.7	15.04 [a]	White Wolf Fault	19:10:	3.4	14.35 [a]	" " A.S. 18
91/05/20	3.7	14.48 [a]	San Jacinto I	92/05/04	4.0	15.04 [a]	" " A.S. 19
91/05/20	3.7	14.20 [a]	San Jacinto II	16:19:	4.8	16.19 [a]	" " A.S. 20
91/06/28	5.4	17.41 [f]	Sierra Madre	92/05/06	4.5	15.87 [a]	" " A.S. 21
15:37:	3.9	14.61 [f]	S. Madre A.S.	92/05/12	4.4	15.60 [a]	" " A.S. 22
17:00:	4.3	15.60 [f]	S. Madre A.S.	92/05/18	3.5	14.39 [a]	" " A.S. 23
91/06/29	4.0	14.60 [a]	Mojave	15:44:	4.9	16.10 [a]	" " A.S. 24
91/07/06	3.8	14.59 [f]	S. Madre A.S.	92/06/11	4.3	15.29 [a]	" " A.S. 25
91/10/12	4.0	15.04 [a]	Blue Cut	92/05/31	3.2	13.78 [a]	Lenwood Flat I
91/10/27	3.4	14.26 [a]	San Jacinto	92/05/31	3.5	14.28 [a]	Lenwood Flat II
91/12/03	5.4	16.72 [g]	San Miguel	92/06/28	3.7	14.29 [a]	Landers A.S.
91/12/04	4.2	14.95 [a]	Julian	92/06/29	5.4	16.85 [a]	Landers A.S.
91/12/04	4.0	14.62 [a]	Big Bear II	14:41:	4.4	16.90 [a]	Landers A.S.
92/02/17	3.5	14.66 [a]	Coso	16:01:	5.2	17.16 [a]	Landers A.S.
92/02/19	4.0	14.85 [a]	Coso I	92/06/29	5.6	17.40 [c]	Little Skull Mtn
92/02/19	3.7	14.41 [a]	Coso II	92/06/29	3.7	14.66 [a]	La Canada
92/02/21	3.7	15.30 [a]	Coso	92/06/30	4.7	15.83 [a]	Landers A.S.
92/02/22	3.9	14.28 [a]	Coso	21:49:	4.3	15.87 [a]	Landers A.S.

[a] Thio and Kanamori, 1992; [b] Ma and Kanamori, 1991; [c] Zhao and Helmberger, 1993;

[d], [e], [f], [g] Dreger and Helmberger, 1990, 1991a, 1991b, 1992;

Table 2: Explosions in this study

Date	M_L	$\log(M_0)$	Event	Date	M_L	$\log(M_0)$	Event
57/09/19	4.25	14.30 [a]	Rainier	70/03/19	4.05	13.65 [g]	Jal
61/12/03	3.91	13.86 [a]	Fisher	70/03/23	5.29	15.73 [g]	Shaper
62/06/27	4.63	14.55 [g]	Haymaker	70/03/26	6.17	17.72 [c]	Handley
65/02/16	4.21	13.98 [g]	Merlin	70/05/01	4.18	14.35 [h]	Beeblam
65/03/03	5.04	15.41 [g]	Wagtail	70/05/05	4.82	14.70 [g]	Mintleaf
65/04/14	4.23	14.02 [g]	Palanquin	70/05/15	5.00	15.19 [g]	Cornice
65/05/12	3.91	13.84 [g]	Buteo	70/05/21	3.60	13.23 [g]	Manzanas
66/04/25	4.69	14.90 [g]	Pinstripe	70/05/21	5.00	14.98 [g]	Morrones
66/04/14	5.02	15.39 [g]	Duryea	70/05/26	4.63	14.60 [g]	Hudsonmoon
66/05/05	4.04	14.24 [g]	Cyclamen	70/05/26	5.20	15.56 [g]	Flask
66/05/13	5.01	15.75 [g]	Piranha	71/06/19	4.20	13.83 [g]	Embudo
66/06/02	4.98	15.73 [g]	Piledriver	71/06/23	4.50	14.45 [g]	Laguna
66/06/25	4.33	14.13 [g]	Vulcan	71/06/29	4.90	14.64 [g]	Harebell
66/06/30	5.90	16.49 [g]	Halfbeak	71/10/29	4.10	14.03 [g]	Pedernal
66/12/20	6.07	16.98 [g]	Greeley	71/10/08	4.10	14.02 [g]	Cathay
67/02/08	4.09	13.82 [g]	Ward	72/04/19	4.20	13.73 [g]	Longchamps
67/02/23	3.89	13.81 [g]	Persimmon	72/05/19	4.48	14.66 [g]	Monero
67/04/07	3.97	13.76 [h]	Fawn	72/10/03	4.40	13.93 [g]	Delphinium
67/04/21	3.83	13.51 [h]	Effendi	73/06/06	5.68	16.78 [e]	Almendro
67/04/21	3.89	13.72 [h]	Chocolate	75/05/14	5.86	16.50 [e]	Tybo
67/05/23	5.57	16.46 [e]	Scotch	75/06/19	5.74	16.58 [e]	Mast
67/06/26	4.54	14.42 [g]	Midimist	75/06/26	5.95	16.96 [g]	Camembert

Table 2 (cont.): Explosions in this study							
Date	M_L	log(M_0)	Event	Date	M_L	log(M_0)	Event
67/08/31	4.73	14.46 [g]	Doormist	75/10/24	4.86	14.80 [g]	Huskypup
67/09/21	3.87	13.51 [g]	Marvel	75/10/28	6.08	17.03 [g]	Kasseri
67/09/27	5.66	16.32 [e]	Zaza	76/02/12	6.12	17.00 [g]	Fontina
68/01/19	5.74	16.83 [g]	Faultless	76/02/26	5.86	16.79 [e]	Cheshire
68/03/12	3.96	14.28 [g]	Buggy	76/03/09	5.83	16.79 [e]	Estuary
68/04/26	6.09	17.24 [g]	Boxcar	76/03/17	5.77	16.52 [e]	Pool
68/09/24	5.06	14.85 [g]	Hudsonseal	77/04/05	5.20	16.01 [e]	Marsilly
68/11/04	4.46	14.57 [g]	Crew	77/04/27	4.90	15.62 [g]	Bulkhead
68/12/19	6.14	17.35 [g]	Benham	77/05/25	5.00	15.52 [g]	Crewline
69/02/12	4.81	14.63 [g]	Cypress	77/11/09	5.40	16.27 [e]	Sandreef
69/05/07	5.68	16.42 [e]	Purse	77/12/14	5.30	16.22 [e]	Farallones
69/09/16	6.19	16.82 [b]	Jorum	78/03/23	5.30	16.02 [d]	Iceberg
69/10/08	5.50	16.19 [c]	Pipkin	78/04/11	5.10	15.89 [d]	Backbeach
69/10/29	4.40	13.55 [g]	Cruet	78/07/12	5.20	15.75 [g]	Lowball
69/10/29	4.60	13.97 [g]	Pod	78/08/31	5.30	15.92 [d]	Panir
69/10/29	5.50	15.79 [g]	Calabash	78/09/13	4.40	14.55 [g]	Diablohawk
70/02/11	4.67	14.77 [g]	Diamamist	78/09/27	5.30	16.15 [d]	Rummy
70/02/25	4.60	14.89 [g]	Cumarin	78/11/02	4.23	14.36 [h]	Emmenthal
70/02/26	4.80	14.65 [g]	Yannigan	78/11/18	5.00	15.30 [g]	Quargel
70/03/06	4.20	13.57 [g]	Cyathus	78/12/16	5.20	16.40 [c]	Farm
70/03/06	4.10	13.09 [g]	Arabis	79/02/08	5.20	15.80 [g]	Quinella
79/06/11	5.30	16.13 [d]	Pepato	84/03/31	4.20	13.71 [g]	Agrini

Table 2 (cont.): Explosions in this study

Date	M_L	$\log(M_0)$	Event	Date	M_L	$\log(M_0)$	Event
79/06/20	3.92	13.91 [h]	Chess	84/05/01	5.10	15.76 [g]	Mundo
79/09/06	5.30	16.16 [d]	Hearts	84/05/31	5.30	15.89 [g]	Caprock
79/09/26	5.20	15.98 [d]	Sheepshead	84/06/20	4.40	14.48 [g]	Duoro
79/11/29	3.89	13.66 [h]	Backgammon	84/07/25	5.30	15.42 [g]	Kappeli
80/03/08	3.89	13.43 [h]	Norbo	84/08/02	4.30	14.28 [g]	Correo
80/04/26	5.10	15.91 [c]	Colwick	84/08/30	4.50	14.52 [g]	Dolcetto
80/04/30	5.10	15.61 [g]	Pyramid	84/09/13	4.80	15.01 [g]	Breton
80/07/25	5.10	16.10 [d]	Tafi	84/11/10	4.30	14.21 [g]	Villita
80/10/31	4.50	14.77 [g]	Minersiron	84/12/09	5.10	15.63 [g]	Egmont
81/01/15	5.20	15.79 [g]	Baseball	84/12/15	5.00	15.63 [g]	Tierra
81/06/06	5.40	15.87 [f]	Harzer	85/03/15	4.60	14.77 [g]	Vaughn
81/11/12	5.00	15.61 [g]	Rousanne	85/03/23	5.00	15.31 [g]	Cottage
82/01/28	5.30	16.08 [g]	Jornada	85/04/02	5.40	16.12 [g]	Hermosa
82/02/12	5.00	15.95 [g]	Molbo	85/04/06	4.50	14.86 [g]	Misty-rain
82/02/12	5.00	15.90 [g]	Hosta	85/06/12	5.10	15.85 [g]	Salut
82/04/17	4.40	14.35 [g]	Tenaja	85/07/25	5.20	15.73 [g]	Serena
82/04/25	5.00	15.79 [g]	Gibne	85/12/05	5.20	15.56 [g]	Kinibito
82/05/07	5.20	15.76 [g]	Bouschet	85/12/28	5.00	15.57 [g]	Goldstone
82/06/24	5.20	15.96 [g]	Nebbiolo	86/03/22	5.10	15.46 [g]	Glencoe
82/07/29	4.10	14.45 [g]	Monterey	86/04/10	4.50	14.78 [g]	Mightyoak
82/08/05	5.40	16.16 [g]	Atrisco	86/04/22	5.00	15.71 [g]	Jefferson
82/09/02	3.50	13.23 [g]	Cerro	86/05/21	4.00	13.96 [g]	Panamint

Table 2 (cont.): Explosions in this study

Date	M_L	$\log(M_0)$	Event	Date	M_L	$\log(M_0)$	Event
82/09/23	4.60	14.82 [g]	Huronlanding	86/06/05	5.30	15.58 [g]	Tajo
82/09/23	4.60	14.88 [g]	Frisco	86/06/25	5.30	15.61 [g]	Darwin
82/09/29	3.80	13.98 [g]	Borrego	86/07/17	5.20	15.08 [g]	Cybar
82/11/12	4.10	13.92 [g]	Seyval	86/07/24	4.70	14.40 [g]	Cornucopia
82/12/10	4.40	14.56 [g]	Manteca	86/09/30	5.40	15.72 [g]	Labquark
83/03/26	4.90	15.44 [g]	Cabra	86/10/16	5.30	15.77 [g]	Belmont
83/04/14	5.20	15.59 [g]	Torquoise	87/04/18	5.30	15.77 [g]	Delamar
83/05/26	4.30	14.26 [g]	Fahada	87/04/30	5.30	15.88 [g]	Hardin
83/06/09	4.30	14.29 [g]	Danablu	87/06/18	4.00	13.90 [h]	Brie
83/09/01	5.30	15.77 [f]	Chancellor	87/10/23	5.40	15.31 [g]	Borate
83/09/22	4.00	13.90 [g]	Techado	88/04/07	3.60	12.75 [h]	Abliene
83/12/16	4.80	15.22 [g]	Romano	90/06/21	4.30	13.91 [h]	Austin
83/05/05	4.20	14.26 [g]	Crowdie	91/08/15	4.00	14.10 [h]	Floydada
84/02/15	4.50	14.78 [g]	Milagro	92/09/18	4.00	14.02 [h]	Hunterstrophy
84/03/01	5.30	15.85 [g]	Tortugas	92/09/23	4.41	14.27 [h]	Divider

[a] Aki *et al*, 1974; [b] Helmberger and Hadley, 1981; [c] Stump and Johnson, 1984;
[d] Given and Mellman, 1986; [e] Stevens, 1986a; [f] Johnson, 1988;
[g] Woods and Harkrider, 1993; [h] This study

SECTION 2

Source Retrieval from Broadband Regional Seismograms; Hindu Kush Region

Source Retrieval from Broadband Regional Seismograms; Hindu Kush Region

Lian-She Zhao and Donald V. Helmberger

Seismological Laboratory 252-21

California Institute of Technology

Pasadena, CA 91125, USA

ABSTRACT

A method of relocation and source characterization of small earthquakes using one modern regional station is developed and tested. First, we model teleseismic body-waves of two events, which are used as masters. Short period depth phases, pP and sP, are used to establish the epicentral depth, and the events are relocated using calibrated stations and a mantle model derived for this region, TIP. The events moved upward by 12 and 31 kms, respectively. The regional waveforms recorded at the IRIS station GAR from the best determined source are forward modeled to establish a local crustal model. A four-layered model with a thickness of 65 km proves effective. Synthetics from this crustal model can then be compared to the data from other events where the depths are poorly known, i. e., PDE depths of 33 km. Forward modeling of the short period phases allows better estimates of depth and makes relocation possible. Next, we perform a long period inversion of whole and partial waveform data to obtain source mechanism and moment, and repeat the procedure if necessary. This technique is applied to events in the tectonically active Pamir-Hindu Kush region to test its usefulness. Five crustal events sampling various azimuths are presented as examples of relocation and determination of source mechanisms from small events. The smallest

event has a moment of 5.1×10^{22} dyne-cm. For the seven events we studied, the average depth correction to PDE is 19 km, and the location correction is 11 km on average. The method can be used to identify earthquakes and thus it lowers the threshold below present m_b:M_S discrimination, since these events are too small to be seen teleseismically. Secondly, these events can be used as "masters" in the calibration of other systems, case-based event characterizations, etc.

Running title: Source Retrieval

INTRODUCTION

Earthquake source mechanisms remains an important topic in seismology. Techniques to obtain accurate seismic parameters from teleseismic waveform data have become well developed both for surface waves (Dziewonski et al., 1981) and for body waves (Langston and Helmberger, 1975). PDE gives the source mechanisms for events with magnitude greater than 5.5 routinely and mechanisms are published in bulletins and catalogs. However, smaller earthquakes in the magnitude range $4 < m_b < 5.5$ are often not well recorded teleseismically. The importance of source mechanisms of these smaller earthquakes is growing since they prove useful in tectonic studies, geodynamics, earthquake predictions, and verification of test ban treaties. However, source mechanism for these small events are difficult to determine, since they are poorly recorded. Usually, they appear on only a few stations, maybe only one at regional distances. In this paper, we address the issue of source estimates using one broadband station (GAR) situated in the remote region of Garm, CIS, see Figure 1.

GAR is one of the IRIS broadband digital stations which consist of the Widlandt-Streckeisen sensor and the Quanterra data logger. The systems remain stable for even the rather strong motions received from large regional events, see

Figure 2. This feature is essential to our procedure since we can study these records with the source characteristics determined by teleseismic means. Included in Figure 2 are the responses of conventional instruments. For example, the motions of the LP3090 are similar to the long-period WWSSN and would be off-scale at the normal gains of 1500. Source inversion studies using regional phases are usually conducted on the longer periods using the LP3090 as a filter (see Dreger and Helmberger 1991a, 1991b; Fan and Wallace 1991). The short period Wood-Anderson (WA.SP) seismograms usually are used in estimating the local magnitude, M_L, and prove useful in defining depth phases. A strategy for determining a crustal model that produces Green's function explaining regional recordings, such as in Figure 2, is given in a earlier paper, Zhao and Helmberger (1991a). We apply the same procedure in this paper where we forward model broadband regional waveforms of these master events to determine the velocity structure. We use this structure to predict the waveforms of the smaller events where we generally find disagreements with the observations in ranges and depth relative to those given in bulletins. Once the source depth and source receiver distance of a particular earthquake are adjusted to fit the Green's functions, we use the inversion code of Dreger and Helmberger (1991a, 1991b) to determine the source mechanism. The physical information that makes this method work is extracted from the relative P, SV, and SH strengths as pointed out by Langston (1982).

VELOCITY STRUCTURE BENEATH THE GARM REGION

In this section, we discuss the development of the model using the master events. We begin by first determining the source mechanisms of the two large events displayed in Figure 2 and their detailed source properties. Actually, Event 89205 will be used as the master event and Event 90036 will be used in a compatibility test. This allows an independent check on the regional results compared

with the teleseismic data, and provides some confidence in the procedure.

Locations and source mechanisms of the master events

In order to get more accurate information about these sources, we forward model the teleseismic waveforms of long- and short-period waveforms available from GDSN stations to determine the source depth and source mechanism. Then we assume the source depth to be fixed and use the relocation scheme of Zhao and Helmberger (1991b) to determine the location and origin time. The model used to calculate Green's functions is TIP (Tibet model, Zhao et al., 1991). For the relocation scheme, a TIP source region and Jeffreys-Bullen receiver regions are assumed. Dziewonski and Anderson's (1983) station corrections are used as in the above study.

Figures 3 gives the results of forward modeling the 89205 event. The event information is given in Table 1, according to the various agencies. In Figure 3a, adequate fits for the long-period waveforms are reached for all stations except WMQ. WMQ is at the distance is 14.9°, within the upper mantle triplication, and the poor fit means that TIP model does not work well for this path. TIP works well for the paths crossing the Tibetan Plateau (see the fits of KMI and LZH data, Figure 3a). The short-period synthetics (Figure 3b) indicate the triplications where the additional arrivals are associated with pP and sP. These depth phases are seen in the teleseismic stations ANTO, COL, CTAO, HIA, MDJ, SSE and TOL. Our forward modeling results indicate the source depth is 85 km (PDE 97 km); source mechanism: strike 245°, dip 45° and rake 140°, with a moment of 1.0×10^{25} dyne-cm. The location is 36.131°N, 71.073°E , and the origin time is 3:27:48.9. These results can be compared with the other estimates in Table 1.

Forward modeling of the source mechanism of the 90036 event is given in Figure 4. The long-period fits are not as good as those for the event 89205 (Fig-

ure 3a). However, good fits are obtained for stations CTAO, GRFO, KMI, MAJO, and WMQ (Figure 4a). The fits are also acceptable for stations ANTO, BCAO, HIA, NWAO, and SLR, if we disregard the amplitude ratio of P and pP waves. There are also three arrivals on the synthetics (except the stations WMQ and LZH, Figure 4b). Good separations of the three arrivals are obtained for stations ARU, BJI, CTAO, KMI, LZH, MAJO, SLR and TOL, and as well as the spacing of the six arrivals at stations LZH and WMQ which fixes the source depth. Results from forward modeling of the 90036 event indicate a source depth of 100 km (PDE 131 km), source mechanism: strike 115°, dip 52° and rake 126°; with a moment of 1.5×10^{25} dyne-cm. The relocation yields the coordinates 37.012°N, 71.240°E, and the new origin time 5:16:44.5. These results can be compared with the parameters given by different agencies in Table 1. The relocated events agree well with the ISC estimates in depth and origin times but differ considerably from HRVD results.

Velocity structure of Garm region

Since the master event occurred at source depths not usually modeled, we will begin with some preliminary results for a simple layer over a half-space model, see Figure 5. The responses of the three fundamental fault orientations are displayed to gain insight into possible solutions. The SH system is relatively simple and has been neglected. The upper panel shows the first few sets of ray paths used in the construction of the synthetic response along with an approximate solution including only eight rays, the direct with conversions at the Moho and internal reflections without conversion at the Moho. With only eight rays to consider, it proves relatively easy to investigate models that might match the 89205 observations. Figure 6 displays the best fitting one-layer and four layered models found by the trial-and-error method. This region has a crust of about 65 km thick, and

a mantle with compressional velocity of about 8.0 km/sec and a shear velocity of about 4.60 km/sec, Table 2. These models are nearly the same as TIP (Zhao et al., 1991) and thus TIP can be used in relocating events in this region.

Synthetics for these models are given in Figure 7. Despite the complexity of the waveforms, good fits are obtained for the major arrivals of P, S_P, PP_mP, SS_mS and S phases. After the S arrival the waveform becomes difficult to explain in terms of a flat-layered model and will be neglected. Note that the arrivals SP_mP and SP_oP (we use "o" here after to denote internal crustal reflections) are arriving at almost the same time on the data, but not in the synthetics. We could find a one layer model to meet the requirement of all the internal and Moho reflections arriving at about the same time, but the synthetic fit of the latter part of the record is not as good as that of the four layer model. This suggests a two dimensional property along the path.

We invert the whole waveform and obtain strike 272°, dip 44° and rake 136°, a mechanism quite close to that of teleseismic modeling. Figure 8 gives the comparison of long-period WWSSN data and synthetics of the two source mechanisms. We can see that these two mechanisms work equally well in matching the data. If we do not know the source mechanism, we have no reason to choose one over the other. The moment obtained from the inversion is 6.4×10^{24} dyne-cm, slightly smaller than the teleseismic result.

Relocation by forward modeling

Most of the smaller events are not well constrained in depth, as indicated by the standard PDE default of 33 km. But from the experience gained in relocating events beneath Tibet, Zhao and Helmberger (1991b), we expect the location to be quite good in comparison. Essentially, the depth trades off with origin time. This means that we must explore the depth and to a lesser extent the range to

GAR before attempting an inversion. Thus we compare a catalog of Green's functions with the observed waveforms to make these adjustments (Figure 9).

Since we do not know the mechanism, we can begin by exploring with the three fundamental faults as displayed in Figure 10. The three dark traces are the three component data from the 90064 event and the eight lighter traces are the reflectivity synthetics for the fundamental faults (three traces for the vertical, three for the radial and two for the tangential). Since any fault can be approximated by a linear combination of these, it is likely that one of these traces will look like the data. For example, the synthetics associated with the 45° dip-slip fit the vertical and radial components of data quite well. For the tangential component the synthetics of strike-slip fault seem better, which is expected for a thrust mechanism. We compare the three component waveform data with the field of synthetics, by assuming the source mechanism as displayed in Figure 11, and reach a distance and a source depth that produces the best fitting synthetics. The distance of 320 km and the depth of 10 km, "320/10", are obtained (Table 1). Major phases are lined up with respect to P_n , the depth phase sP_mP, S_n, and surface waves. Next, we address the regional inversion results for this event in conjunction with results obtained from teleseismic studies since this is a relatively large event.

Event 90064

Two solutions for this event are available, namely, strike 169°, dip 30°, rake −57°, and moment 2×10^{25} dyne-cm from NEIC; and strike 192°, dip 36°, rake −46°, and moment 2×10^{25} dyne-cm given by Harvard, see Table 3. The source depth is 3 - 60 km from different agencies (see ISC bulletin for details).

Figure 12 gives the comparison of data with the synthetics predicted by the different source mechanisms. The top darker traces are the data. The second

traces are the synthetics of the source mechanism, strike 85°, dip 77°, rake 4°, and the moment of 8.8×10^{24} dyne-cm from the whole waveform inversion, and the third trace uses only a portion of the waveforms denoted by arrows. The bottom traces are the synthetics of the source mechanism of Harvard CMT solutions, strike 192°, dip 36°, rake − 46°.

Inversion results from the third trace are very close to the CMT solution and are almost the same as the mechanism given by NEIC. This solution and the CMT solution give very nice surface wave fits to the data (the third and the bottom traces, Figure 12). However, the partial waveform solution predicts the wrong polarity of both P_n and S_n (SH component) phases, and Harvard CMT gives a nodal P_n. The whole waveform solution is almost a pure strike-slip, however the partial waveform solution is the summation of pure strike-slip, dip-slip and 45° with about same strength for the $P-SV$ waves. The source mechanisms from inversion and others are given in Table 3, along with magnitude information. Thus, from Figure 12, it is clear that the source mechanism that predicts the best fit to the whole waveforms of one station may not be the same as the source mechanism from more stations and points out the limitation of the one-station waveform inversion. We will address these issues later.

The moment obtained form inversions, 8.8×10^{24} from the whole waveform data and 1.1×10^{25} from partial waveform data, are about half of that given by NEIC and Harvard. The differences may be caused by the depth uncertainty. Note that the amplitude of the surface waves is about the same as that of the S waves in the radial component, which suggests a deeper source, but this is not supported by the vertical component of the data. If the depth is 10 km deeper, one can expect a 50 percent increase of the moment (Figure 9). This suggests that the moment is an uncertain quantity for crustal events, if the depth can not be established. Next we return to the other master event, namely the deep

event 90036.

Event 90036

We start with some synthetics generated with rays containing direct and first crustal reflections for different depths and distances to relocate the event. The best estimates are given in Figure 13 along with the data. Although the synthetics of 245/100 (distance 245 and depth 100 km) seems better, those of the other two are also acceptable. The depth of 100 km agrees with the teleseismic, for the vertical travel time of the model given in Table 2 is almost identical to the model TIP used in the source depth determination. The distance of 245 km is slightly different from that of teleseismic results, namely 235 km and that of PDE 230 km. However, the origin time of the relocation is 1.7 seconds earlier than that of teleseismic result (Table 1). These differences can be easily accommodated by an increase in mantle velocity beneath 85 kms.

The inversion results for the source mechanism for the event 90036 are given in the lower portion of Figure 13. The source mechanism is: strike 227°, dip 47° and rake 46° from the whole waveform inversion. It is not much different from that of the teleseismic result: strike 245°, dip 50° and rake 53°. The inversion results are displayed as the second traces while the results assuming the teleseismic mechanisms are displayed in the third row. The mechanisms are quite similar as displayed but there are serious problems with the tangential motions. The observed tangential motions for the master event were nodal and also disturbed in that there appears to be (P - SV) motions observed on the tangential component. No clear explanation can be given for this except to point out that the strength of direct S is greatly reduced by the transmission across the mantle-crust boundary at these angles, that is, most of the energy is reflected down into the Earth. Apparently, the non-planar structure becomes particularly important in

this geometry. At any rate the lack of *SH* control greatly reduces the effectiveness of the method. Note that the later part of the synthetics is about the same for the two source orientations, whereas the teleseismic solution produces a slightly smaller P - wave in agreement with the data.

The moment from the inversion, 2.8×10^{25} dyne-cm, almost two times of that of teleseismic studies, 1.5×10^{25}, is the same as that given by NEIC and Harvard (Table 3). The amplitude predictions of the teleseismic mechanism are smaller than that of the data. The moment would be 1.8×10^{25}, instead of 1.5×10^{25}, in order for the teleseismic source mechanism to predict the correct amplitudes of this regional data. Since the tangential component is poorly matched, we did not include it in the moment calculation.

MORE EXAMPLES

Next, we present more examples of relocation and determination of source mechanisms for small crustal events, 89124, 89146, 90085, and 91026. Table 1 gives the relocation results and Table 3 gives the source mechanisms.

Event 89124

The forward relocation results are given in Figure 14, in which the event moved from PDE 208/33 to 200/20 . Synthetics at small perturbations in depth and distance are included. The data and the synthetics are lined up with respect to the first arrival $P_o P$. If we use the depth of 25 km (top traces), the $sP_m P$ arrival is later than in the data. The distance of 210 km predicts a separation of the $P_o P$ and $S_o S$ phases that is larger than in the data. The surface wave part of the data is very complicated on the vertical, while relatively simple on the radial component. The *SH* component has a small arrival before the arrival denoted as $S_o S$. This arrival could be a internal reflection in the crust, and suggests that this

particular path has a boundary in the upper 20 km of the crust. This is the indication of the complexity of the structure.

The inversion results are given in the lower portion of Figure 14, where the strike 33°, dip 21° and rake 10° is obtained. The moment is 3.8×10^{23} dyne-cm. The Rayleigh waves are excluded in this inversion because of the complex vertical component.

Event 89146

From forward modeling, we obtain 445/35 as the best location, which is close to 439/26, the estimate given by PDE. Figure 15 gives the synthetic comparison of the data with different source depths and distances. The data and synthetics are lined up with respect to the P_n arrival on the vertical and radial components, and S_n on the tangential. For the vertical and radial components, the 445/35 synthetics fit better than others. However, for the tangential component, the 445/30 synthetics are better (better timing of $S_m SS_m S$). The synthetics of the surface waves are acceptable. The strong $S_m SS_m S$ phase on the radial component suggests a relatively sharp Moho. The best source mechanism obtained from waveform inversion is: strike 128°, dip 89° and rake −1° and the moment is 1.4×10^{23} dyne-cm. This is essentially a strike-slip event. In the lower portion of Figure 15 gives the synthetic comparison of the data for both long-period and broadband. In this waveform inversion, we used the 445/35 synthetics for the vertical and radial components of Green's function and the 445/30 synthetics for the tangential component. The source mechanism from partial waveform (after S_n arrival) inversion is the same as the results given above.

Event 90085

The relocation results are given in Figure 16 where we obtain (315/10)

compared to the PDE (341/33). Note that a deeper source predicts a late sP_mP phase (top traces), larger distance gives a late arriving Airy phase (bottom traces). The data and synthetics are lined up with respect to P_n phase as in other plots. Note that many sharp arrivals on the synthetics are the result of the sharp boundaries in the crust of the model. The fundamental faults used in this figure are 45° dip-slip for the vertical and radial components and strike-slip for tangential component.

The source mechanism is: strike 320°, dip 24°, rake $-81°$ and the moment 5.1×10^{22} dyne-cm, from whole waveform inversion, see Figure 16. This source mechanism is very similar to the partial waveform result of Event 90064. However, a clear downward polarity of P_n shows up in the data. This event is small, and high-level long-period noise can be seen on both radial and tangential component. The source mechanism from partial waveform (after S_n arrival) inversion is: strike 316°, dip 24° and rake $-83°$. It is almost the same as the whole waveform inversion.

Event 91026

The relocation results for this event are given in Figure 17, where we obtain 225/10 compared with the PDE 225/32 estimate. Four major arrivals are indicated on the figure. They are: P_oP, a internal crustal reflection, P_mP, a reflection from Moho, and corresponding critical angle reflections of S waves. The data and synthetics are lined up with respect to the first arrival. Slight shifts in distance and depth indicates that the 225/10 is the best model as indicated in the upper portion of Figure 17.

We obtain two different source mechanisms, namely, strike 157°, dip 83°, rake 95°, and moment 7.2×10^{23} dyne-cm from whole waveform inversion; and strike 176°, dip 16, rake 288°, and moment 4.5×10^{23} dyne-cm, from a partial

waveform inversion. Although the values of dip and rake of the source mechanisms are very different, the radiation patterns of them are not much different for this particular station. The synthetic comparison of the two source mechanisms are given in the lower portion of Figure 17. Amazing fits of surface waveforms are reached from the partial waveform source mechanism, which predicts the wrong polarity for the early portion of the data (bottom traces). The whole waveform solution gives a good fit for the early portion of the data, but its surface wave is not as good as that of the partial waveform solution. Comparing the waveforms of the data and synthetics of the two source mechanisms, we conclude that the 91026 event has a nearly dip-slip source from the vertical and radial components. However, a strike-slip source predicts a better fit to the tangential component.

DISCUSSIONS

Our results are preliminary in nature in that we do not have much experience in broadband modeling, given the limited amount of recording history. Nevertheless, it appears that modeling regional data is easier than generally envisioned. In fact, some of our fits look quite promising. In this section we will discuss some of the questions of uniqueness and possible improvements in our present method.

The inversion scheme employed in the above examples is not particularly sophisticated. For instance, instead of applying a method that depends on the starting model we could have employed the moment tensor approach, see Fan and Wallace (1991). There is also, the measure of fit question, L1 versus L2, etc. But since we are dealing with very approximate Green's functions, we must be concerned with the actual fits of synthetics to observations, and a number of parameters involved. Sometimes the surface waves match very well but S_n has opposite polarity. Since the phase of the surface waves can be distorted easily by shallow

structure, we may want to choose a model that fits the S_n polarity even though that model does not produce the best inversion criterion. Thus the question of selective weighting appears where body waves are given preference. But, perhaps, P_n or S_n is nodal, and this waveform may not be so meaningful, and, perhaps, the Love wave should be emphasized. We can address these issues to some extent by conducting numerical experiments in which we examine the complete source model space for small changes in the Green's functions. To address these issues of uniqueness, we choose the event 90064 as a test case since it has a CMT solution available for comparison. This event is, also, interesting in that the P-waves are nodal which causes difficulties with the inversion, as discussed earlier. The inversion scheme minimizes the error defined by

$$e_i = \int_0^T [\, f_i(t) - g_i(t)]^2 dt,$$

where f_i, g_i are data and synthetics, T is the time segment used in the inversion. Note that this measure of fit tends to emphasize the longer periods and the largest amplitudes. In Figures 18 and 19, we explore the possible solutions by constructing three cross-sections through the 3D source space in terms of strike:rake, dip:rake, and strike:dip. Synthetics corresponding to the best fitting models are displayed in Figure 19. The top panel, Figure 18, displays the parameter space sampled at five degree intervals, with a moment of 10×10^{24} dyne-cm, and contours in dB units with a strike of 350°, a dip of 85° and a rake of 180° yielding the lowest error. The synthetics for this strike-slip orientations are displayed along the traces second from the bottom in Figure 19. The other solutions discussed earlier are included for comparison. The normalized cross-correlation coefficients are given to indicate the goodness of fit. Note that e_i depends on the amplitudes as well so that large cross-correlation coefficients do not completely control the

solution with respect to the inversion. The second panel in Figure 18 displays the parameter space generated with a smaller moment, $M_0 = 5 \times 10^{24}$. The corresponding synthetics are given at the bottom of Figure 19 with similar results to the top panel; dropping the moment tends to reduce the error somewhat. The third panel from the top of Figure 18 (325/10) displays even smaller $\sum e_i$ when the range is changed by 5 kms. The rake changes substantially and the overall fits are improved both in cross-correlation coefficients and reduced overall errors, see the top set of traces in Figure 19. The bottom panel displayed in Figure 18 gives the results for a 5 km change in depth. This set of Green's functions allows the best overall fit as indicated by the smallest error and greatest coefficients, see the second set of traces in Figure 19.

So far we have not used the broadband features of these seismograms but have concentrated on the longer period motions. Including shorter periods or actually modeling both short period and long period simultaneously is quite difficult. Recent studies of TERRAscope data suggests that the relative timing between phases, i. e., $P_m P$, $S_m S$ etc, while not so noticeable at long periods, becomes obvious in short period seismograms. Furthermore, lateral variation in structure causes surface reflected depth phases to show considerable scatter which can be accounted for some degree by applying decomposed Green's functions in which timing shifts between phases are allowed and determined by local calibration events (see Helmberger et al., 1992).

A less sophisticated approximation that still uses the energy ratios of short period, Wood-Anderson, over long period, Press-Ewing, band pass of the data. This ratio distinguishes earthquakes from explosions as pointed out recently by Woods et al. (1992). The ratio appears to be relatively independent of distance and depth if we eliminate the surface waves. Adding the surface waves or whole

record ratios show a dependence on depth and distance (Figure 20). These features can be seen in the Green's functions, Figure 9.

Figure 20, also, displays the obvious dependence of this energy ratio on source duration or stress-drop. Thus, we can obtain a rather rough estimate of stress level by adjusting the δt_i, assuming a triangle source history, to match the observed ratio. The numbers indicating the data ratios are on the right in Figure 19. The first number for the body wave portions of the observed and synthetics agrees roughly, assuming the same $\delta t = 1.2$ seconds for all cases, while the second number, for the whole seismograms, is effected by the depth and mechanisms. Note that a more strike-slip type of mechanism reduces the the long-period surface waves and increases the ratio, bottom traces. A deeper source, case 320/15, accomplishs the same effect. Thus, including such constraints can help establish the source depth and add creditability. However, there are complications which need to be understood and individual station characteristics established before these energy ratios can be treated seriously. For example, a station setting on soft material will probably observe anomalously strong short-periods. Secondly, directivity could, also, effect these energy ratios. These issues can probably be assessed with an adequate recording history and local experiences.

Other criterion can also be used to establish the nature of events such as the relationship of the derived mechanisms to the tectonics of the region. However, in this particular stressed zone with its relatively complex geology, see Chatelain et al. (1980), we probably want to use the derived mechanisms to study the tectonics as opposed to deducing mechanisms from the knowledge of particular fault dynamics.

We conclude from this discussion that the best way to obtain better results is to obtain more accurate Green's functions. This may be possible by

regionalization and using Green's functions based on azimuth. For example, in the Pamir region (latitudes of 34 – 38°N and longitudes 68 – 72°E), see Figure 1, Roecker (1982) inverted arrival times form 580 local events and fixed the crustal thickness at 70 km. He obtained an average crustal velocity model similar to ours. He suggested compressional and shear velocities of 8.08 and 4.63 km/sec for the depths of 70-110 km. These results are in good agreement with the model presented in Table 2 as well as the studies to the south by Zhao and Xie (1992) and Holt and Wallace (1990). The latter two studies suggest considerable lateral variations as originally proposed by Roecker (1982). This feature is well observed in a deep seismic sounding profile running from (42°N, 72°E) to (34°N, 75°E), Beloussov et al. (1980) and Kaila (1981), where the crustal thickness changes from 50-55 km at the northern end to 60-65 km at the south end. This means that the one dimensional velocity model assumed in our analysis is a rough approximation and allowing some regionalization could be quite helpful.

CONCLUSIONS

In conclusion, we have examined the possibility of providing source location and characterization using a single modern station. We selected the Hindu-Kush region in this pilot study largely because of it high seismic activity, numerous observations with only a short recording history. Unfortunately, a high rate of seismic activity, especially the dip-slip style in this region, is associated with complex crustal structure and wave propagation. Nevertheless, we found excellent waveform fits for some small events that can not be studied teleseismically. But considerable liberty was taken in moving the sources around to find a Green's function that worked. Such adjustment shift the timing and phases strengths of the various wave packets. Shifts of this sort could be caused by lateral variations

in structure and maybe not correspond to the true source position. However, since the applied shifts in this study produced solutions comparable to the teleseismic solutions for the large events, we think the results should also apply to the smaller events. To confirm this conclusion requires more information, perhaps, some short period regional data (networks) or preferably more IRIS stations.

ACKNOWLEDGMENTS

We would like to thank Doug Dreger for his suggestions and the use of his Inversion Code, Chandan Saikia for his FK code, and Holly Given for providing the data used in this study. This research was supported by the Advanced Research Projects Agency of the Department of Defense and was monitored by the Air Force Geophysics Laboratory under the contract F29601-91-K-DB14 and was also supported by Phillips Laboratory of the Air Force Materiel Command under contract F19628-90-K-0049. Contribution No. 5201, Division of Geological and Planetary Sciences, California Institute of Technology, Pasadena, California.

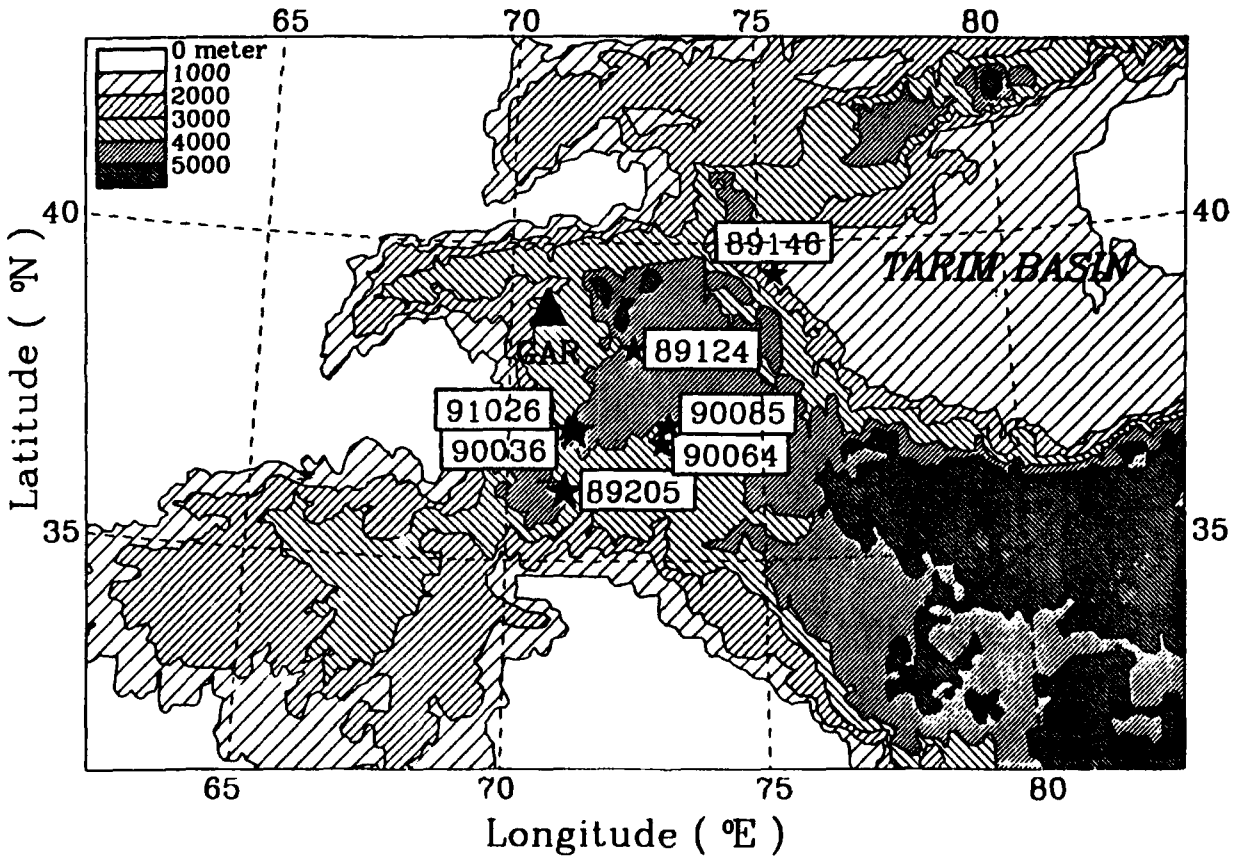
0 meter
1000
2000
3000
4000
5000
65
70
75
80
40
35
89146
TARIM BASIN
CAR
89124
91026
90085
90036
90064
89205
Latitude (°N)
Longitude (°E)

Figure 1

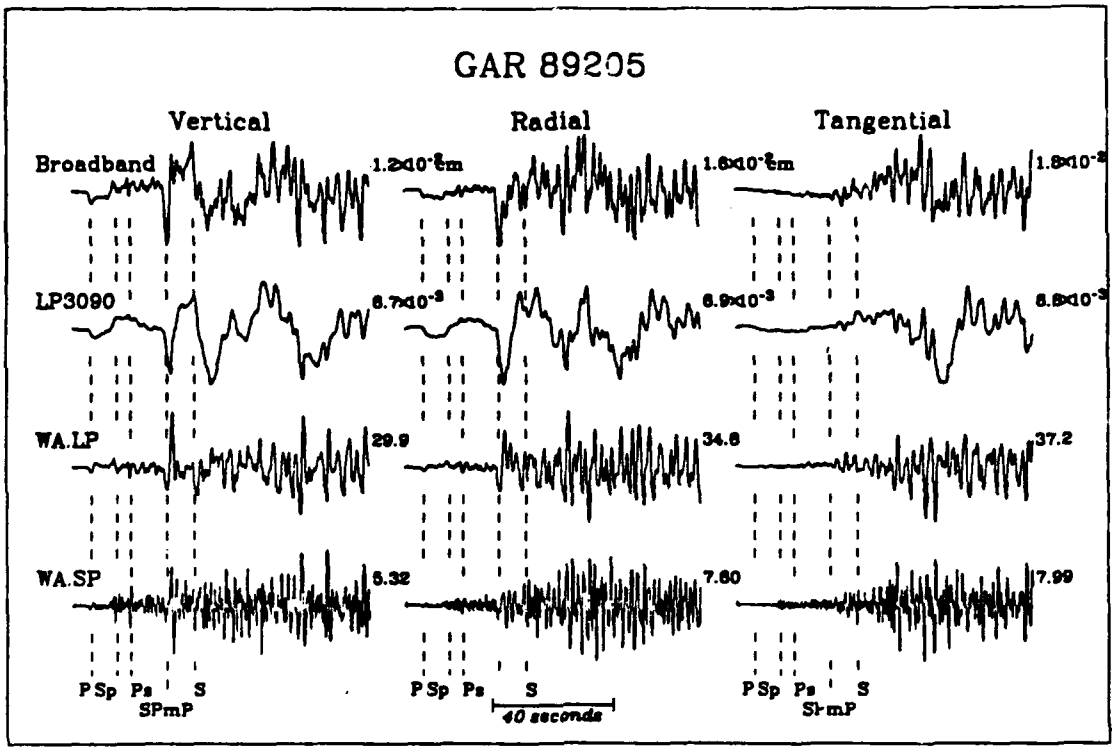

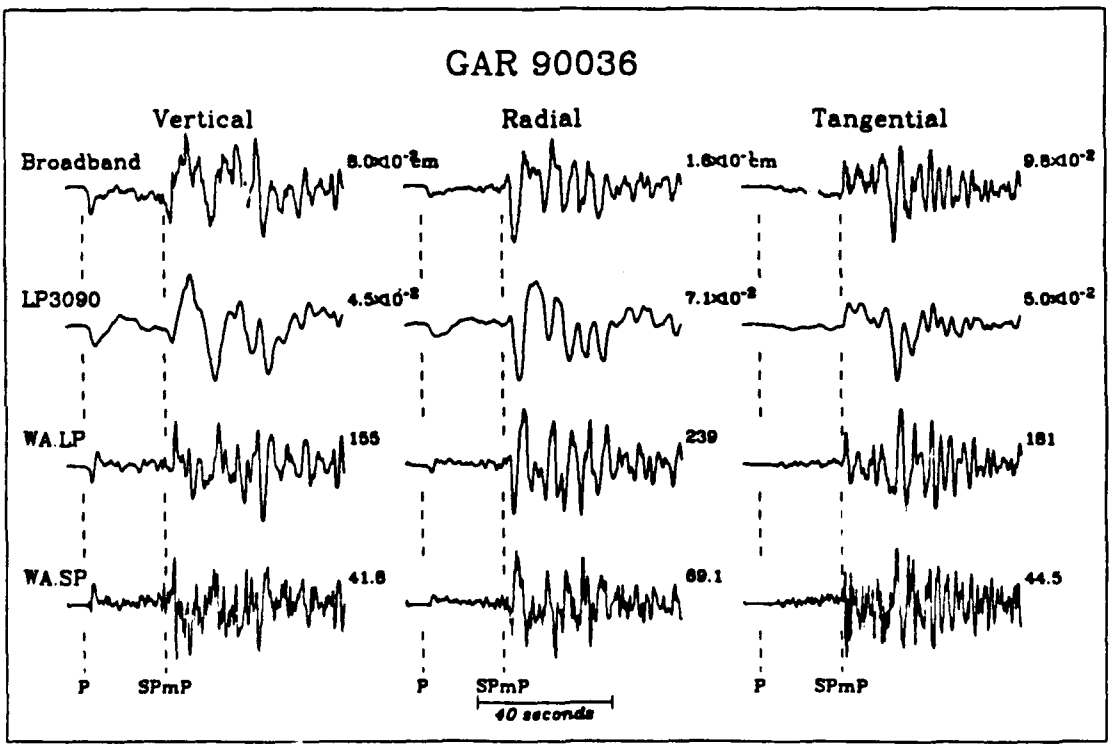

Figure 2

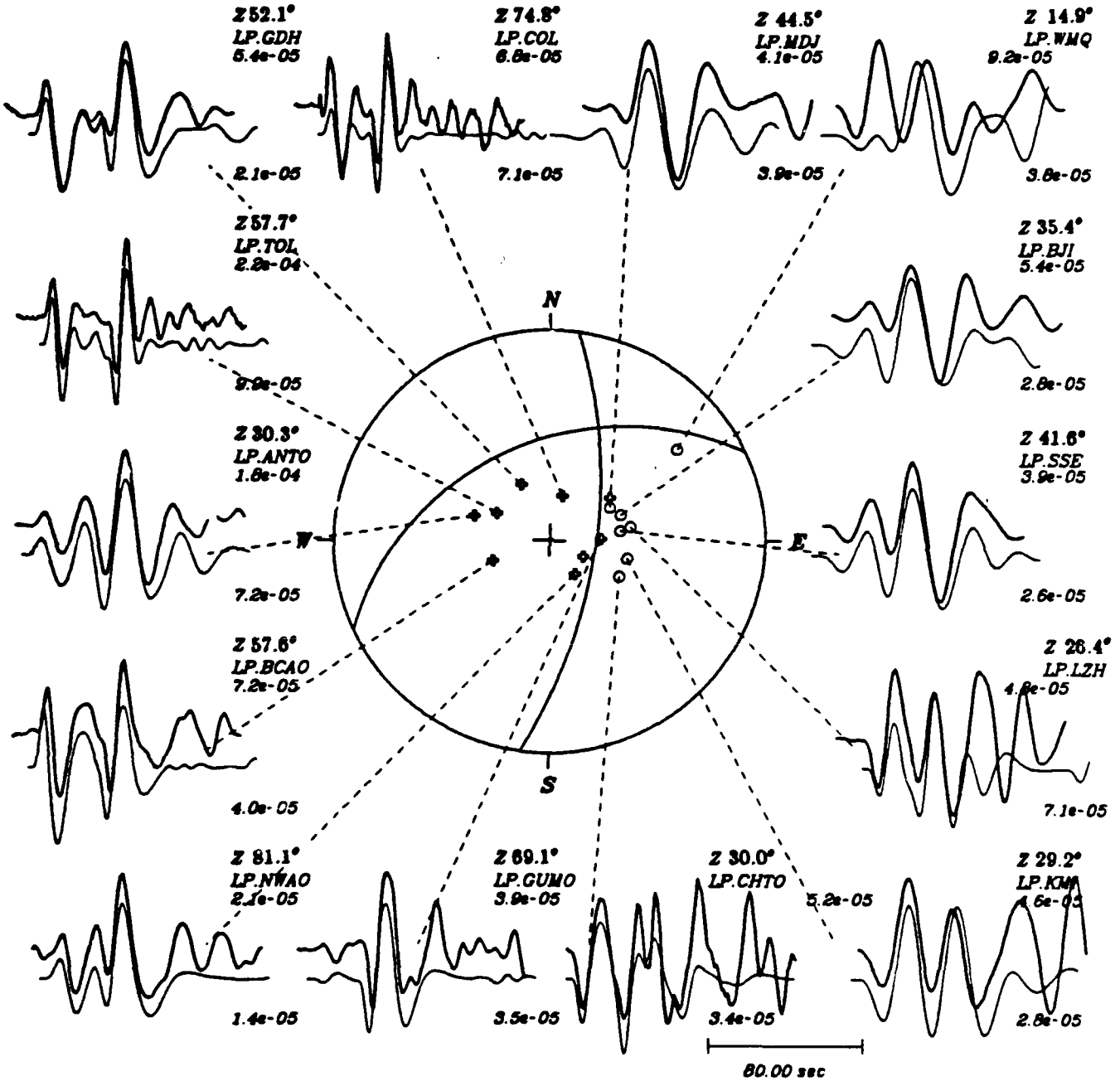

Figure 3a

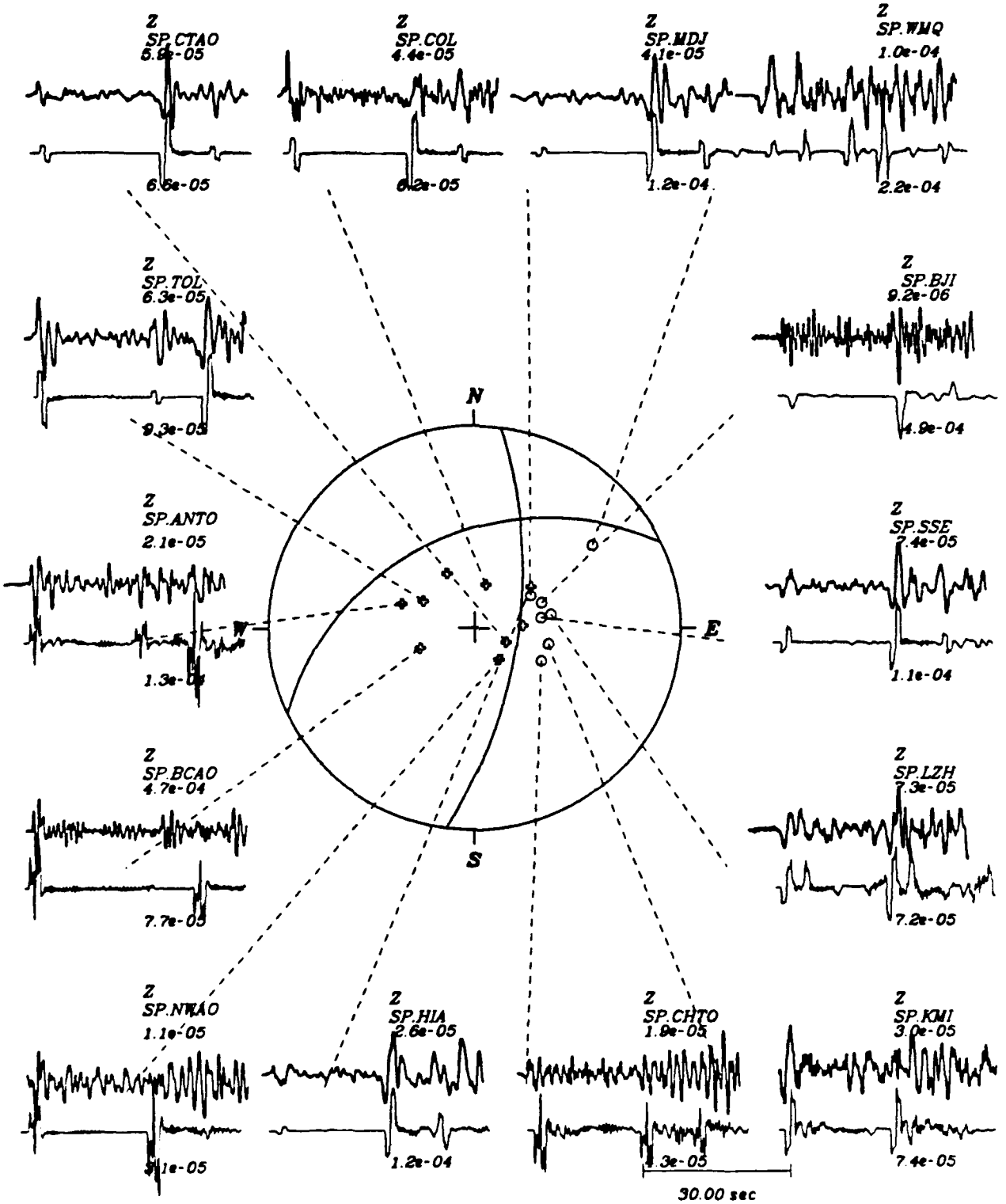
JUL 24,1989 3:27:48.77 36.114N 71.100E 85.0KM Strike 245 Dip 40 Rake 140 Moment 1.0e+25 Source fn 1.0,0.0,1.0
Z SP.CTAO 6.8e-05 6.6e-05
Z SP.COL 4.4e-05 6.2e-05
Z SP.MDJ 4.1e-05 1.2e-04
Z SP.WMQ 1.0e-04 2.2e-04
Z SP.TOL 6.3e-05 9.3e-05
Z SP.BJI 9.2e-06 4.9e-04
N
W
E
S
Z SP.ANTO 2.1e-05 1.3e-04
Z SP.SSE 7.4e-05 1.1e-04
Z SP.BCAO 4.7e-04 7.7e-05
Z SP.LZH 7.3e-05 7.2e-05
Z SP.NWAO 1.1e-05 5.1e-05
Z SP.HIA 2.6e-05 1.2e-04
Z SP.CHTO 1.9e-05 1.3e-05
Z SP.KMI 3.0e-05 7.4e-05
30.00 sec

Figure 3b

1.5 Final result

Feb 5,1990 5:16:45.10 37.069N 71.273E 102.0KM Strike 115 Dip 52 Rake 126 Moment 1.0e+25 Source fn 1.0,0.0,1.0

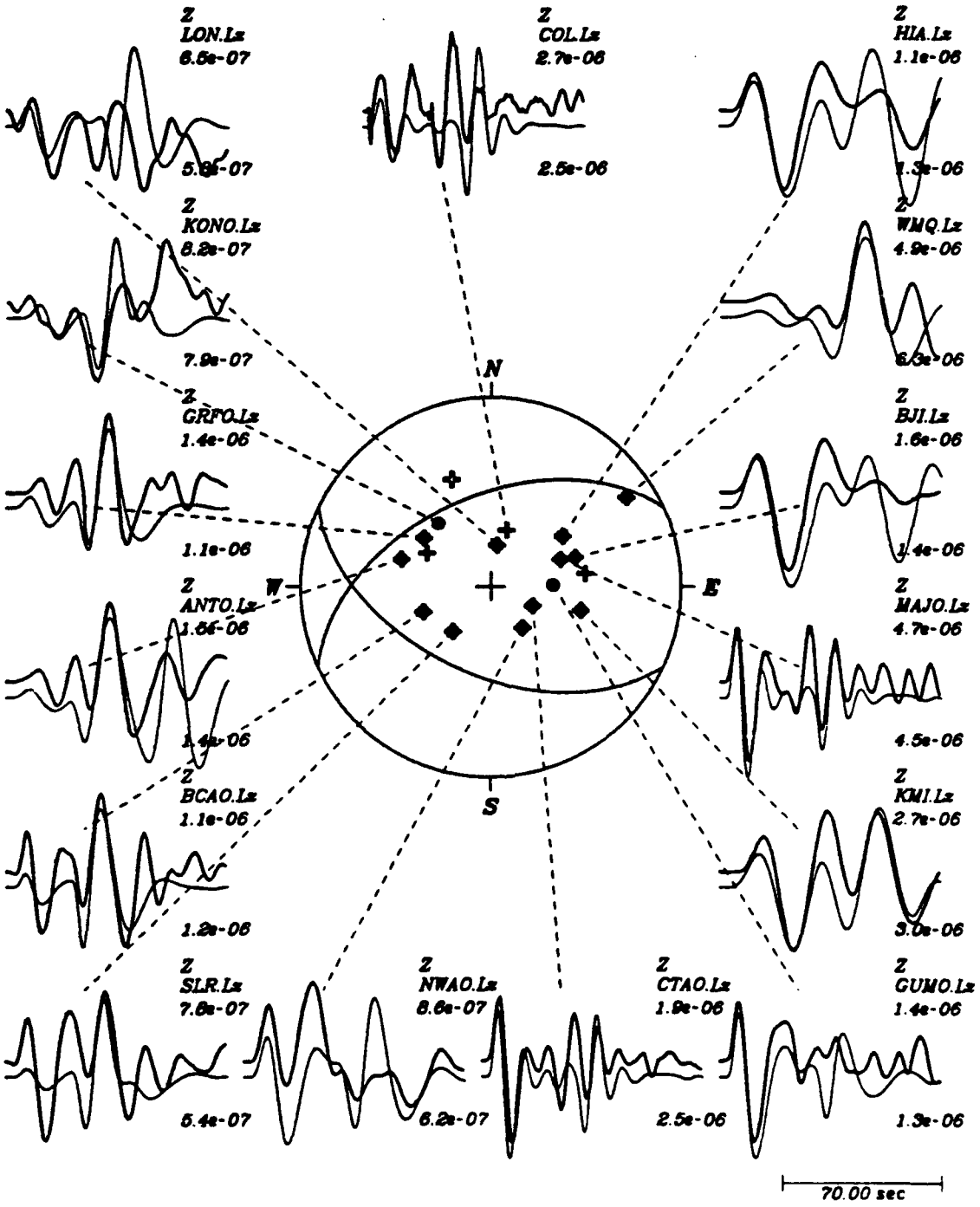

Figure 4a

Final seismo 0.5 0.5

Feb 5,1990 5:16:45.10 37.069N 71.273E 102.0KM Strike 115 Dip 52 Rake 126 Moment 1.5e+25 Source fn 1.0,0.0,1.0

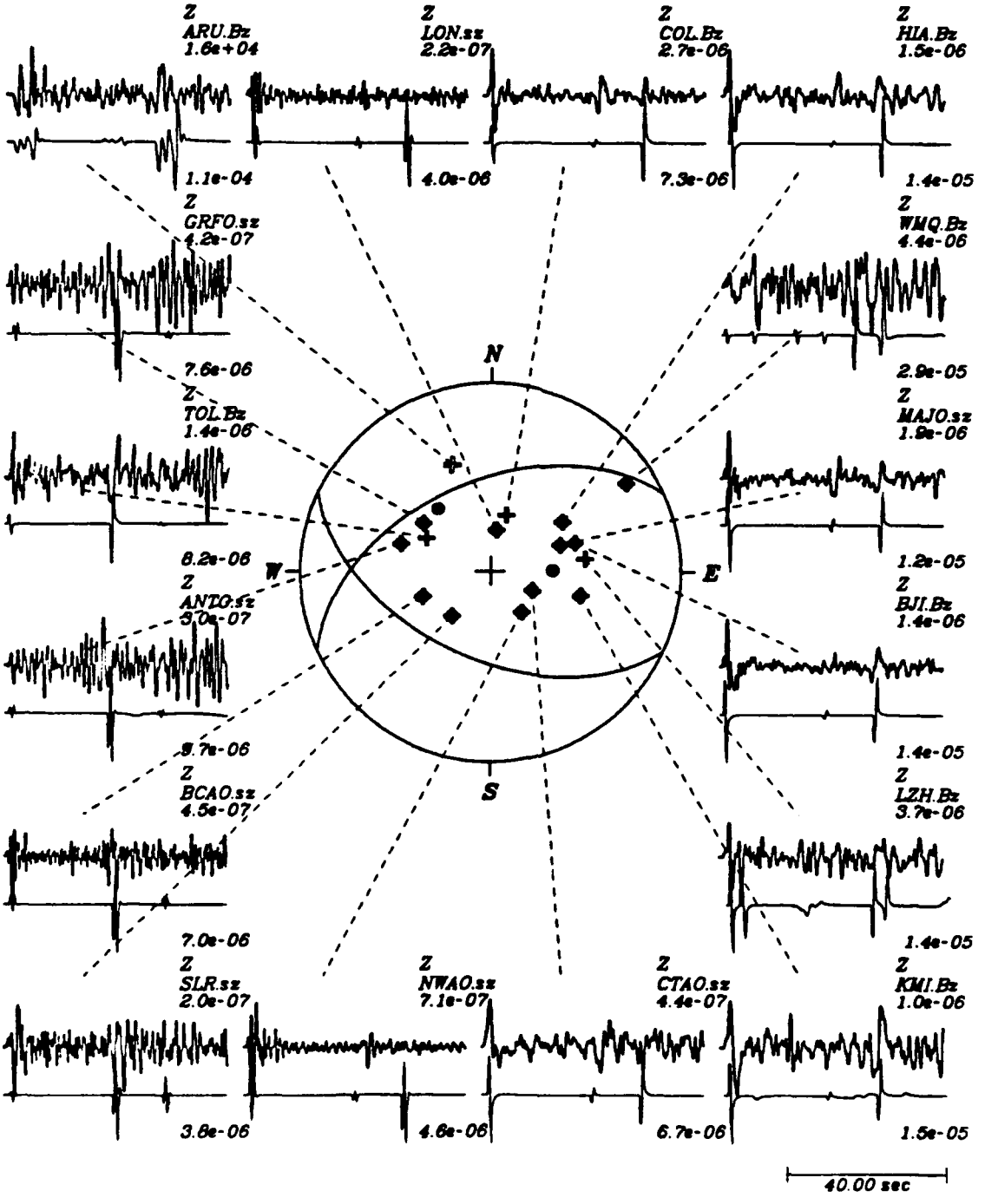

Figure 4b

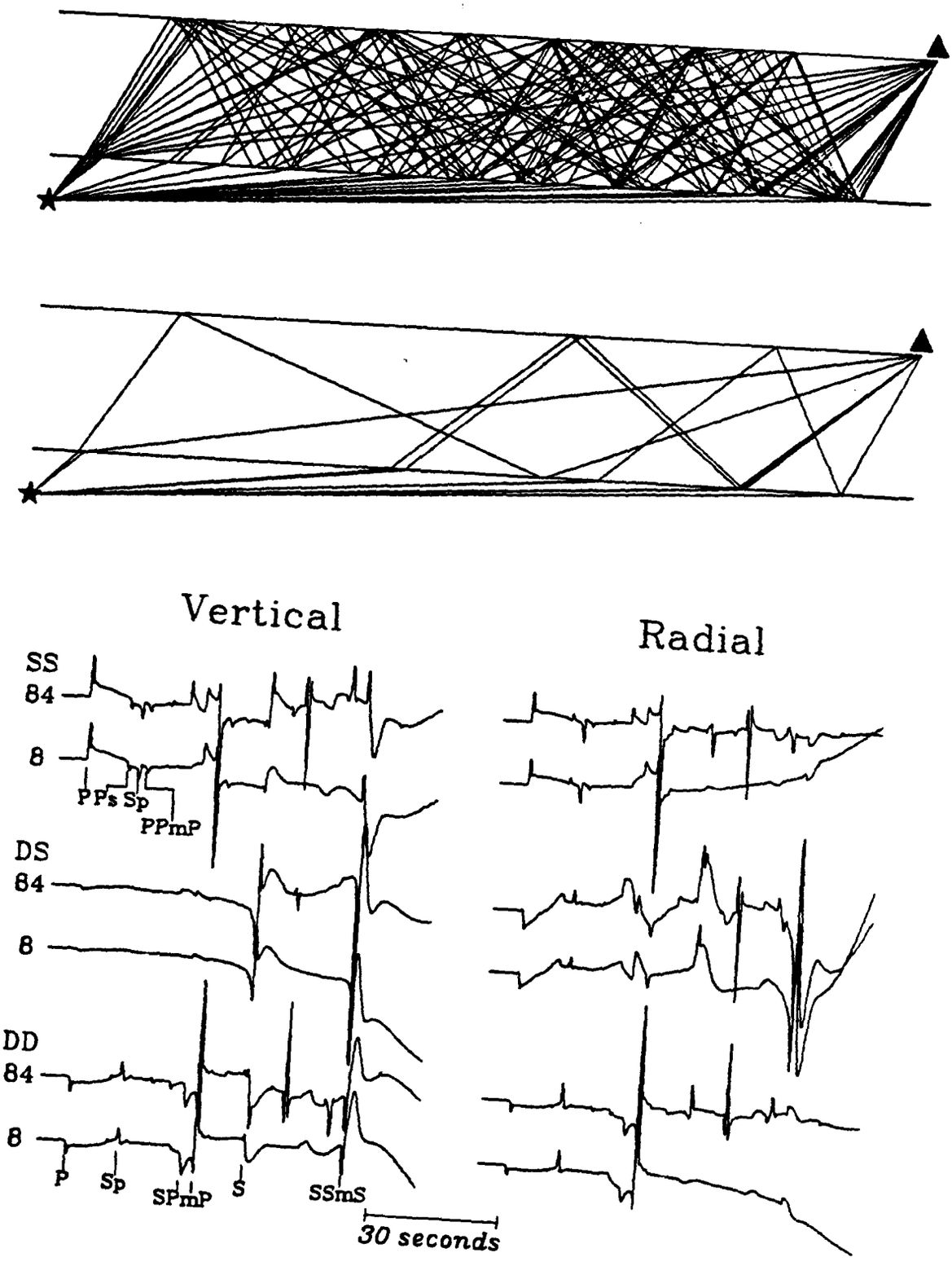

.Corm/.figs/Fig0b.p

Figure 5

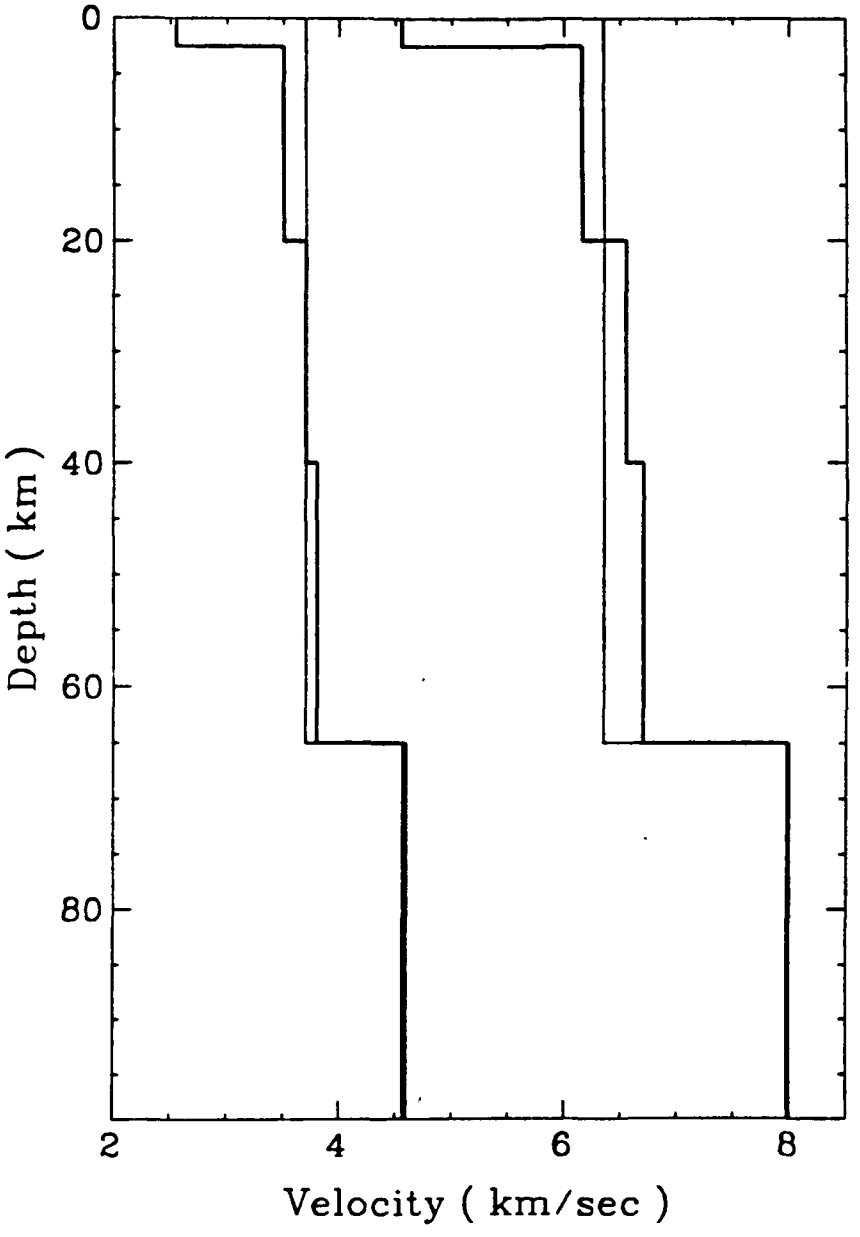

Figure 6

.Cerm/.fige/fig0d.p

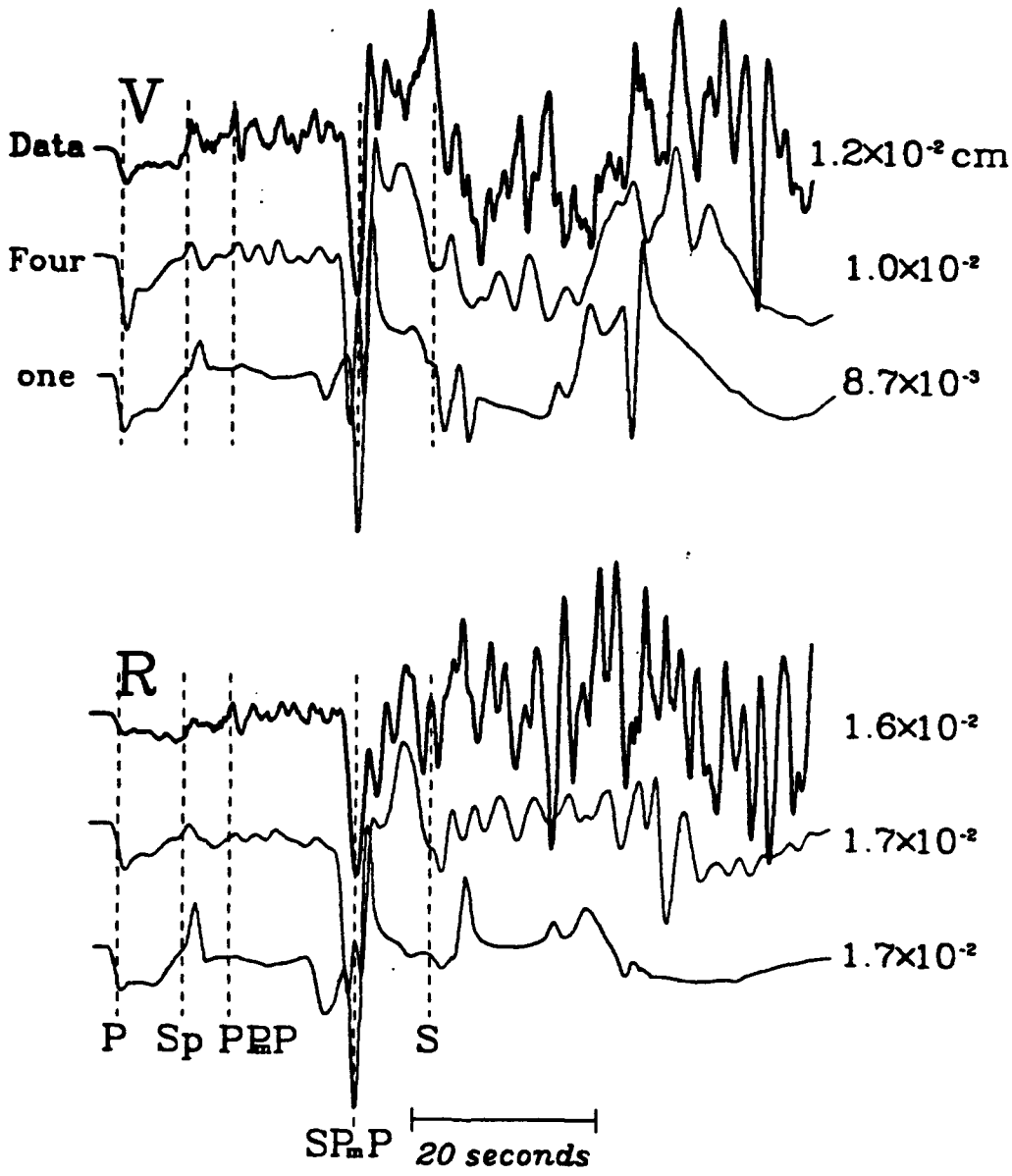

.Corm/.figs/fig0c.p2

Figure 7

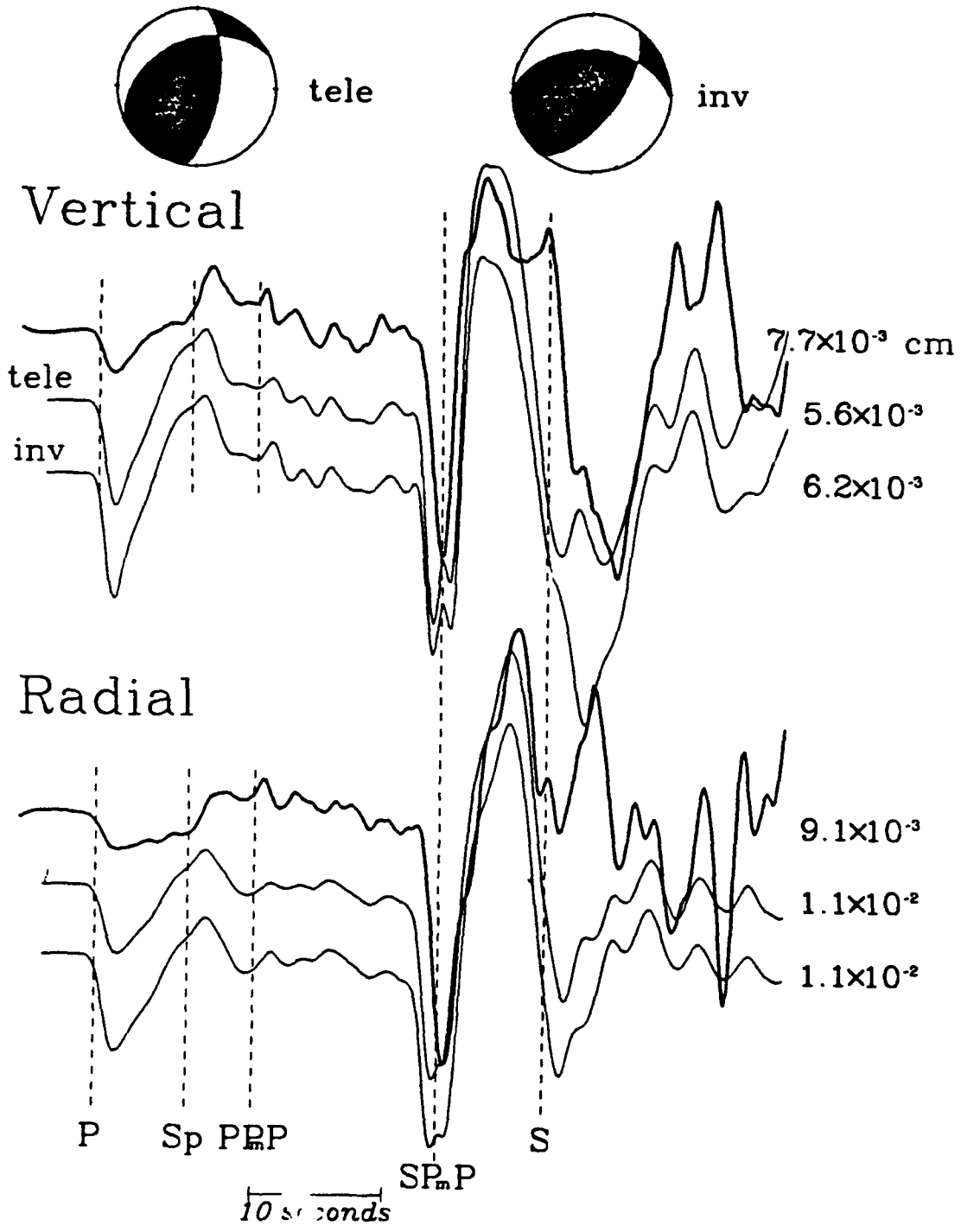

Figure 8

.Germ/.figs/fig01.p

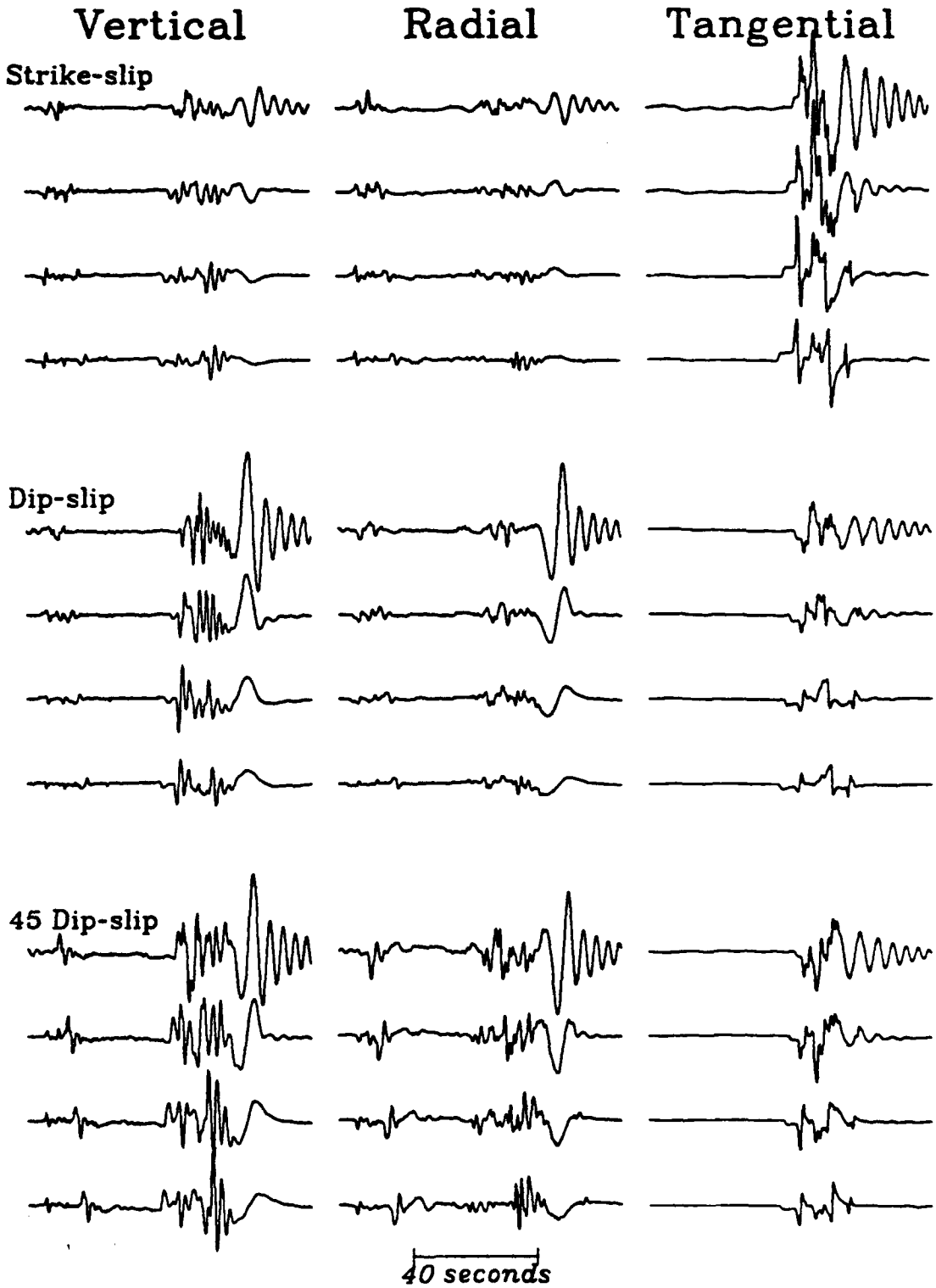
Vertical
Radial
Tangential
Strike-slip
Dip-slip
45 Dip-slip
40 seconds

Figure 9

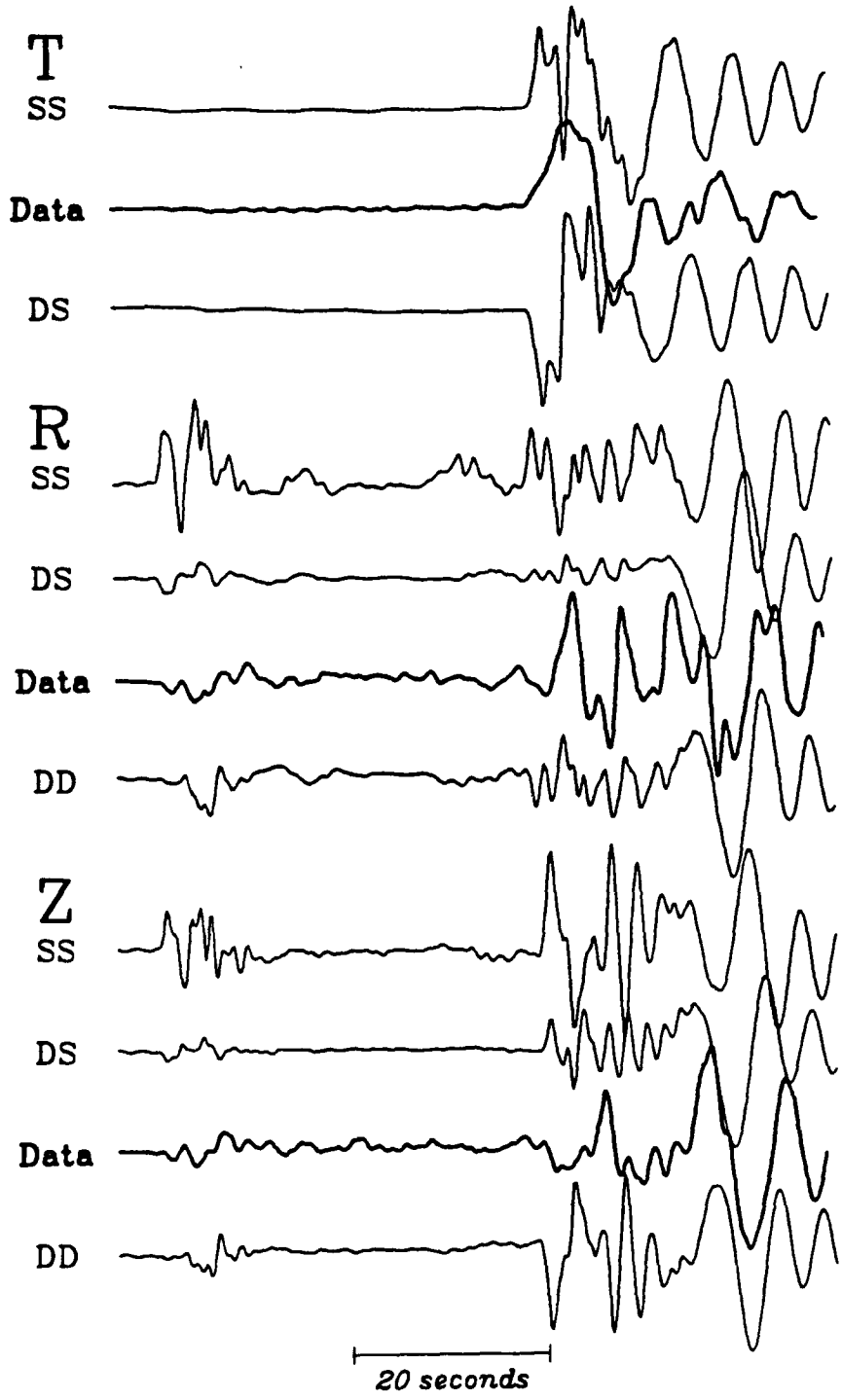

Figure 10

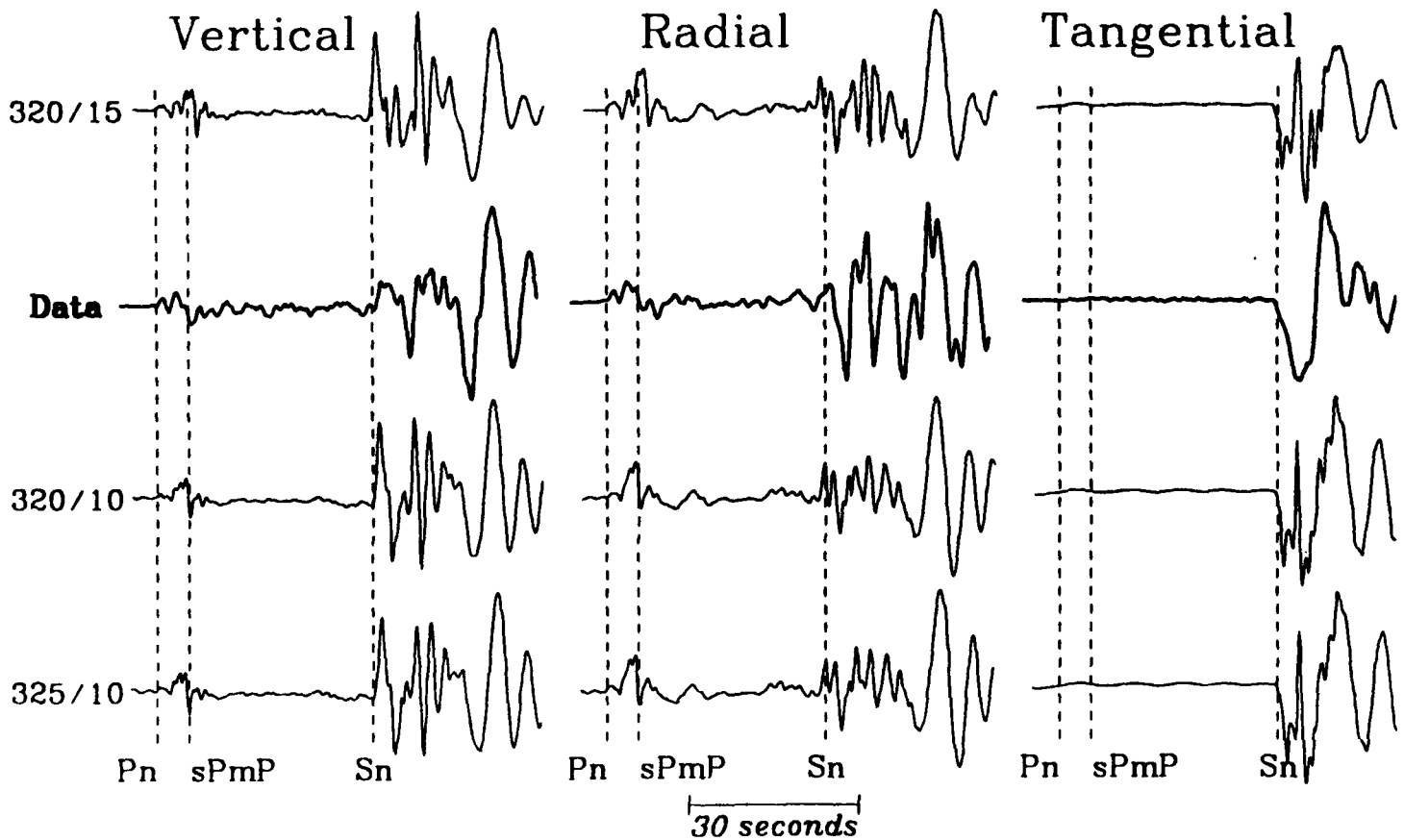
Vertical
Radial
Tangential
320/15
Data
320/10
325/10
Pn
sPmP
Sn
Pn
sPmP
Sn
Pn
sPmP
Sn
30 seconds

Figure 11

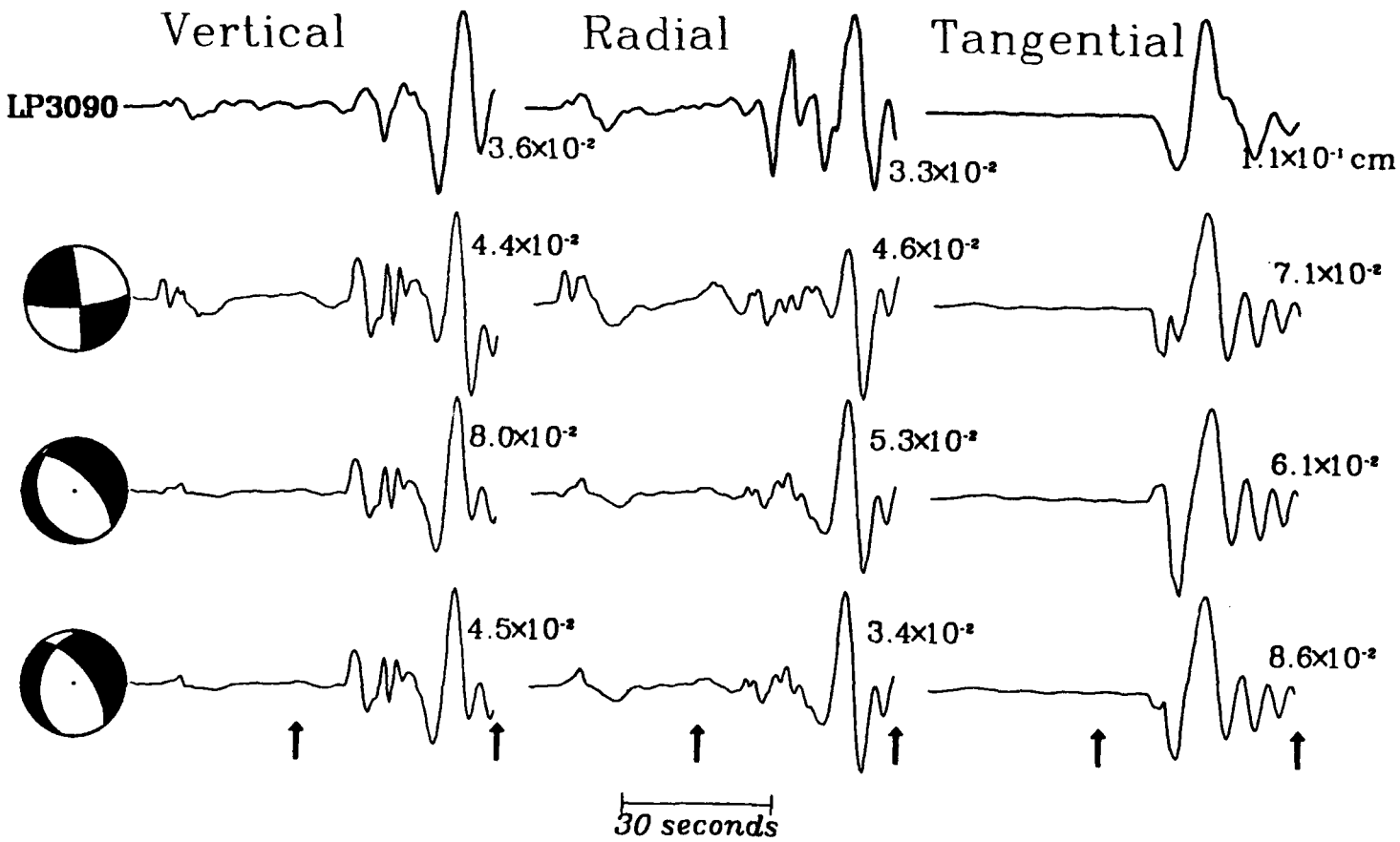
Vertical
Radial
Tangential
LP3090
3.6×10⁻²
3.3×10⁻²
1.1×10⁻¹ cm
4.4×10⁻²
4.6×10⁻²
7.1×10⁻²
8.0×10⁻²
5.3×10⁻²
6.1×10⁻²
4.5×10⁻²
3.4×10⁻²
8.6×10⁻²
30 seconds

Figure 12

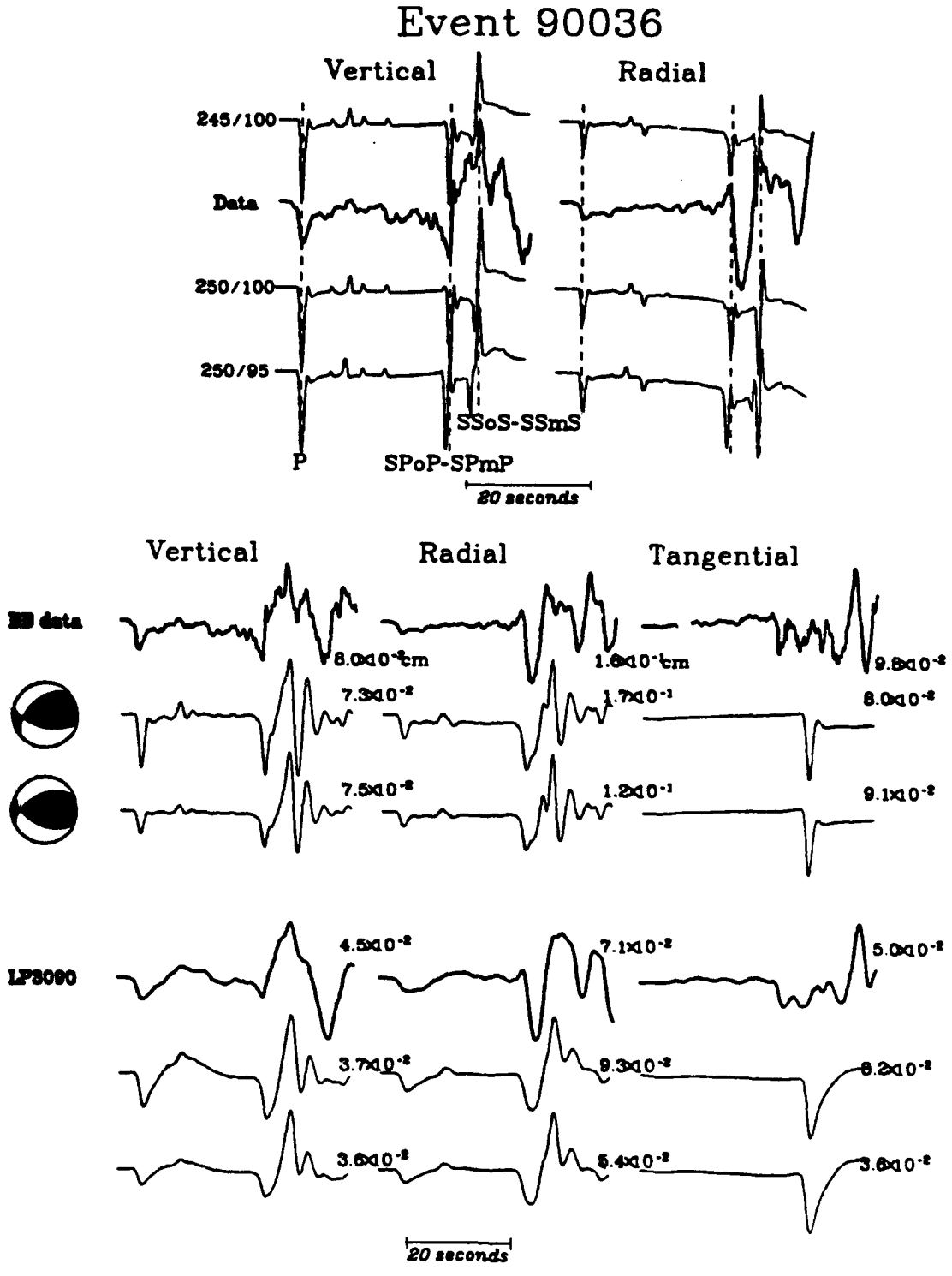

wwc/90036/figcomp.p

Figure 13

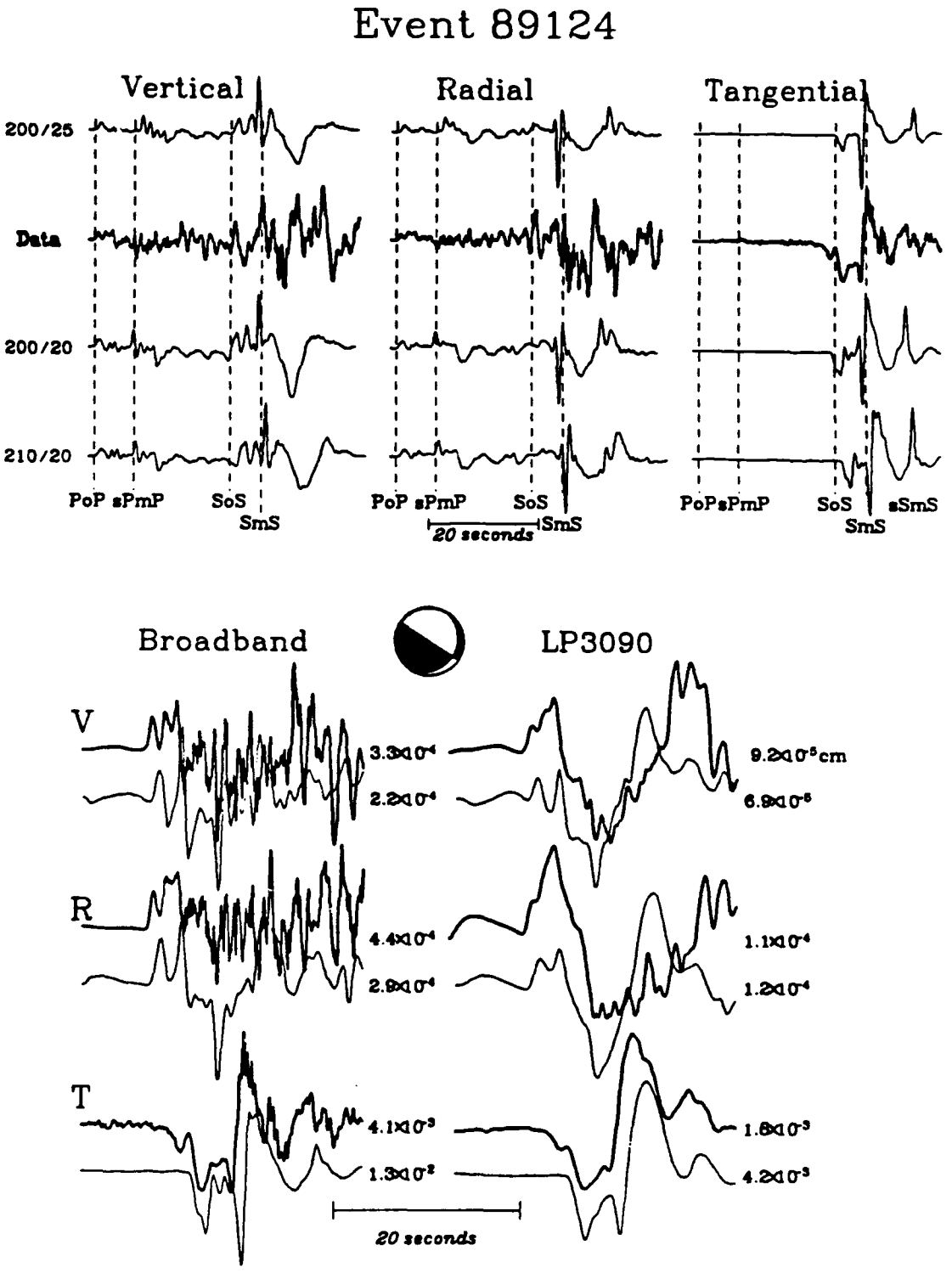

~/wwc/89124/figcomp.p

Figure 14

Event 89146

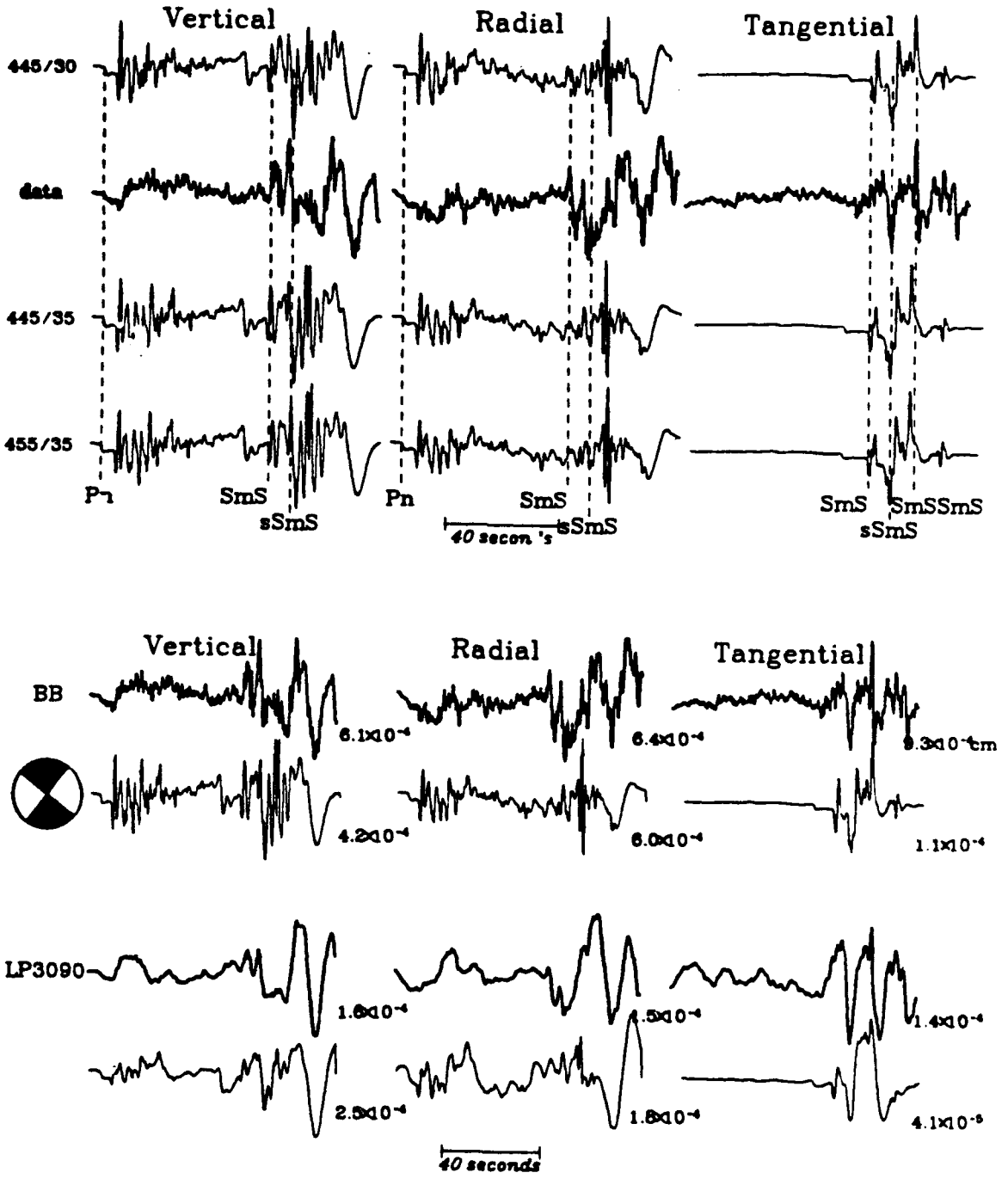

wec/89146/figcomp.p

Figure 15

Event 90085

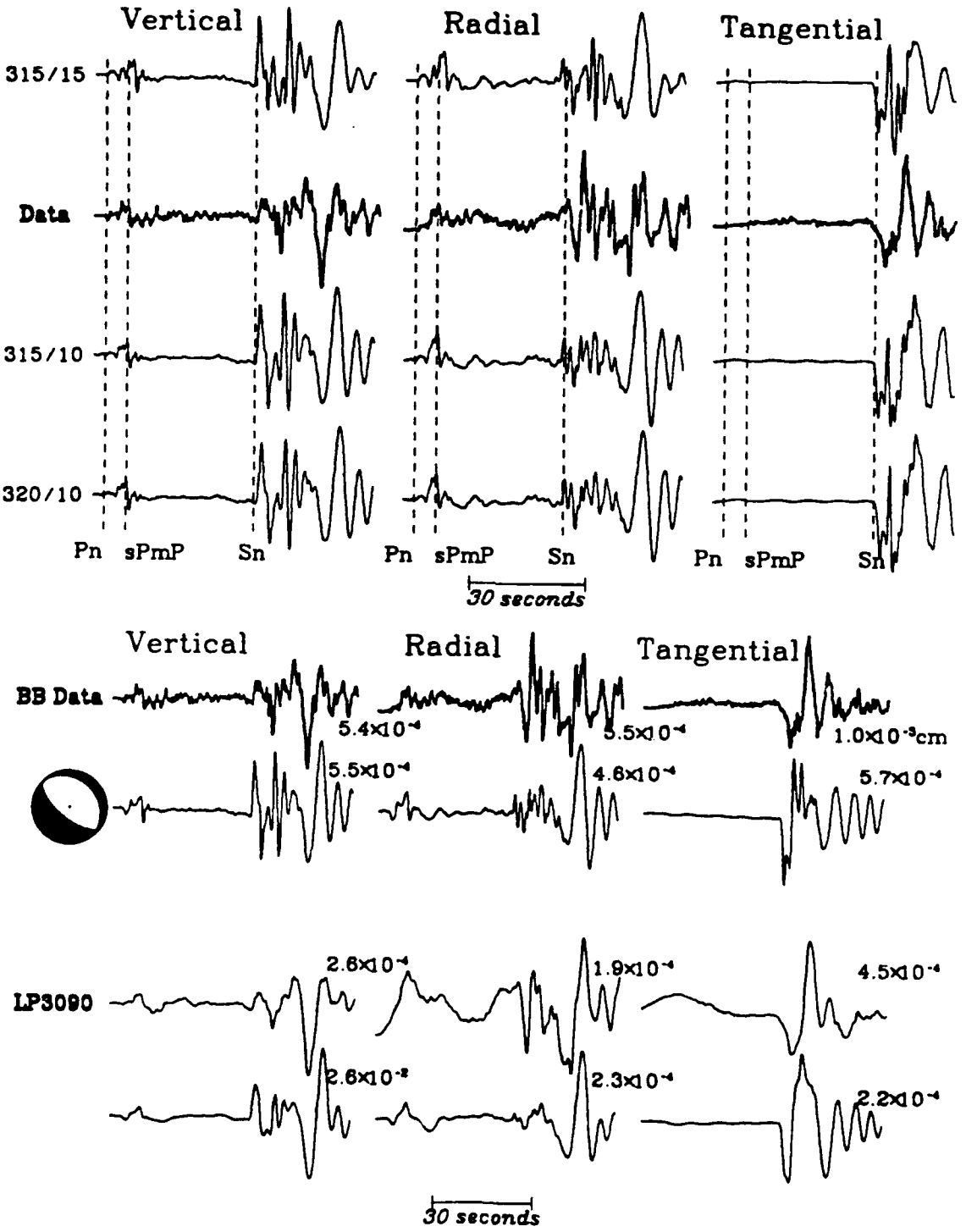

eec/90085/figcomp.p

Figure 16

Event 91026

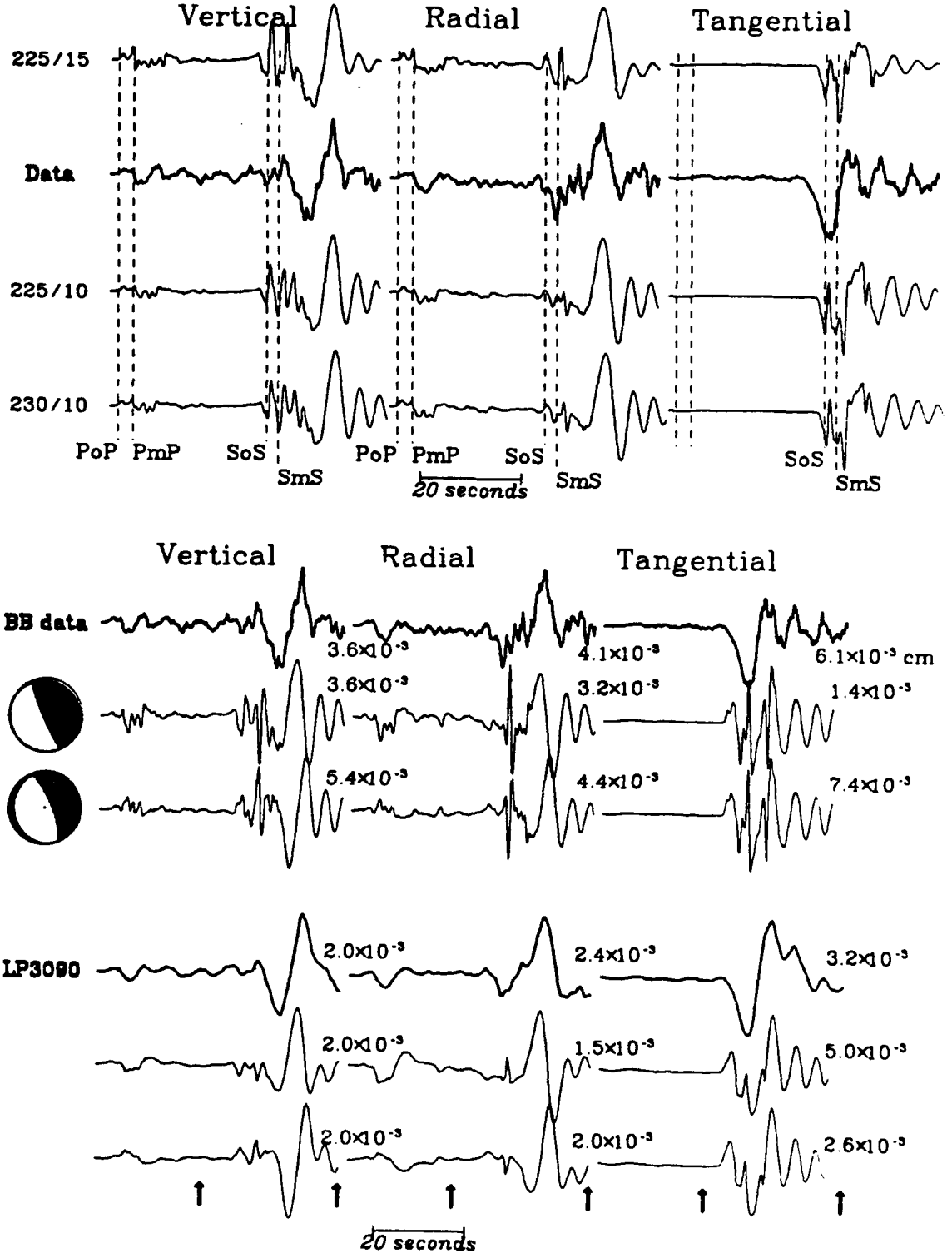

wwc/91026/figcomp.p

Figure 17

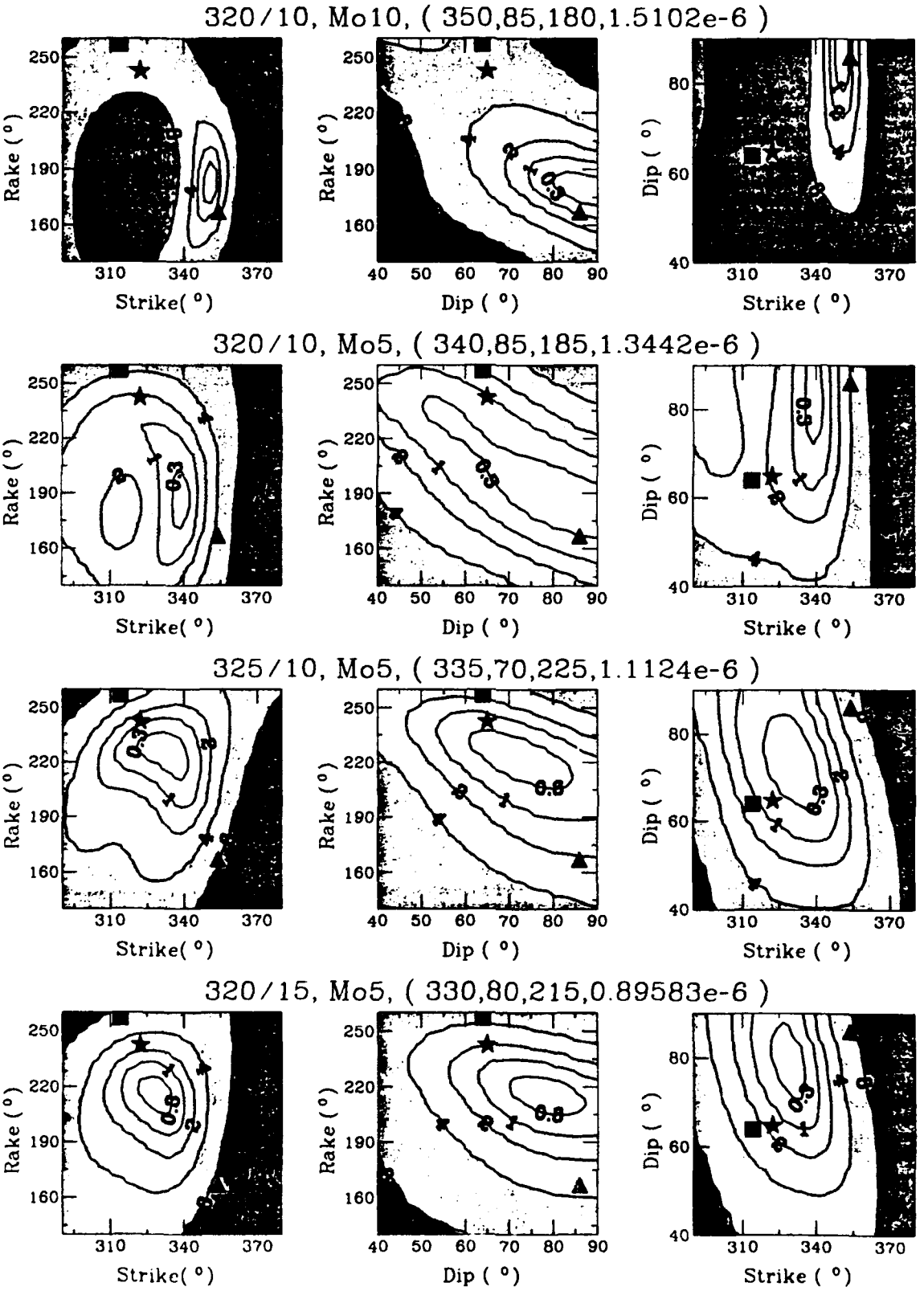

Figure 18
79

fig.par

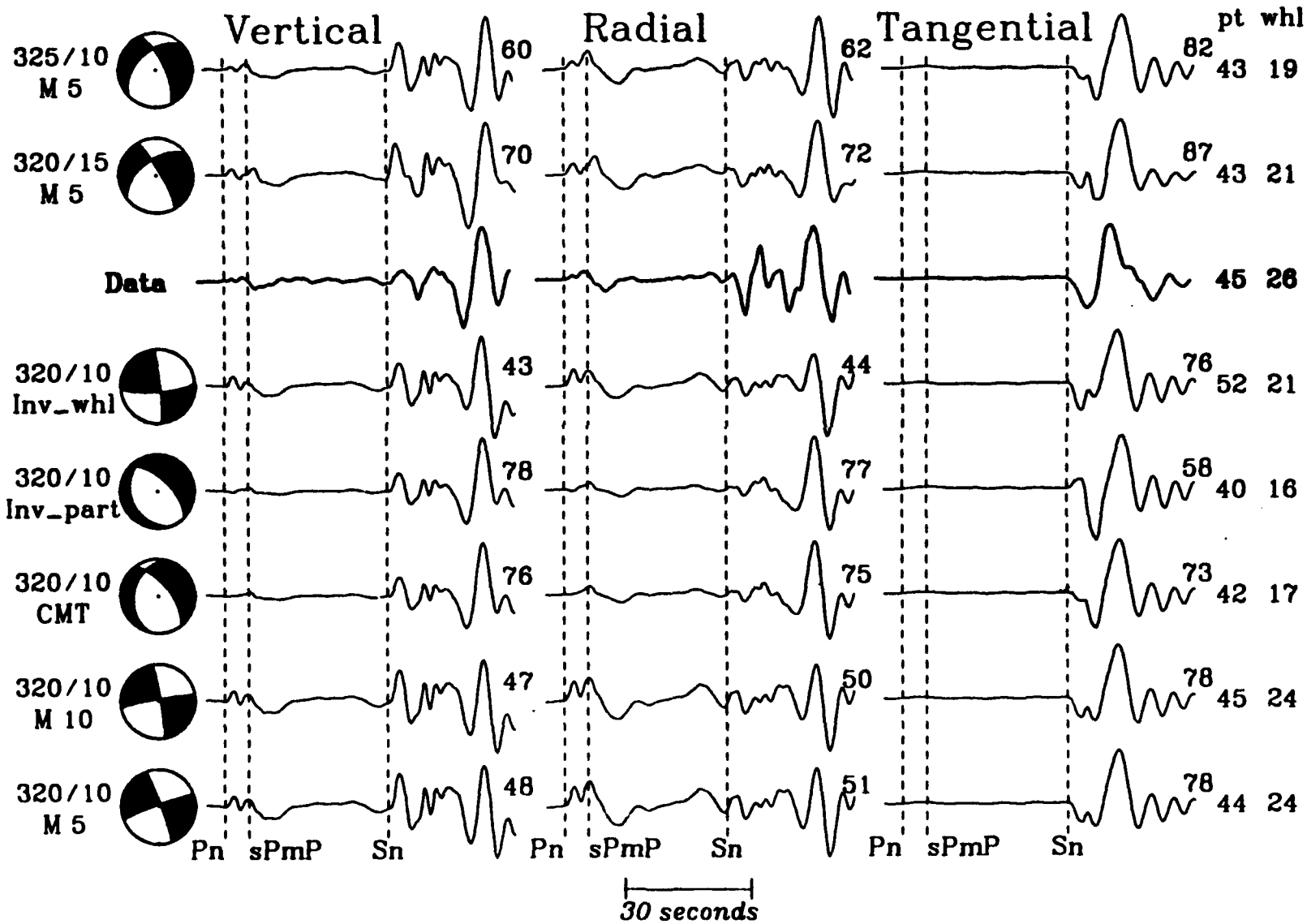
Vertical
Radial
Tangential
pt whl
325/10
M 5
320/15
M 5
Data
320/10
Inv_whl
320/10
Inv_part
320/10
CMT
320/10
M 10
320/10
M 5
60
62
82
43 19
70
72
87
43 21
45 26
43
44
76
52 21
78
77
58
40 16
76
75
73
42 17
47
50
78
45 24
48
51
78
44 24
Pn
sPmP
Sn
Pn
sPmP
Sn
Pn
sPmP
Sn
30 seconds

Figure 19

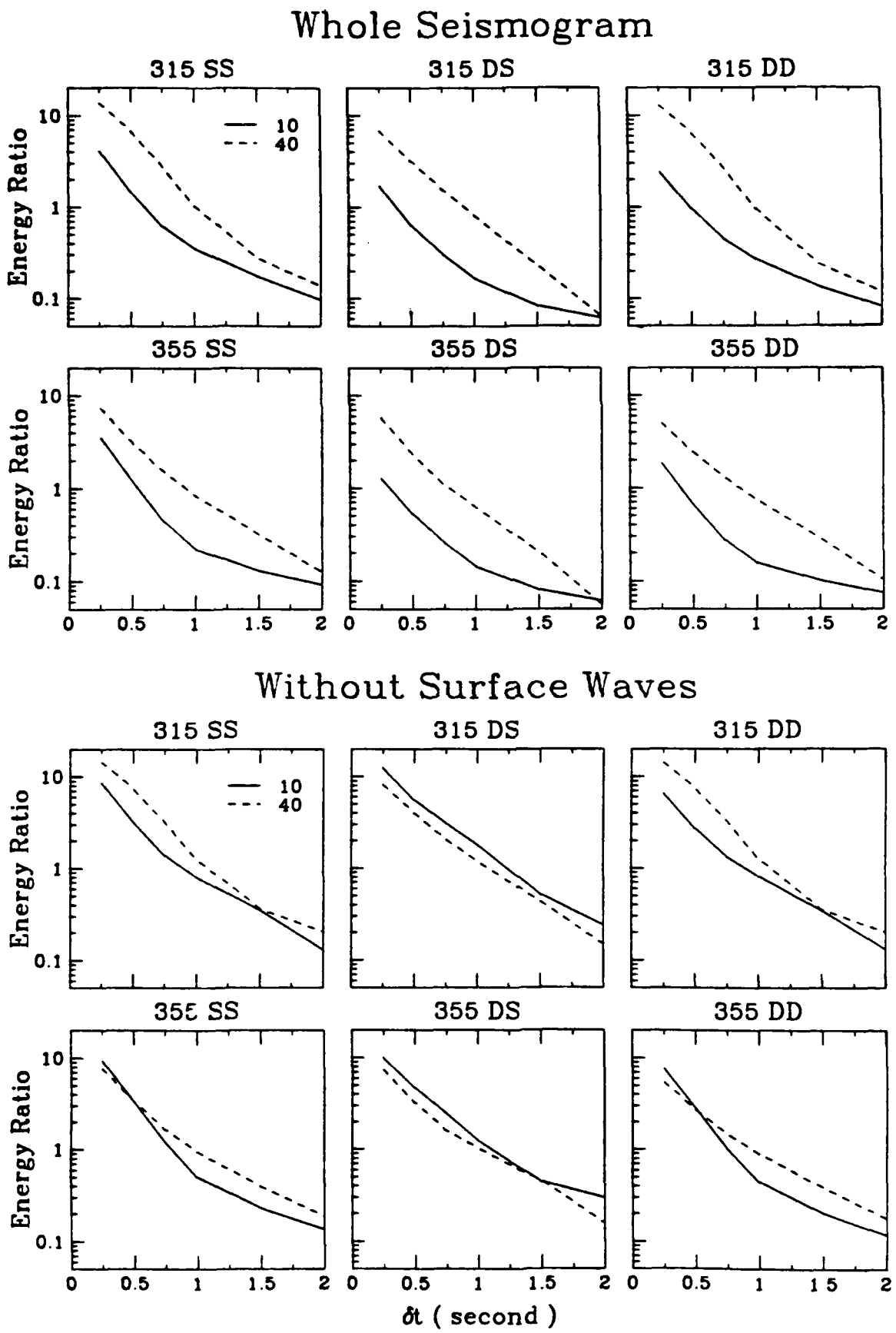

docum/FNN/.*rm/.figs/energy/fig05.p

Figure 20

Prof. Thomas Ahrens
Seismological Lab, 252-21
Division of Geological & Planetary Sciences
California Institute of Technology
Pasadena, CA 91125

Prof. Keiiti Aki
Center for Earth Sciences
University of Southern California
University Park
Los Angeles, CA 90089-0741

Prof. Shelton Alexander
Geosciences Department
403 Deike Building
The Pennsylvania State University
University Park, PA 16802

Dr. Ralph Alewine, III
DARPA/NMRO
3701 North Fairfax Drive
Arlington, VA 22203-1714

Prof. Charles B. Archambeau
CIRES
University of Colorado
Boulder, CO 80309

Dr. Thomas C. Bache, Jr.
Science Applications Int'l Corp.
10260 Campus Point Drive
San Diego, CA 92121 (2 copies)

Prof. Muawia Barazangi
Institute for the Study of the Continent
Cornell University
Ithaca, NY 14853

Dr. Jeff Barker
Department of Geological Sciences
State University of New York
at Binghamton
Vestal, NY 13901

Dr. Douglas R. Baumgardt
ENSCO, Inc
5400 Port Royal Road
Springfield, VA 22151-2388

Dr. Susan Beck
Department of Geosciences
Building #77
University of Arizona
Tuscon, AZ 85721

Dr. T.J. Bennett
S-CUBED
A Division of Maxwell Laboratories
11800 Sunrise Valley Drive, Suite 1212
Reston, VA 22091

Dr. Robert Blandford
AFTAC/TT, Center for Seismic Studies
1300 North 17th Street
Suite 1450
Arlington, VA 22209-2308

Dr. Stephen Bratt
Center for Seismic Studies
1300 North 17th Street
Suite 1450
Arlington, VA 22209-2308

Dr. Lawrence Burdick
IGPP, A-025
Scripps Institute of Oceanography
University of California, San Diego
La Jolla, CA 92093

Dr. Robert Burridge
Schlumberger-Doll Research Center
Old Quarry Road
Ridgefield, CT 06877

Dr. Jerry Carter
Center for Seismic Studies
1300 North 17th Street
Suite 1450
Arlington, VA 22209-2308

Dr. Eric Chael
Division 9241
Sandia Laboratory
Albuquerque, NM 87185

Dr. Martin Chapman
Department of Geological Sciences
Virginia Polytechnical Institute
21044 Derring Hall
Blacksburg, VA 24061

Prof. Vernon F. Cormier
Department of Geology & Geophysics
U-45, Room 207
University of Connecticut
Storrs, CT 06268

Prof. Steven Day
Department of Geological Sciences
San Diego State University
San Diego, CA 92182

Marvin Denny
U.S. Department of Energy
Office of Arms Control
Washington, DC 20585

Dr. Zoltan Der
ENSCO, Inc.
5400 Port Royal Road
Springfield, VA 22151-2388

Prof. Adam Dziewonski
Hoffman Laboratory, Harvard University
Dept. of Earth Atmos. & Planetary Sciences
20 Oxford Street
Cambridge, MA 02138

Prof. John Ebel
Department of Geology & Geophysics
Boston College
Chestnut Hill, MA 02167

Eric Fielding
SNEE Hall
INSTOC
Cornell University
Ithaca, NY 14853

Dr. Mark D. Fisk
Mission Research Corporation
735 State Street
P.O. Drawer 719
Santa Barbara, CA 93102

Prof Stanley Flatte
Applied Sciences Building
University of California, Santa Cruz
Santa Cruz, CA 95064

Dr. John Foley
NER-Geo Sciences
1100 Crown Colony Drive
Quincy, MA 02169

Prof. Donald Forsyth
Department of Geological Sciences
Brown University
Providence, RI 02912

Dr. Art Frankel
U.S. Geological Survey
922 National Center
Reston, VA 22092

Dr. Cliff Frolich
Institute of Geophysics
8701 North Mopac
Austin, TX 78759

Dr. Holly Given
IGPP, A-025
Scripps Institute of Oceanography
University of California, San Diego
La Jolla, CA 92093

Dr. Jeffrey W. Given
SAIC
10260 Campus Point Drive
San Diego, CA 92121

Dr. Dale Glover
Defense Intelligence Agency
ATTN: ODT-1B
Washington, DC 20301

Dr. Indra Gupta
Teledyne Geotech
314 Montgomery Street
Alexanderia, VA 22314

Dan N. Hagedon
Pacific Northwest Laboratories
Battelle Boulevard
Richland, WA 99352

Dr. James Hannon
Lawrence Livermore National Laboratory
P.O. Box 808
L-205
Livermore, CA 94550

Dr. Roger Hansen
HQ AFTAC/TTR
130 South Highway A1A
Patrick AFB, FL 32925-3002

Prof. David G. Harkrider
Seismological Laboratory
Division of Geological & Planetary Sciences
California Institute of Technology
Pasadena, CA 91125

Prof. Danny Harvey
CIRES
University of Colorado
Boulder, CO 80309

Prof. Donald V. Helmberger
Seismological Laboratory
Division of Geological & Planetary Sciences
California Institute of Technology
Pasadena, CA 91125

Prof. Eugene Herrin
Institute for the Study of Earth and Man
Geophysical Laboratory
Southern Methodist University
Dallas, TX 75275

Prof. Robert B. Herrmann
Department of Earth & Atmospheric Sciences
St. Louis University
St. Louis, MO 63156

Prof. Lane R. Johnson
Seismographic Station
University of California
Berkeley, CA 94720

Prof. Thomas H. Jordan
Department of Earth, Atmospheric &
Planetary Sciences
Massachusetts Institute of Technology
Cambridge, MA 02139

Prof. Alan Kafka
Department of Geology & Geophysics
Boston College
Chestnut Hill, MA 02167

Robert C. Kemerait
ENSCO, Inc.
445 Pineda Court
Melbourne, FL 32940

Dr. Karl Koch
Institute for the Study of Earth and Man
Geophysical Laboratory
Southern Methodist University
Dallas, Tx 75275

Dr. Max Koontz
U.S. Dept. of Energy/DP 5
Forrestal Building
1000 Independence Avenue
Washington, DC 20585

Dr. Richard LaCoss
MIT Lincoln Laboratory, M-200B
P.O. Box 73
Lexington, MA 02173-0073

Dr. Fred K. Lamb
University of Illinois at Urbana-Champaign
Department of Physics
1110 West Green Street
Urbana, IL 61801

Prof. Charles A. Langston
Geosciences Department
403 Deike Building
The Pennsylvania State University
University Park, PA 16802

Jim Lawson, Chief Geophysicist
Oklahoma Geological Survey
Oklahoma Geophysical Observatory
P.O. Box 8
Leonard, OK 74043-0008

Prof. Thorne Lay
Institute of Tectonics
Earth Science Board
University of California, Santa Cruz
Santa Cruz, CA 95064

Dr. William Leith
U.S. Geological Survey
Mail Stop 928
Reston, VA 22092

Mr. James F. Lewkowicz
Phillips Laboratory/GPEH
29 Randolph Road
Hanscom AFB, MA 01731-3010(2 copies)

Mr. Alfred Lieberman
ACDA/VI-OA State Department Building
Room 5726
320-21st Street, NW
Washington, DC 20451

Prof. L. Timothy Long
School of Geophysical Sciences
Georgia Institute of Technology
Atlanta, GA 30332

Dr. Randolph Martin, III
New England Research, Inc.
76 Olcott Drive
White River Junction, VT 05001

Dr. Robert Masse
Denver Federal Building
Box 25046, Mail Stop 967
Denver, CO 80225

Dr. Gary McCartor
Department of Physics
Southern Methodist University
Dallas, TX 75275

Prof. Thomas V. McEvilly
Seismographic Station
University of California
Berkeley, CA 94720

Dr. Art McGarr
U.S. Geological Survey
Mail Stop 977
U.S. Geological Survey
Menlo Park, CA 94025

Dr. Keith L. McLaughlin
S-CUBED
A Division of Maxwell Laboratory
P.O. Box 1620
La Jolla, CA 92038-1620

Stephen Miller & Dr. Alexander Florence
SRI International
333 Ravenswood Avenue
Box AF 116
Menlo Park, CA 94025-3493

Prof. Bernard Minster
IGPP, A-025
Scripps Institute of Oceanography
University of California, San Diego
La Jolla, CA 92093

Prof. Brian J. Mitchell
Department of Earth & Atmospheric Sciences
St. Louis University
St. Louis, MO 63156

Mr. Jack Murphy
S-CUBED
A Division of Maxwell Laboratory
11800 Sunrise Valley Drive, Suite 1212
Reston, VA 22091 (2 Copies)

Dr. Keith K. Nakanishi
Lawrence Livermore National Laboratory
L-025
P.O. Box 808
Livermore, CA 94550

Dr. Carl Newton
Los Alamos National Laboratory
P.O. Box 1663
Mail Stop C335, Group ESS-3
Los Alamos, NM 87545

Dr. Bao Nguyen
HQ AFTAC/TTR
130 South Highway A1A
Patrick AFB, FL 32925-3002

Prof. John A. Orcutt
IGPP, A-025
Scripps Institute of Oceanography
University of California, San Diego
La Jolla, CA 92093

Prof. Jeffrey Park
Kline Geology Laboratory
P.O. Box 6666
New Haven, CT 06511-8130

Dr. Howard Patton
Lawrence Livermore National Laboratory
L-025
P.O. Box 808
Livermore, CA 94550

Dr. Frank Pilotte
HQ AFTAC/TT
130 South Highway A1A
Patrick AFB, FL 32925-3002

Dr. Jay J. Pulli
Radix Systems, Inc.
201 Perry Parkway
Gaithersburg, MD 20877

Dr. Robert Reinke
ATTN: FCTVTD
Field Command
Defense Nuclear Agency
Kirtland AFB, NM 87115

Prof. Paul G. Richards
Lamont-Doherty Geological Observatory
of Columbia University
Palisades, NY 10964

Mr. Wilmer Rivers
Teledyne Geotech
314 Montgomery Street
Alexandria, VA 22314

Dr. George Rothe
HQ AFTAC/TTR
130 South Highway A1A
Patrick AFB, FL 32925-3002

Dr. Alan S. Ryall, Jr.
DARPA/NMRO
3701 North Fairfax Drive
Arlington, VA 22209-1714

Dr. Richard Sailor
TASC, Inc.
55 Walkers Brook Drive
Reading, MA 01867

Prof. Charles G. Sammis
Center for Earth Sciences
University of Southern California
University Park
Los Angeles, CA 90089-0741

Prof. Christopher H. Scholz
Lamont-Doherty Geological Observatory
of Columbia University
Palisades, NY 10964

Dr. Susan Schwartz
Institute of Tectonics
1156 High Street
Santa Cruz, CA 95064

Secretary of the Air Force
(SAFRD)
Washington, DC 20330

Office of the Secretary of Defense
DDR&E
Washington, DC 20330

Thomas J. Sereno, Jr.
Science Application Int'l Corp.
10260 Campus Point Drive
San Diego, CA 92121

Dr. Michael Shore
Defense Nuclear Agency/SPSS
6801 Telegraph Road
Alexandria, VA 22310

Dr. Robert Shumway
University of California Davis
Division of Statistics
Davis, CA 95616

Dr. Matthew Sibol
Virginia Tech
Seismological Observatory
4044 Derring Hall
Blacksburg, VA 24061-0420

Prof. David G. Simpson
IRIS, Inc.
1616 North Fort Myer Drive
Suite 1050
Arlington, VA 22209

Donald L. Springer
Lawrence Livermore National Laboratory
L-025
P.O. Box 808
Livermore, CA 94550

Dr. Jeffrey Stevens
S-CUBED
A Division of Maxwell Laboratory
P.O. Box 1620
La Jolla, CA 92038-1620

Lt. Col. Jim Stobie
ATTN: AFOSR/NL
110 Duncan Avenue
Bolling AFB
Washington, DC 20332-0001

Prof. Brian Stump
Institute for the Study of Earth & Man
Geophysical Laboratory
Southern Methodist University
Dallas, TX 75275

Prof. Jeremiah Sullivan
University of Illinois at Urbana-Champaign
Department of Physics
1110 West Green Street
Urbana, IL 61801

Prof. L. Sykes
Lamont-Doherty Geological Observatory
of Columbia University
Palisades, NY 10964

Dr. David Taylor
ENSCO, Inc.
445 Pineda Court
Melbourne, FL 32940

Dr. Steven R. Taylor
Los Alamos National Laboratory
P.O. Box 1663
Mail Stop C335
Los Alamos, NM 87545

Prof. Clifford Thurber
University of Wisconsin-Madison
Department of Geology & Geophysics
1215 West Dayton Street
Madison, WS 53706

Prof. M. Nafi Toksoz
Earth Resources Lab
Massachusetts Institute of Technology
42 Carleton Street
Cambridge, MA 02142

Dr. Larry Turnbull
CIA-OSWR/NED
Washington, DC 20505

Dr. Gregory van der Vink
IRIS, Inc.
1616 North Fort Myer Drive
Suite 1050
Arlington, VA 22209

Dr. Karl Veith
EG&G
5211 Auth Road
Suite 240
Suitland, MD 20746

Prof. Terry C. Wallace
Department of Geosciences
Building #77
University of Arizona
Tuscon, AZ 85721

Dr. Thomas Weaver
Los Alamos National Laboratory
P.O. Box 1663
Mail Stop C335
Los Alamos, NM 87545

Dr. William Wortman
Mission Research Corporation
8560 Cinderbed Road
Suite 700
Newington, VA 22122

Prof. Francis T. Wu
Department of Geological Sciences
State University of New York
at Binghamton
Vestal, NY 13901

AFTAC/CA
(STINFO)
Patrick AFB, FL 32925-6001

DARPA/PM
3701 North Fairfax Drive
Arlington, VA 22203-1714

DARPA/RMO/RETRIEVAL
3701 North Fairfax Drive
Arlington, VA 22203-1714

DARPA/RMO/SECURITY OFFICE
3701 North Fairfax Drive
Arlington, VA 22203-1714

HQ DNA
ATTN: Technical Library
Washington, DC 20305

Defense Intelligence Agency
Directorate for Scientific & Technical Intelligence
ATTN: DTIB
Washington, DC 20340-6158

Defense Technical Information Center
Cameron Station
Alexandria, VA 22314 (2 Copies)

TACTEC
Battelle Memorial Institute
505 King Avenue
Columbus, OH 43201 (Final Report)

Phillips Laboratory
ATTN: XPG
29 Randolph Road
Hanscom AFB, MA 01731-3010

Phillips Laboratory
ATTN: GPE
29 Randolph Road
Hanscom AFB, MA 01731-3010

Phillips Laboratory
ATTN: TSML
5 Wright Street
Hanscom AFB, MA 01731-3004

Phillips Laboratory
ATTN: PL/SUL
3550 Aberdeen Ave SE
Kirtland, NM 87117-5776 (2 copies)

Dr. Michel Bouchon
I.R.I.G.M.-B.P. 68
38402 St. Martin D'Heres
Cedex, FRANCE

Dr. Michel Campillo
Observatoire de Grenoble
I.R.I.G.M.-B.P. 53
38041 Grenoble, FRANCE

Dr. Kin Yip Chun
Geophysics Division
Physics Department
University of Toronto
Ontario, CANADA

Prof. Hans-Peter Harjes
Institute for Geophysic
Ruhr University/Bochum
P.O. Box 102148
4630 Bochum 1, GERMANY

Prof. Eystein Husebye
NTNF/NORSAR
P.O. Box 51
N-2007 Kjeller, NORWAY

David Jepsen
Acting Head, Nuclear Monitoring Section
Bureau of Mineral Resources
Geology and Geophysics
G.P.O. Box 378, Canberra, AUSTRALIA

Ms. Eva Johannisson
Senior Research Officer
FOA
S-172 90 Sundbyberg, SWEDEN

Dr. Peter Marshall
Procurement Executive
Ministry of Defense
Blacknest, Brimpton
Reading FG7-FRS, UNITED KINGDOM

Dr. Bernard Massinon, Dr. Pierre Mechler
Societe Radiomana
27 rue Claude Bernard
75005 Paris, FRANCE (2 Copies)

Dr. Svein Mykkeltveit
NTNT/NORSAR
P.O. Box 51
N-2007 Kjeller, NORWAY (3 Copies)

Prof. Keith Priestley
University of Cambridge
Bullard Labs, Dept. of Earth Sciences
Madingley Rise, Madingley Road
Cambridge CB3 OEZ, ENGLAND

Dr. Jorg Schlittenhardt
Federal Institute for Geosciences & Nat'l Res.
Postfach 510153
D-3000 Hannover 51, GERMANY

Dr. Johannes Schweitzer
Institute of Geophysics
Ruhr University/Bochum
P.O. Box 1102148
4360 Bochum 1, GERMANY

Trust & Verify
VERTIC
8 John Adam Street
London WC2N 6EZ, ENGLAND